PRELIMINARY DEVELOPMENT OF A BIO-INSPIRED HEXAPOD CLIMBING ROBOT RELYING ON DRY ADHESIVES

by

Yasong Li
B. Eng., South China Agricultural University, 2006

THESIS SUBMITTED IN PARTIAL FULFILLMENT OF
THE REQUIREMENTS FOR THE DEGREE OF

MASTER OF APPLIED SCIENCE

In the
School of Engineering Science

SIMON FRASER UNIVERSITY

Summer 2009

APPROVAL

Name: **Yasong Li**

Degree: **Master of Applied Science**

Title of Thesis: **Preliminary Development of a Bio-inspired Hexapod Climbing Robot Relying on Dry Adhesives**

Examining Committee:

Chair:

Dr. Ash Parameswaran
Professor – Engineering Science

Dr. Carlo Menon
Senior Supervisor
Assistant Professor – Engineering Science

Dr. Shahram Payandeh
Supervisor
Professor – Engineering Science

Dr. Siamak Arzanpour
Internal Examiner
Assistant Professor – Engineering Science Surrey

Date Defended/Approved: July 23, 2009

Declaration of
Partial Copyright Licence

ABSTRACT

Biologists have recently discovered that dry adhesion on the feet of geckos and hunting spiders provides remarkable adhesive forces generated by van der Waals forces. Different researches have attempted to mimic the adhesive used by geckos and spiders adhesives through novel manufacturing processes. This thesis presents the preliminary analysis and development of hexapod climbing robot prototypes designed to take advantage of the special features that dry adhesion offers. A kinematic analysis was performed, which was validated through an experimental procedure. The two robotic prototypes, which were developed following engineering design procedures, are presented and discussed in this thesis. Preliminary investigations on optimal trajectory and joint torques for enhancing dry adhesive properties are introduced for a future in depth analysis and use in climbing platforms.

Keywords: climbing robot; kinematics; hexapod; dry adhesion; bio-inspired

I dedicate this thesis to my family.

To mom and dad, for your unconditional love and support.

To grandma, the first teacher in my early days.

To grandpa, the respectable man forever.

ACKNOWLEDGEMENTS

I would like to dedicate faithful thanks to my senior supervisor, Dr. Carlo Menon, who provided such a great topic and helped me through the research, and also for teaching me how to become a professional.

I also extend my acknowledgements to Dr. Ash Parameswaran and Dr. Shahram Payandeh, for the inspiring lessons and advice you gave; Dr. Daniel Sameoto, you are always my good example; Gary Houghton, for your help in rapid prototyping machine; Gary Shum and Marius Haiducu, for helping in huge amount of ordering forms; and all the faculty members, staffs and technicians who run the school in good condition.

Here I also would like to thank my colleagues and friends (alphabetically): Ausama Ahmed, Bastian Tietjen, Chris Martens, Claire Wu, Dr. Cormac Sheridan, Dariush Sahebjavaher, David Tang, Doris Liu, Isacco Pretto, Jenny Ma, Jyh-Yuan Yeh, Kaveh Kianfar, Menita Prasad, Nathan Cheng, Nathaniel Seung, Nina Sauthoff, Simon Ruffieux, Ted Meredith, Wen Shi, Xiaochuan Sun, Xingjie Jiang, and Zeeshan Khokhar. You all make Vancouver and SFU such a nice place to stay.

Last, thank GOD there is such a discipline I enjoy with passion!

TABLE OF CONTENTS

LIST OF FIGURES

LIST OF TABLES

CHAPTER 1 INTRODUCTION

Interest in studying climbing robots has grown rapidly in the recent decade. Research can be categorized in four key areas of application: (1) servicing (e.g., maintenance of skyscrapers, ships' hulls, nuclear plants, etc.); (2) rescue (e.g., during fire, earthquakes, landslides, etc.); (3) security (e.g., surveillance, inspection, and military operations in buildings, extreme natural environments, etc.); and (4) space (e.g., planetary exploration, Intra-Vehicular Activities, Extra-Vehicular Activities, etc.) [1].

Among natural climbers, some creatures, such as geckos and spiders stand out, as they can climb on almost all kinds of surfaces, even upside down. Biologists have determined that their spectacular climbing ability is mainly due to the nano-/micro-scale structures on their feet. These structures have been named “dry adhesives”, as their adhesion relies on van der Waals forces rather than tacky materials [2]. Biological dry adhesives are lightweight, self-cleaning and have a high safety factor.[1] The manufacture of synthetic dry adhesives has been proven to be possible [3-7], and it is potentially suitable to enable the development of climbing robots for different applications [8-15].

This thesis focuses on the design of a potentially robust and energy efficient climbing mechanism utilizing dry adhesion. The proof-of-concept prototypes were developed to show the ability of vertical climbing.

[1] Safety factor is the relationship between body weight and the maximum adhesive force.

1.1 Motivation

The dry adhesion mechanism was first discovered on Tokay gecko's feet by K. Autumn et al. [2]. Further investigation extended to some species of hunting spiders such as the jumping spider *Evarcha arcuata* [16], the wondering spider *Cupiennius salei* and the bird spider *Aphonopelma seemanni* [17]. Hunting spiders, unlike the web spiders, do not build webs to trap their prey. Instead, they wait and ambush their prey by launching a quick attack when the prey comes close. Hence these spiders have to safely stand on the surfaces of different materials and roughness. In the upper left picture of Figure 1, a wondering spider, *Cupiennius salei*, is sitting on a glass plate. The rest of the pictures consecutively show the multi-scale structure on the spider leg: claws (CL) and scopulae (CS for claw scopulae and TS for tarsal scopulae) on top of the leg, setae (SE) on top of the scopula, and spatulae (SP) on top of the seta. Relying on this multi-scale structure, the adhesive force is enlarged significantly by enlarging the contact area. Kesel et al. [16] measured the adhesive force of a single setule on *Evarcha arcuata* using atomic force microscopy (AFM), and the result showed an adhesive force up to 41 nN when the setule was perpendicular to the contacting surface. Estimating the species' numbers of setules to be 642000 and the total contact area to be 1.06×10^{11} nm^2, the total adhesive force could reach 2.56×10^{-2} N. Given that the weight of the spider is approximately 15.1 mg, the safety factor could, therefore, reach 173.

Dry adhesives also possess the property of anisotropic adhesion; dragging in one direction reinforces the adhesive force while dragging in the

opposite direction releases the adhesive force. Autumn et al. [18] proposed the term programmable adhesive to describe the gecko's ability to preload and drag at angels smaller than 30 degrees to turn on the adhesive and increasing the angle to easily turn off the adhesive. In the case of spiders, Niederegger et al. [17] proposed that spiders push the tarsal to reinforce the adhesion and pull to release the adhesion, due to the nano-hair arrangement on the spider legs.

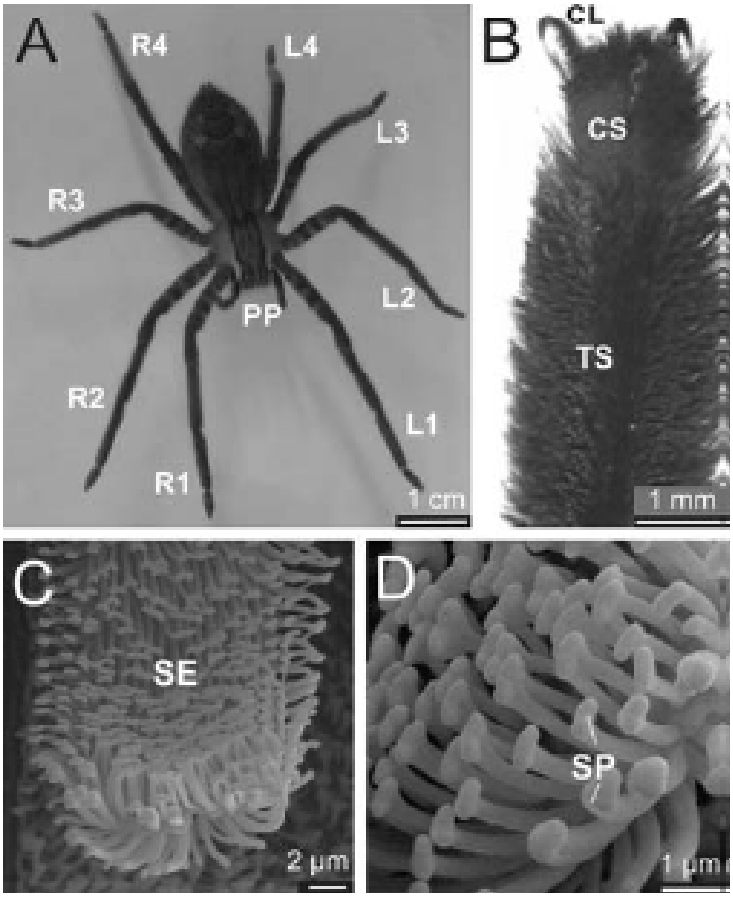

Figure 1-1: Multi-scale adhesion mechanism in the spider *Cupiennius salei*. A) Spider resting on a tilted glass plate, B) Claws and scopula, C) Tip of single seta, D) Microtrichia with spatula at their tips. (Picture cited from Niederegger and Gorb, 2006. [17])

Several attempts have been made to replicate natural dry adhesion since confirming the dry adhesion on gecko's feet. The first attempts of manufacturing synthetic dry adhesion were reported by Campolo et al. [19], Sitti and Fearing [20], and Geim et al. [21] in 2003. These early attempts focused on replicating the nano-structures, but the fibers (diameter of several hundred nanometers) tended to be clump together, therefore, the samples were not sticky as expected. Afterwards, fabrication of synthetic dry adhesion started to focus on a bigger scale of fibers (with diameters varying from several microns to several hundred microns) [22-24]. Those adhesive designs tried to replicate the anisotropic property of natural dry adhesion by manufacturing fibers at a certain angle to the substrate or by adding asymmetric structures on the fibers. Performance was enhanced and, therefore, enabled a few successful climbing robots to employ these adhesive designs.

Following this enhancement, dry adhesive development grew rapidly, allowing climbing robots to use different shapes and functions of dry adhesives. During early exploration of developing climbing robot utilizing dry adhesion, three key criteria were identified in [13] for reliable climbing robot using dry adhesion: (1) maximize the attachment area, (2) apply a preload between the vehicle and the surface to increase the attachment force, (3) use a peeling mode to detach the dry adhesion. Using these criteria, the design of a climbing robot should maximize the adhesion efficiency by adapting unique characteristics of the dry adhesives.

One of the first reported climbing robots successfully implemented with synthetic dry adhesives was the Mini-Wheg^{TM} [9] (Figure 1-2 (a)). Later on, a climbing robot, Waalbot, with a similar climbing strategy was reported by Murphy [12] (Figure 1-2 (b)). Both of the robots use wheels with some adhesive pads attached. The idea behind these climbing robots is to use a simple mechanism to achieve preloading and peeling for attaching and detaching the adhesive. The advantage of the wheel design is that the motors required for driving are small and, therefore, the weight and size of the robot decrease significantly. However, the disadvantages include: a) the need for a 'tail' to preload the adhesive, or else the robot will flip over and fall down; b) steering difficulties, e.g. turning locally; c) the wheels are only able to run on continuous trail (i.e., could not overcome gaps); d) no active control of the direction of attaching and detaching adhesive as they are predefined by the geometry of the wheel. Waalbot is reported to be able to climb on vertical surfaces at a velocity of 6 mm/s, and is capable of turning and transiting between vertical and horizontal surfaces, but the transition is not robust as it can get stuck in corners.

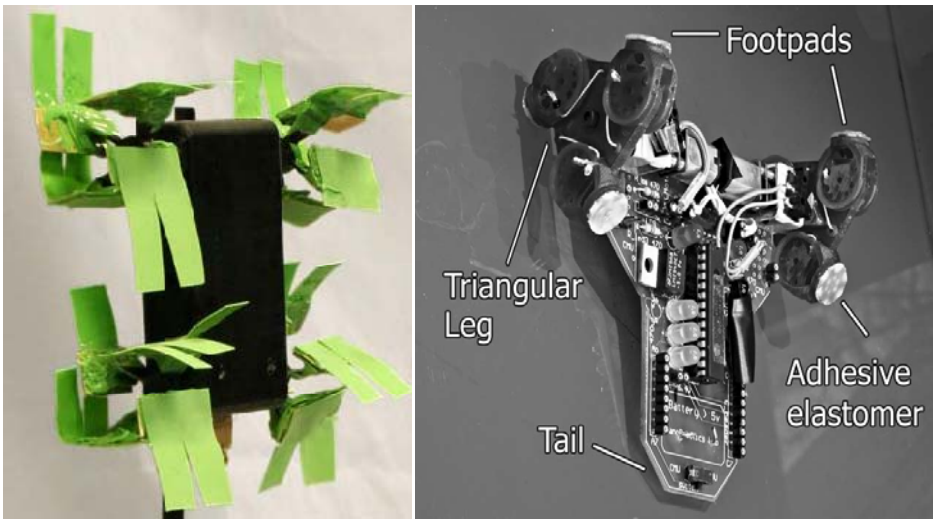

(a) **(b)**

Figure 1-2: Wheel climbing robots. (a) Mini-Wheg™ with a 25cm tail (picture cited from website of Mini-Wheg™ from Case Western Reserve University [9]). (b) Waalbot (picture cited from [12]).

Some other climbing robots intended to mimic geckos are shown in Figure 1-3. GeckoBot (Figure 1-3 (a)), reported by Unver et al. in 2006 [10], used elastomer adhesives in each foot. This robot is able to climb on smooth surface up to 85°, but it cannot steer at surface angles beyond 45°. Extra motors are provided for peeling adhesives. Diagonal feet are actuated simultaneously; therefore, the tail is included to provide the third support point for stable adhesion to the wall. Stickybot (Figure 1-3 (b)), reported by Kim et al. in 2007 [11], uses directional adhesive and has a similar but more sophisticated construction as GeckoBot. The robot is able to climb on vertical surfaces but cannot steer. The robot is highly conformable to climbing surfaces: its body and feet are designed to conform to uneven planes with soft and deformable structures. The robot is

under-actuated, having 38 degrees of freedom (DOF) but only actively controlled by 12 servo motors. Each toe is embedded with a steel string, which is pulled by an extra servo motor, causing a peeling movement. However, the adhesive constrained its ability on climbing smooth surfaces. Its ability to steer and transit is also limited by its design.

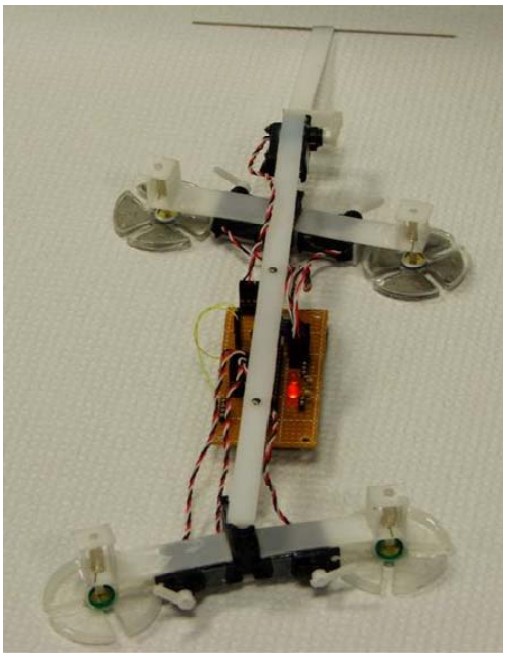

(a)

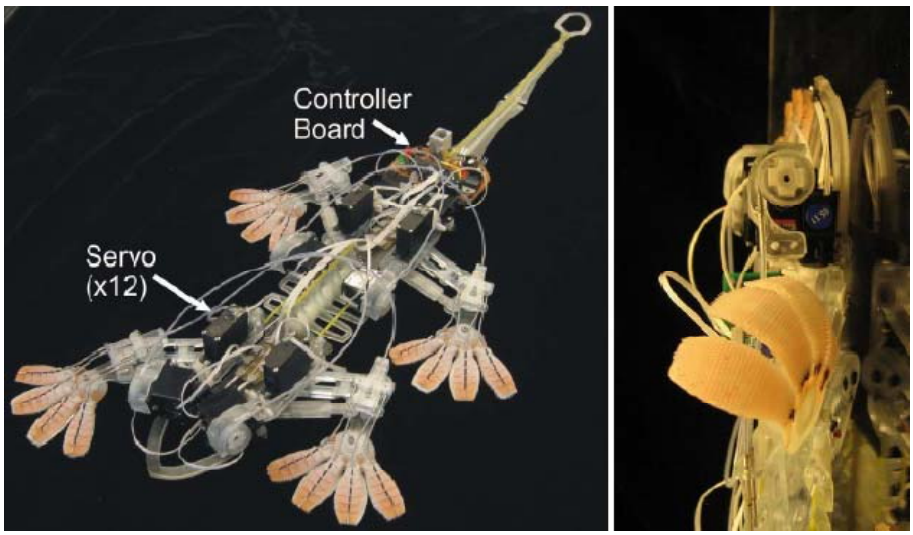

(b)

Figure 1-3: Gecko-inspired robots. (a) GeckoBot (picture cited from [10]). (b) StickyBot (picture cited from [11]).

As synthetic dry adhesion has not been available until recent years, some researchers used micro-spines to enable their robots to climb on rough surfaces. Spinybot (Figure 1-4 (a)), introduced by Kim et al., used arrays of micro-spines and compliant feet design [25]. The robot is able to climb on vertical concrete walls but not on smooth surfaces. Also it is not able to steer. Only one actuator is used in moving the two sets of legs, which are identified by red and blue colors in Figure 1-4 (a). A more complicate hexapod, the RiSE robot (Figure 1-4(b)) was introduced in [26]. With the help of an active tail, this robot mimicks a cockroach and is able to climb vertically and transit from vertical to horizontal surfaces. The legs of the RiSE robot are also compliant to the surface with a four-bar-linkage mechanism. However, because the robot has many actuators and electronics, it is very heavy (3 kg in comparison to others in the order of several hundred grams).

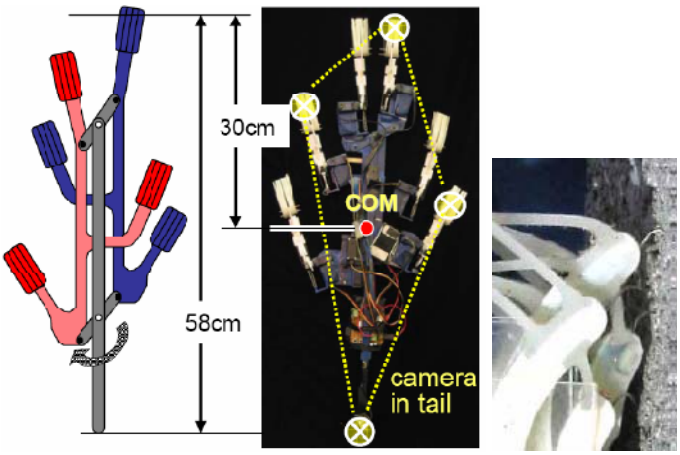

(a)

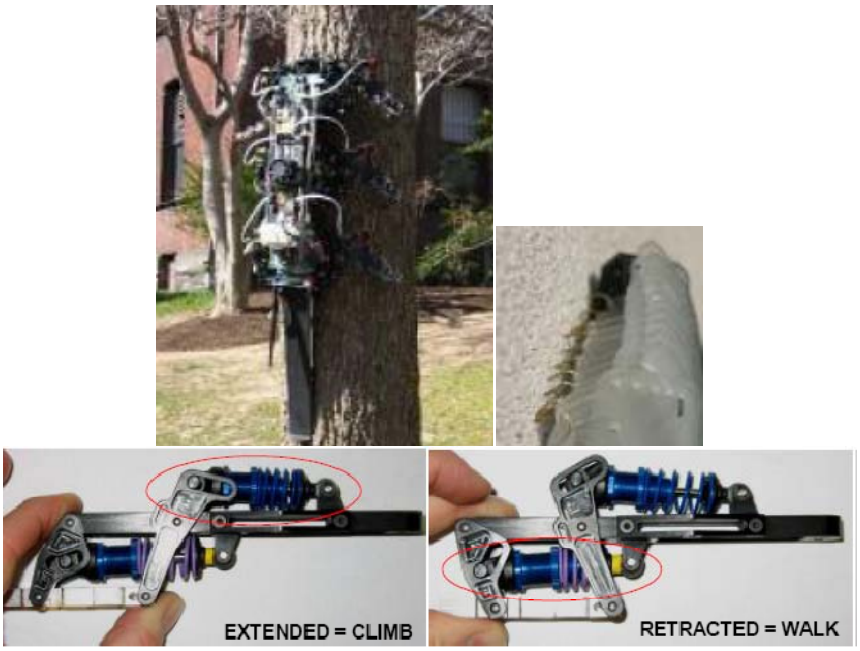

(b)

Figure 1-4: Spine embedded climbing robots. (a) SpinyBot and a close-up of the foot (Pictures cited from [25]). (b) the RiSE robot climbing on a tree (upper-left), close-up of foot (upper-right) and compliant foot design (lower). (Picture cited from [26]).

By investigating most of the existing climbing robots, including those introduced above, no existing general climbing machine can achieve versatile tasks. Successful climbing robots are designed for specific tasks, e.g., cleaning windows, climbing on ferrous flat surfaces, climbing inside or outside of tubes for inspection. The existing robots are unable to climb on other surfaces than those they were originally designed for. Upon encountering unexpected surfaces, (e.g., convex, gaps, or obstacles) the robot will fail to stick to the wall which may result in fatal damage. The performance of the robots previously introduced summarized in Table 1-1. The research in this thesis is to develop a climbing robot that can potentially overcome the limitation of existing robots.

Table 1-1: Comparison among exsiting climbing robot that use micro/nano adhesion structures

	Leg/ wheel	DOF (motor)	Tail	Weight (g)	Size (mm)	Surface	Steering	Transfer	Speed
Mini-Wheg™ (PSA[2] and dry adhsion)	Wheel	N/A (1)	yes (PSA: no)	76 g (PSA) 110 g/132 g (dry adhesion, 6.6 cm/25 cm tail)	54×89 (thickness not given)	Smooth, 6.6 cm tail – 60°, 25 cm tail – 90°	yes	yes	5.8 cm/s (PSA vertical sruface) 8.6 cm/s (dry adhesion 60 deg surface)
Waalbot	Wheel	N/A (2)	yes	69 g	130×50×123	Smooth, up to 110° surface	yes	yes, not reliable (stuck in corners)	6 mm/s (straight) 37°/s (steering)
Geckobot	Leg	1 (7)	yes (100 mm)	100 g	190×110 (exclude tail, thickness not given)	Smooth, up to 85° surface	yes (no in surface angle 45°)	no	5 cm/s (ground), 4 cm/s (tilt surface)
Stickybot	Leg	38 (12)	yes	370 g	600×200×60	Smooth, up to 110° surface	no	no	24 cm/s (ground), 4 cm/s (tilt surface),
Spinybot	Leg (micro-spine)	1 (7)	yes	400 g	580×300 (COM to wall: 10 mm)	Rough	no	no	2.3 cm/s (vertical surface)
RiSE robot	Leg (micro-spine)	12 (12)	yes	3000 g	2500 (body length, others not given)	Rough, 90° on carpet, 55°on wood	yes	yes	17 cm/s (vertical carpet), 24cm/s (asphalt ground)

[2] PSA stands for pressure sensitive adhesion, such as Scotch® tape.

1.2 Objective

A successful climbing robot should be able to handle various tasks which conventional mobile robots cannot achieve. Compared to wheeled robots, legged robots possess greater mobility, e.g., turning locally and versatility locomoting in different terrains. By considering the use of dry adhesion for climbing, a legged robot may be considered to be a preferable solution because of its flexibility of movement, which could allow changing orientation and direction of the feet to comply with the anisotropic property of the synthetic dry adhesive.

Randall [27] specified several properties a robot should have to agilely walk: (1) highly adaptive to environment, (2) lightweight, (3) reliable and robust, (4) high force to weight ratio, (5) navigate using 3D path planning, (6) possibility to 'learn from experience', (7) have reliable and robust control system to drive various actuators, (8) be able to sense its environment to achieve tasks efficiently, and (9) design functions in module in order to 'plug and play' in specific tasks. For a wall-climbing robot, additional requirements are emphasized to achieve the particular climbing feature. The robot should be able to: (1) transit between horizontal and vertical surfaces in all directions, (2) negotiate obstacles and ledges, (3) prevent falling due to occasional adhesion failure, and (4) maximize adhesion efficiency.

For a climbing machine, the weight and, therefore, miniaturization should have higher priority than a usual walking machine. Miniaturized robots can also take advantage of their reduced size to go through narrow spaces for tasks not

suitable for bigger robots. The climbing robot, therefore, should be designed to have compact structures to maintain low body weight and small size.

With millions of years of evolution, spiders, specifically hunting spiders, survive and thrive with their hunting skills. Compared to geckos, they have a rigid body and legs instead of flexible muscles and skin; this property is much easier to mimick in engineering design. The spider adhesion mechanism, which relies on multi-scale hairs, is compliant to surfaces and can be replicated by synthetic dry adhesion fabrication technology. With these special properties, spiders are a preferable bio-mimetic subject for the design of engineering climbing robots.

To summarize, the robot designed in this thesis was designed to: 1) be miniaturized and lightweight; 2) rely on dry adhesives; and 3) have a legged configuration. Using solutions found in spiders, the robot in this thesis should be able to adapt to different surfaces, shapes and materials.

1.3 Thesis outline

The layout of the remaining parts of this thesis is arranged as follows: Chapter 2 first presents the basic configurations of size, weight, and construction according to the objective of the research. Thereafter, analyses of the kinematic properties are performed. Equations are developed to calculate the direct kinematics and inverse kinematics for legs in swing phase, which is the instant while the legs are moving in air without touching a fixed base. Inverse kinematic equations are also used to control the robot body movement. Lastly the local

ground coordinate is introduced to further implementation of kinematic equations while the robot is moving in sequential steps.

Chapter 3 introduces two prototypes developed during this research and presents their mechatronic design. A comparison between the two prototypes is discussed.

Chapter 4 demonstrates the validation of the kinematic equations and the development of simplified control strategies. Tests are performed to determine the power saving trajectories for the feet to release adhesion in order to make reliable contact position for reinforced adhesion. Validation of an algorithm, which was developed in MENRVA Group to reduce reaction force between adhesive feet and the wall, is performed. Test results are discussed that show actively controlled joint torques of the robot can reduce significantly the adhesive requirement.

Chapter 5 proposes future development of an under-actuated system. Preliminary joint design is introduced and the robotic concept design is explained. The advantage of an under-actuated system is that it could reduce robot weight and cost of future platforms.

Chapter 6 presents the conclusion of all the preliminary results and points out future work towards a fully reliable bio-mimetic climbing robot.

1.4 Thesis contributions

The use of dry adhesion relying on van der Waals forces that are not constrained by surface materials and shapes opens a new area of research for

climbing robot development. The contribution of this thesis is utilizing the advantages of synthetic dry adhesion to investigate the development of a spider-inspired robot which possesses the ability to maneuver in different terrains.

Firstly, by considering the different terrains the robot might encounter, a basic configuration for a climbing robot is proposed. Secondly, kinematic equations set for the climbing robot are proposed. Assigning coordinates to control the robot in successive steps is introduced based on kinematic analysis. Furthermore, with specific application to the climbing robot, the theory of peeling the thin film is revisited and applied in releasing adhesion. A power saving trajectory is proposed and proved in a power consumption test. Finally, a robot prototype is developed that is able to climb a vertical smooth surface with a synthetic dry adhesive attached. The robot design is validated and the potential better climbing mechanism is shown as planned.

Overall, the contribution of this work is developing a climbing robot which has the potential to possess high mobility and the ability to fully utilize the advantage of dry adhesion.

CHAPTER 2 ROBOT DESIGN CONFIGURATIONS AND KINEMATIC ANALYSIS

2.1 Design configurations

In the early design phase, different configurations for the robot design were analyzed according to the objectives of this research. The synthetic dry adhesion we had recently fabricated could produce a maximum adhesive force of around 0.9 kg/cm^2 when manually preloaded [28]. Usually, without active preloading (e.g. pushing the adhesive area by hand), the effective contact area of the adhesive lowers to 10-20% of the total area. Therefore, the generated adhesive force was reduced to 100-200 g/cm^2. In order to keep the safety factor of the climbing robot on a reasonable level, we set the maximum weight of the robot at around 200g and the total adhesive area at around 20 cm^2 (a safety factor at more than 10).

Similarly to spiders, the robot was designed to have multiple legs, which provide high flexibility to potentially avoid obstacles and walk on rough terrains. Instead of using eight legs as in spiders, the proposed robot was designed with six legs in order to reduce its complexity and weight.

In order to enlarge the work-space of each leg and provide high potential dexterity[3] to the robot, a specific configuration was chosen as proposed in Figure 2-1. Three joints were used in each leg. Two of them located at the edge of the

[3] Dexterity is the ability of performing tasks.

robot platform with cross axes, while the joint in the middle of the leg has a parallel axis with the second joint. This mechanism is known as an anthropomorphic arm. The work-space of the anthropomorphic arm is within the sphere of the full leg length, which means the tip of the leg can reach every point within a sphere of that size. For the sake of clarity, from the inside out, the three joints are named the hip, shoulder and elbow joints. Similarly, the second link (from the shoulder to the elbow joint) is called the femur and the third link (from the elbow to the end tip of the leg) is called the tibia. The six legs are arranged 60 degrees apart in a circle to better mimick the spider instead of placing them in two rows as in most engineering hexapods developed so far. The hexagonal arrangement allows for more gaits and is easier to achieve the desired direction than the rectangular platform [29]; this configuration could facilitate transition among perpendicular surfaces. All joints in the six legs were controlled separately, which guarantees the robot's dexterity. Based on previous considerations, the basic configuration of the mechanical design was a 200 g hexapod having three actuators per leg, with all legs arranged symmetrically around a circular platform.

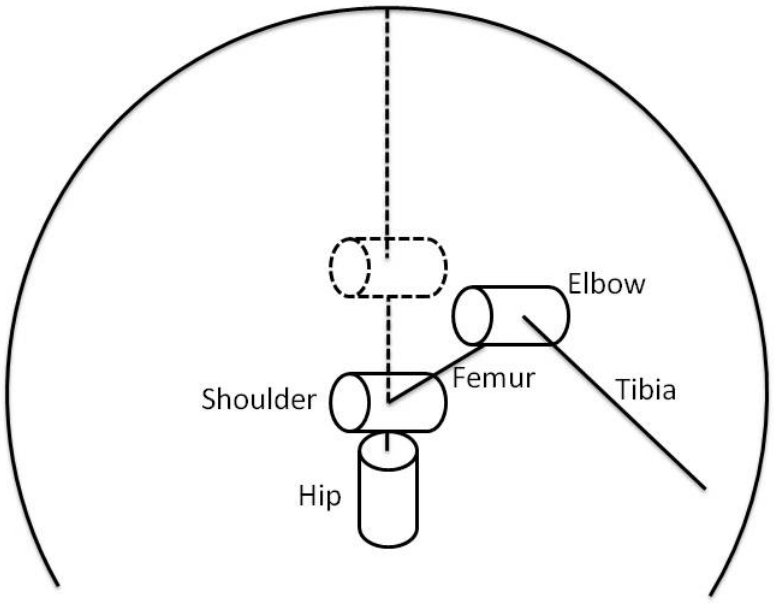

Figure 2-1: Anthropomorphic arm and its workspace.

2.2 Introduction to kinematic analysis

Based on the design configuration above, kinematic analysis was performed to analyze two scenarios. The first one concerns the case in which a single leg is in its swing phase; the leg is analyzed as a 3 DOF serial manipulator. The second scenario concerns the entire robot when all the legs are attached to a surface; in this case, the end-effector is the robot's body and the structure should be analyzed as a parallel robot.

2.3 First scenario: serial manipulator analysis

Each leg without a fixed end to the ground was considered as a serial manipulator or an open chain. The three revolute joints provided 3 DOF to the mechanism. Two configurations, called configuration 1, which has no intersected

joints axes in the hip and shoulder joints, and configuration 2, which has intersected joints axes in the hip and shoulder joints, were considered as presented in the following sections.

2.3.1 Direct kinematics

Given the joint variables, we used direct kinematics to solve the position of the end-effector, which is the end tip of the leg in this situation, with given joint variables. Configuration 1, which reduces the body thickness relevant to lower the center of mass, is represented in Figure 2-2. This figure also shows the coordinates assignment for this configuration. All the revolute joints rotate about their z-axis. In this configuration the axes of the hip and shoulder joint are not intersecting. Denavit-Hartenberg parameters (DH parameters) for this configuration are listed in Table 2-1.

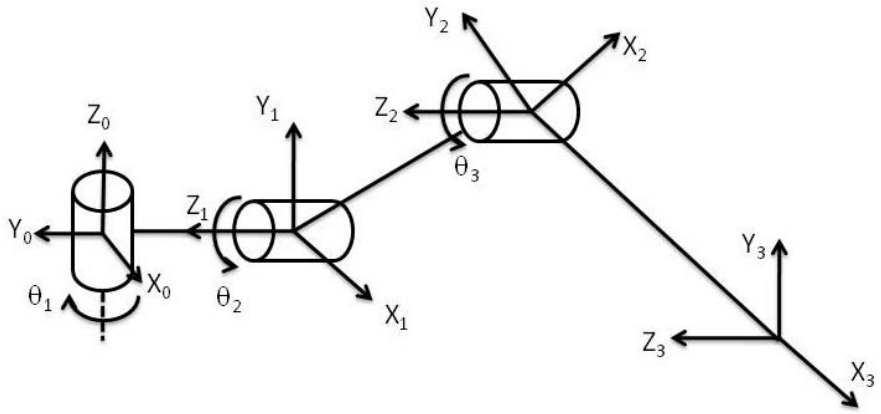

Figure 2-2: Coordinate assignment in configuration 1.

Table 2-1: DH parameters in serial manipulator case for configuration 1.

Link	a_i	α_i	d_i	θ_i
1	a_1	π/2	0	θ_1
2	a_2	0	0	θ_2
3	a_3	0	0	θ_3

The homogeneous transformation matrices for each joint are:

$$A_0^1(\theta_1) = \begin{bmatrix} c_1 & 0 & s_1 & a_1c_1 \\ s_1 & 0 & -c_1 & a_1s_1 \\ 0 & 1 & 0 & 0 \\ 0 & 0 & 0 & 1 \end{bmatrix} \quad (2\text{-}1)$$

$$A_1^2(\theta_2) = \begin{bmatrix} c_2 & -s_2 & 0 & a_2c_2 \\ s_2 & c_2 & 0 & a_2s_2 \\ 0 & 0 & 1 & 0 \\ 0 & 0 & 0 & 1 \end{bmatrix} \quad (2\text{-}2)$$

$$A_2^3(\theta_3) = \begin{bmatrix} c_3 & -s_3 & 0 & a_3c_3 \\ s_3 & c_3 & 0 & a_3s_3 \\ 0 & 0 & 1 & 0 \\ 0 & 0 & 0 & 1 \end{bmatrix} \quad (2\text{-}3)$$

Therefore, the direct kinematics transformation matrix is

$$T_0^3(\theta_1\theta_2\theta_3) = A_0^1A_1^2A_2^3$$

$$= \begin{bmatrix} c_1c_{23} & -c_1s_{23} & s_1 & c_1(a_1 + a_2c_2 + a_3c_{23}) \\ s_1c_{23} & -s_1s_{23} & -c_1 & s_1(a_1 + a_2c_2 + a_3c_{23}) \\ s_{23} & c_{23} & 0 & a_2s_2 + a_3s_{23} \\ 0 & 0 & 0 & 1 \end{bmatrix} \quad (2\text{-}4)$$

With a given set of joint variables, the position of the end-effector is calculated as a vector with respect to the robot base

$$\boldsymbol{p}\left(p_x, p_y, p_z\right) = [c_1(a_1 + a_2c_2 + a_3c_{23}), s_1(a_1 + a_2c_2 + a_3c_{23}), a_2s_2 + a_3s_{23}] \quad (2\text{-}5)$$

The second configuration, analyzed that we used is represented in Figure 2-3. This figure also shows the coordinate systems. The hip joint and the shoulder joint share the same origin at the geometric center of the second joint. All joints rotate about their z-axis. Notice z_0 and z_1 intersect at the coordinate origin. For this configuration, the DH parameters are specified in Table 2-2.

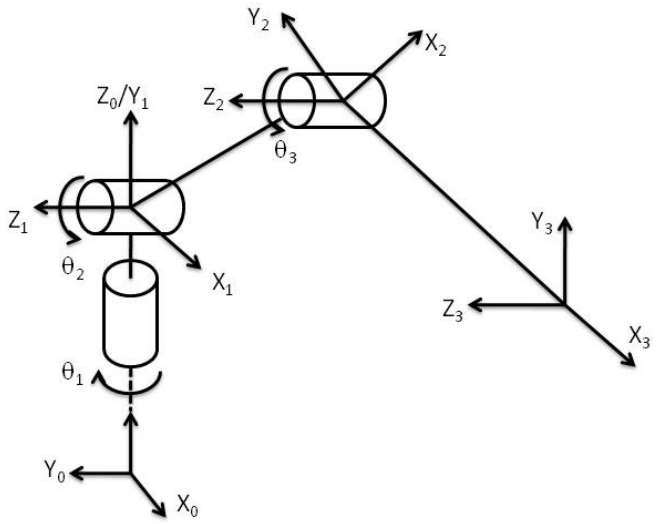

Figure 2-3: Coordinates assignment in configuration 2.

Table 2-2: DH parameters in serial manipulator for configuration 2.

Link	ai	αi	di	θi
1	0	π/2	0	θ1
2	a2	0	0	θ2
3	a3	0	0	θ3

The homogeneous transformation matrices for each joint are:

$$A_0^1(\theta_1) = \begin{bmatrix} c_1 & 0 & s_1 & 0 \\ s_1 & 0 & -c_1 & 0 \\ 0 & 1 & 0 & 0 \\ 0 & 0 & 0 & 1 \end{bmatrix} \quad (2\text{-}6)$$

$$A_1^2(\theta_2) = \begin{bmatrix} c_2 & -s_2 & 0 & a_2c_2 \\ s_2 & c_2 & 0 & a_2s_2 \\ 0 & 0 & 1 & 0 \\ 0 & 0 & 0 & 1 \end{bmatrix} \quad (2\text{-}7)$$

$$A_2^3(\theta_3) = \begin{bmatrix} c_3 & -s_3 & 0 & a_3c_3 \\ s_3 & c_3 & 0 & a_3s_3 \\ 0 & 0 & 1 & 0 \\ 0 & 0 & 0 & 1 \end{bmatrix} \quad (2\text{-}8)$$

where c_i and s_i denotes cosine θ_i and sine θ_i, respectively. Therefore the direct kinematics transformation matrix is:

$$T_0^3(\theta_1\theta_2\theta_3) = A_0^1A_1^2A_2^3 = \begin{bmatrix} c_1c_{23} & -c_1s_{23} & s_1 & c_1(a_2c_2 + a_3c_{23}) \\ s_1c_{23} & -s_1s_{23} & -c_1 & s_1(a_2c_2 + a_3c_{23}) \\ s_{23} & c_{23} & 0 & a_2s_2 + a_3s_{23} \\ 0 & 0 & 0 & 1 \end{bmatrix} \quad (2\text{-}9)$$

where s_{ij} denotes sine $(\theta_i + \theta_j)$.

With a given set of joint variables, the position of end-effector is calculated as a vector with respect to the robot base.

$$\boldsymbol{p}\left(\boldsymbol{p_x}, \boldsymbol{p_y}, \boldsymbol{p_z}\right) = [\boldsymbol{c_1}(\boldsymbol{a_2 c_2} + \boldsymbol{a_3 c_{23}}), \boldsymbol{s_1}(\boldsymbol{a_2 c_2} + \boldsymbol{a_3 c_{23}}), \boldsymbol{a_2 s_2} + \boldsymbol{a_3 s_{23}}] \tag{2-10}$$

2.3.2 Inverse kinematics

Inverse kinematics is used to solve the set of joint variables when given the position of the end-effector. In this thesis, the inverse kinematic problem was solved by geometrical analysis.

Given the end-effector position, vector $\boldsymbol{p}$ (p_x, p_y, p_z), with respect to the robot base frame, the hip joint angle was solved directly from vector $\boldsymbol{p}$, in both configurations:

$$\theta_1 = arctan\frac{p_y}{p_x} \tag{2-11}$$

Configuration 2 is first discussed for its simplicity. The 2D graph shown in Figure 2-4 was used for analyzing. The second and third link length is known, as is the magnitude of the vector $\boldsymbol{p}$. It should be noticed that there are two configurations for the same end-effector position (Figure 2-5). According to the law of cosines, θ_3 can be calculated in

$$\theta_3 = \mp arccos\frac{p_z^2 + p_x^2 - a_2^2 - a_3^2}{2a_2a_3} \tag{2-12}$$

where the negative value physically refers to the elbow up configuration and the positive value refers to the elbow down configuration.

Calculation of θ_2 is the sum of two parts: the angle between a_2 and $\boldsymbol{p}$, and the angle between the x_0 axis and $\boldsymbol{p}$, which is named α and β, respectively. The angle α can be calculated using the law of cosines, while β can be calculated directly using the vector components. Therefore, for both elbow up and elbow down configurations, the end-effector is in the position of positive β:

$$\theta_2 = |\alpha| + \beta = arccos\frac{p_z^2 + p_x^2 + a_2^2 - a_3^2}{2a_2\sqrt{p_x^2 + p_z^2}} + arctan\frac{p_z}{p_x} \qquad (2\text{-}13)$$

For the situation where the end-effector is in the position of negative β:

$$\theta_2 = \pm|\alpha| + \beta = \pm arccos\frac{p_z^2 + p_x^2 + a_2^2 - a_3^2}{2a_2\sqrt{p_x^2 + p_z^2}} + arctan\frac{p_z}{p_x} \qquad (2\text{-}14)$$

where the negative value physically refers to the elbow up configuration and the positive value refers to the elbow down configuration.

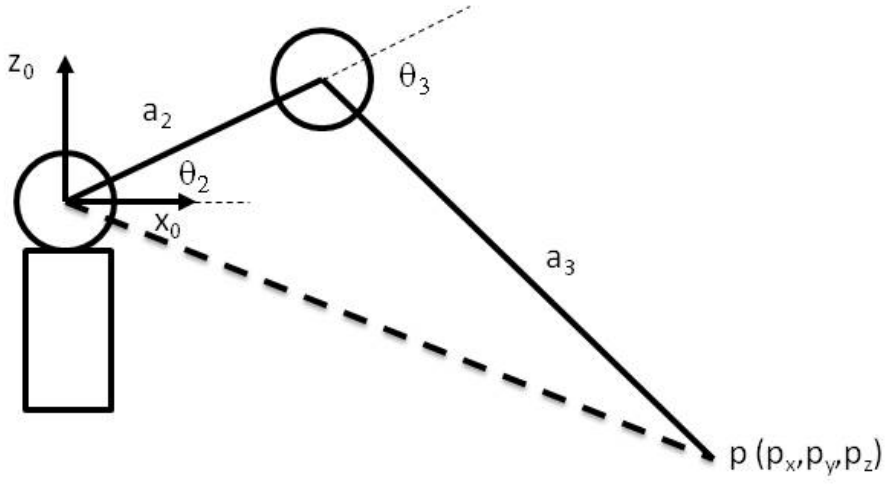

Figure 2-4: 2D graph for geometry analysis of configuration 2.

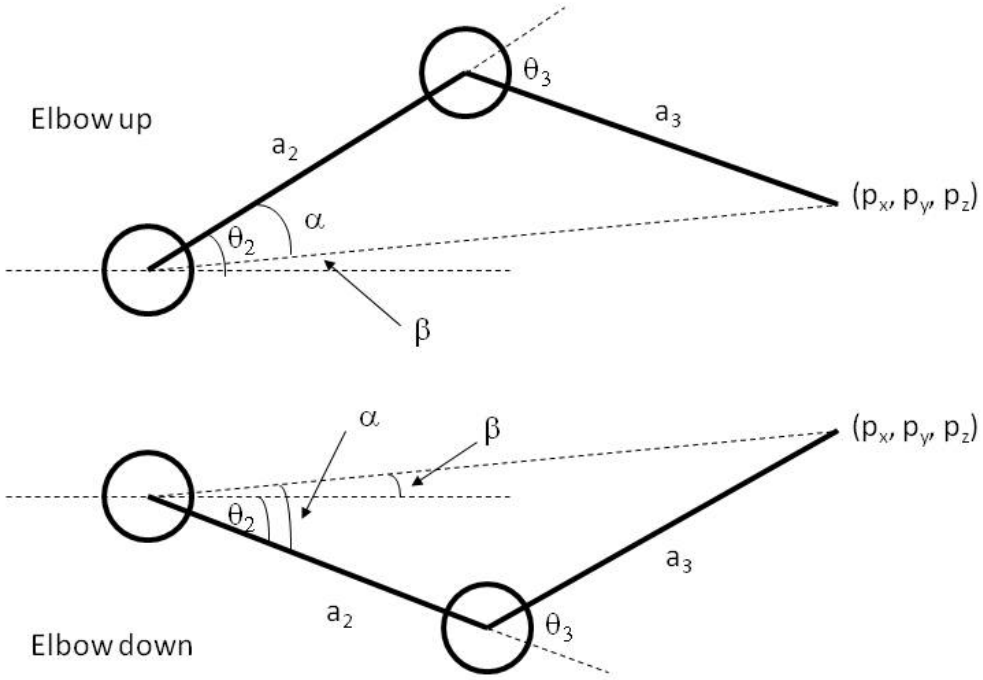

Figure 2-5: Two situations for the end effector reaching same position: elbow up and elbow down.

The 2D graph shown in Figure 2-6 was used for analyzing configuration 1. It should be noticed that the first link length, a_1, has an offset in the x-y plane compared to configuration 2. In order to use the law of cosines as was done for configuration 2, another vector, ***p'***, was used to represent the vector from the shoulder joint coordinate to the end-effector.

The relationship between ***p*** and ***p'*** is

$$p'_x = p_x - a_1 cos\theta_1 \tag{2-15}$$

$$p'_y = p_y - a_1 sin\theta_1 \tag{2-16}$$

$$p'_z = p_z \tag{2-17}$$

By using the same approach for configuration 2,

$$\theta_2 = \pm arccos \frac{p'^2_z + p'^2_x + a_2^2 - a_3^2}{2a_2\sqrt{p'^2_x + p'^2_z}} + arctan \frac{p'_z}{p'_x} \tag{2-18}$$

where the negative value physically refers to the elbow up configuration and the positive value refers to the elbow down configuration.

$$\theta_3 = \mp arccos \frac{p'^2_z + p'^2_x - a_2^2 - a_3^2}{2a_2a_3} \tag{2-19}$$

The negative value refers elbow up position whereas positive value refers to the elbow down position.

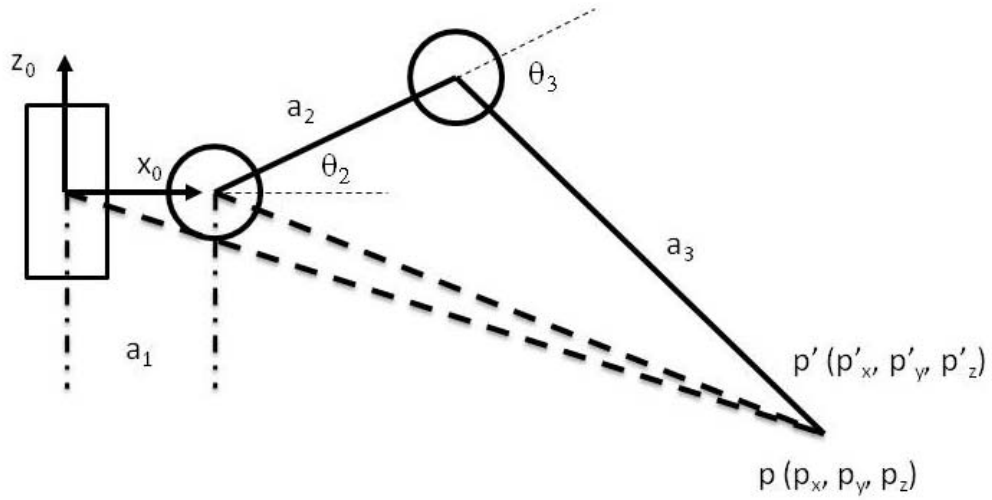

Figure 2-6: 2D graph for geometry analysis of configuration 1.

2.3.3 Singularity

By observation, the singular position of the robot's leg occurs when

$$\theta_3 = 0 \; or \; \pi \tag{2-20}$$

which is the position in which the leg is fully stretched out and folded back. Another situation that causes a singularity occurs when

$$p_x = p_y = 0 \tag{2-21}$$

which is the position when the leg tip is aligned to the z_0 axis.

By analyzing the Jacobian of the manipulator, the above conclusions were validated in analytically.

The Jacobian is calculated by:

$$J = \begin{bmatrix} z_0 \times (p - p_0) & z_1 \times (p - p_1) & z_2 \times (p - p_2) \\ z_0 & z_1 & z_2 \end{bmatrix} \tag{2-22}$$

In configuration 1, the position vector of each joint is:

$$p_0 = \begin{bmatrix} 0 \\ 0 \\ 0 \end{bmatrix} \tag{2-23}$$

$$p_1 = \begin{bmatrix} a_1 c_1 \\ a_1 s_1 \\ 0 \end{bmatrix} \tag{2-24}$$

$$p_2 = \begin{bmatrix} c_1(a_1 + a_2 c_2) \\ s_1(a_1 + a_2 c_2) \\ a_2 s_2 \end{bmatrix} \tag{2-25}$$

$$p = \begin{bmatrix} c_1(a_1 + a_2 c_2 + a_3 c_{23}) \\ s_1(a_1 + a_2 c_2 + a_3 c_{23}) \\ a_2 s_2 + a_3 s_{23} \end{bmatrix} \tag{2-26}$$

In configuration 2, the position vector of each joint is:

$$p_0 = p_1 = \begin{bmatrix} 0 \\ 0 \\ 0 \end{bmatrix} \tag{2-27}$$

$$p_2 = \begin{bmatrix} a_2 c_1 c_2 \\ a_2 s_1 c_2 \\ a_2 s_2 \end{bmatrix} \tag{2-28}$$

$$p = \begin{bmatrix} c_1(a_2 c_2 + a_3 c_{23}) \\ s_1(a_2 c_2 + a_3 c_{23}) \\ a_2 s_2 + a_3 s_{23} \end{bmatrix} \tag{2-29}$$

The unit vector of the revolute axis in each joint, in both prototypes, can be computed as:

$$\mathbf{z_0} = \begin{bmatrix} \mathbf{0} \\ \mathbf{0} \\ \mathbf{1} \end{bmatrix} \tag{2-30}$$

$$z_1 = z_2 = \begin{bmatrix} s_1 \\ -c_1 \\ 0 \end{bmatrix} \tag{2-31}$$

For both configurations:

$$J = \begin{bmatrix} -s_1(a_2c_2 + a_3c_{23}) & -c_1(a_2s_2 + a_3s_{23}) & -a_3c_1s_{23} \\ c_1(a_2c_2 + a_3c_{23}) & -s_1(a_2s_2 + a_3s_{23}) & -a_3s_1s_{23} \\ 0 & a_2s_2 + a_3s_{23} & a_3c_{23} \\ 0 & s_1 & s_1 \\ 0 & -c_1 & -c_1 \\ 1 & 0 & 0 \end{bmatrix} \tag{2-32}$$

Only the first three rows are linearly independent, which denotes the relationship between joint velocity and end-effector linear velocity. Let J_p represent the first three rows of J. The manipulator does not allow arbitrary angular velocity because the last three rows of the Jacobian, which represent angular velocity of the end-effector, are not linearly independent.

The determinant of J_p is

$$\det[J_p] = \begin{vmatrix} -s_1(a_2c_2 + a_3c_{23}) & -c_1(a_2s_2 + a_3s_{23}) & -a_3c_1s_{23} \\ c_1(a_2c_2 + a_3c_{23}) & -s_1(a_2s_2 + a_3s_{23}) & -a_3s_1s_{23} \\ 0 & a_2s_2 + a_3s_{23} & a_3c_{23} \end{vmatrix} \quad (2\text{-}33)$$

$$= -a_2a_3s_3(a_2c_2 + a_3c_{23})$$

When $s_3 = 0$ or $a_2c_2 + a_3c_{23} = 0$, $det[J_p] = 0$, reaching the singular position. These are the conditions previously obtained by geometrical inspection.

2.4 Second scenario: parallel platform analysis

For the hexapod robot, the basic requirement for holding the robotic platform statically stable is having at least three legs contacting the ground (the robotic ankles are modeled as spherical joints). The attached legs and the robotic platform then form a parallel manipulator or closed chain mechanism. The body of the robot becomes the end-effector and it is the object to be controlled. Therefore, the following analysis focuses on the inverse kinematics of the parallel configuration presented in Figure 2-7.

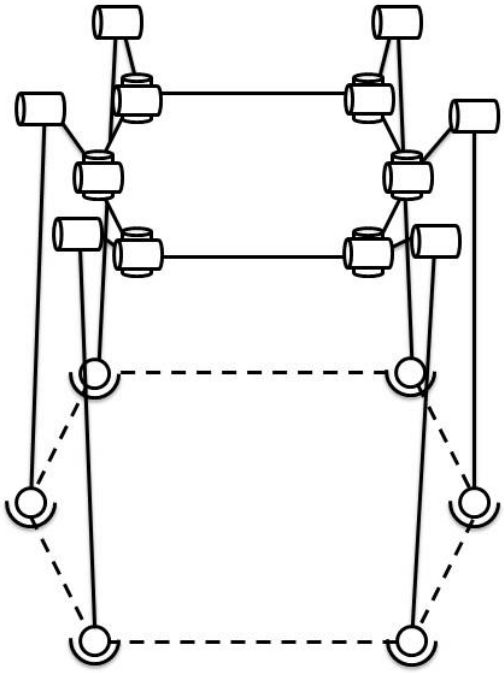

Figure 2-7: Robot model shown in parallel platform.

By examining the DOF of the parallel manipulator, the number of parameters needed to fully control the robot is defined. Each leg has 4 joints and 2 links. The ground and the robot body were counted as one link in the calculation. The DOF of the the robot was computed using the Grubler criterion; when 3 legs are attached to the ground, the criterion yields:

$$F = \lambda(n - j - 1) + \sum_i f_i = 6(11 - 12 - 1) + (3 \times 3 + 3 \times 3) = 6 \quad (2\text{-}34)$$

When 4 legs attach to the ground, the criterion yields:

$$F = \lambda(n - j - 1) + \sum_i f_i = 6(14 - 16 - 1) + (4 \times 3 + 3 \times 4) = 6 \quad (2\text{-}35)$$

When 5 legs attach to the ground, the criterion yields:

$$F = \lambda(n - j - 1) + \sum_i f_i = 6(17 - 20 - 1) + (5 \times 3 + 3 \times 5) = 6 \quad (2\text{-}36)$$

And, when 6 legs attach to the ground, the criterion yields:

$$F = \lambda(n - j - 1) + \sum_i f_i = 6(20 - 24 - 1) + (6 \times 3 + 3 \times 6) = 6 \quad (2\text{-}37)$$

where *n* denotes the number of links, *j* denotes the number of joints, *λ* denotes dimensions of the moving mechanism. Notice that the calculations always yield six DOF in all cases.

Above calculation proved that when at least 3 legs are attached to the ground, the parallel manipulator will always have 6 DOF, which means 6 independent parameters are required as input to control its position. The six parameters representing six DOF were designed to be (p_x, p_y, p_z, α, β, γ), where (p_x, p_y, p_z) denote the three coordinates of vector $\boldsymbol{p}$, while α, β, γ denote the Euler angle controlling the orientation of the robotic platform with respect to the ground.

In order to investigate the inverse kinematics of the platform, the robot was simplified by replacing the elbow joint by a prismatic joint. The variable associated with the prismatic joint is presented as $\boldsymbol{d}_i$ (i=1, 2, 3, 4, 5, 6). By

knowing the geometrical parameters of the triangle formed by the foot, shoulder and elbow joints, θ_3 and θ_2 were obtained using the same approach previously used in the serial manipulator case. The coordinates and vectors designation is shown in Figure 2-8. It is assumed that in the initial posture of the robot, all the 6 legs have identical joint variables. The contacting feet were represented as spherical joints, which allow the end tip of the leg to rotate about all directions. This model was used to represent the compliant feature of the polymer adhesive feet, which were attached to the end of the robotic leg of the prototype described in the following sections. The robot body coordinates (*x, y, z*) are located at the center of the robot body. The ground coordinates (*u, v, w*) are located at the center of the equilateral hexagon formed by the six feet in contact. Vector b_i denotes the fixed position of the hip joint with respect to the main coordinates. Vector $\boldsymbol{c_i}$ denotes the fixed position of the feet in the ground plane. Vector ***p*** is the position vector of the robot body with respect to the ground coordinate. Vector ***q*** is the position vector of the feet with respect to the robot body.

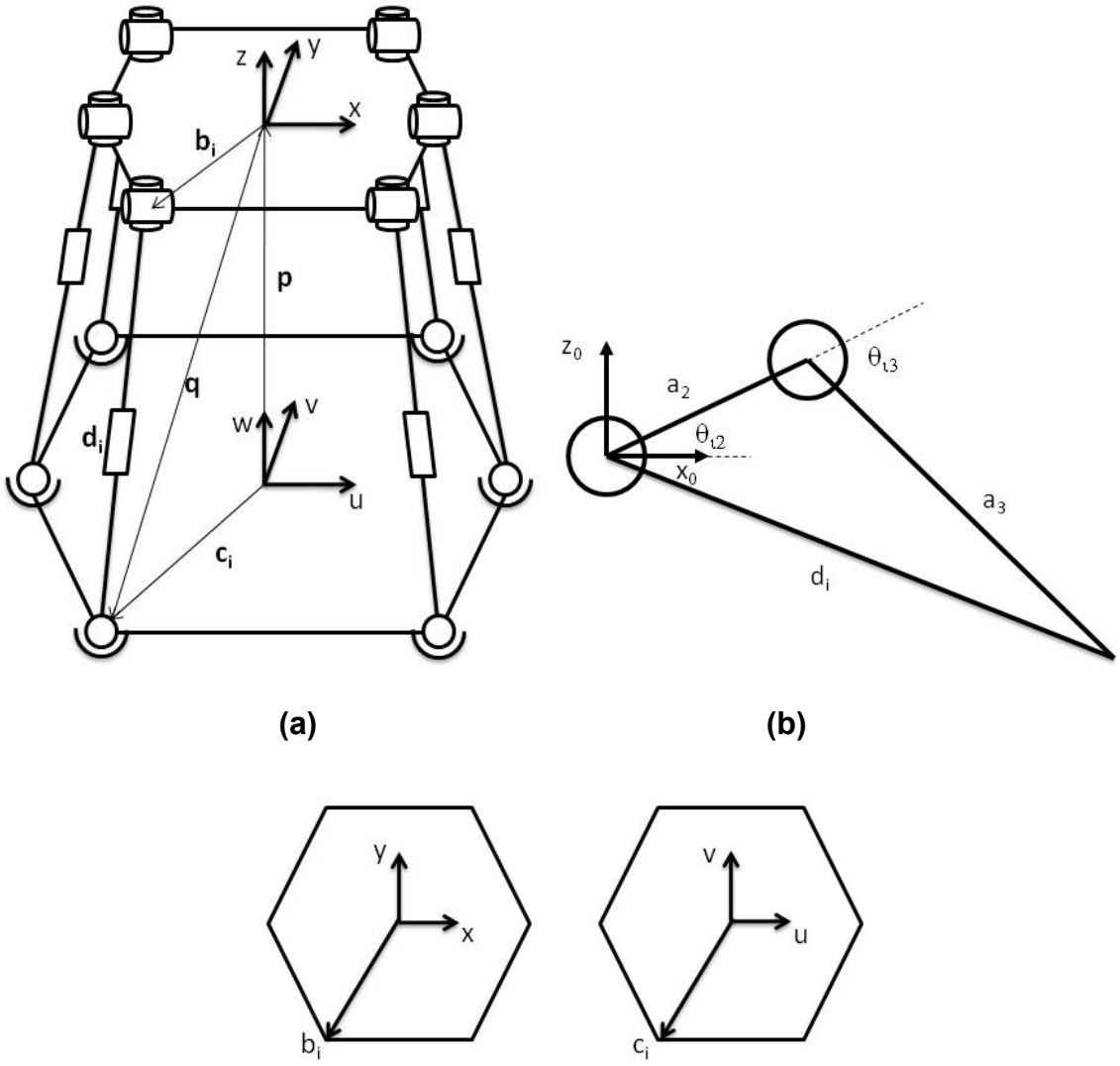

Figure 2-8: Geometry representation of parallel robot situation: (a) Simplified main parallel manipulator. (b) Relationship between simplified model and the original leg. (c) Top view of robot body plane (Plane B) and the ground plane (Plane C).

The rotation matrix of the robot's body coordinates with respect to the ground coordinates is

$$R_B^C = \begin{bmatrix} u_x & v_x & w_x \\ u_y & v_y & w_y \\ u_z & v_z & w_z \end{bmatrix} = \begin{bmatrix} c\alpha c\beta c\gamma - s\alpha s\gamma & -c\alpha c\beta s\gamma - s\alpha c\gamma & c\alpha s\beta \\ s\alpha c\beta c\gamma + c\alpha s\gamma & -s\alpha c\beta s\gamma + c\alpha c\gamma & s\alpha s\beta \\ -s\beta c\gamma & s\beta s\gamma & c\beta \end{bmatrix} \quad (2\text{-}38)$$

Vector $\boldsymbol{q_i}$ is calculated by

$$q_i = R_C^B(c_i - p) = R_B^{C^T}(c_i - p) \quad (2\text{-}39)$$

Then vector $\boldsymbol{d_i}$ is known by

$$d_i = q_i - b_i \quad (2\text{-}40)$$

The magnitude of $\boldsymbol{d_i}$ is

$$|d_i| = [q_i - b_i]^T[q_i - b_i] \quad (2\text{-}41)$$

The first variable is given by

$$\theta_{1i} = \arctan\frac{\mathrm{d_{iy}}}{\mathrm{d_{ix}}} - \arctan\frac{\mathrm{b_{iy}}}{\mathrm{b_{ix}}} \quad (2\text{-}42)$$

where $\boldsymbol{d_{iy}}$ and $\boldsymbol{d_{ix}}$ denote the second and first number representing the *y* and *x* axes in vector $\boldsymbol{d_i}$, respectively.

Figure 2-8 (b) was used to analyze each leg. By applying the law of cosine, the elbow joint was calculated by

$$\theta_{3i} = \mp arccos \frac{|d_i|^2 - a_2^2 - a_3^2}{2a_2 a_3} \tag{2-43}$$

By implementing an approach similar to the one used in the serial manipulator, we obtained:

$$\theta_{2i} = \pm arccos \frac{|d_i|^2 + a_2^2 - a_3^2}{2a_2|d_i|} + arctan \frac{d_{iz}}{d_{ix}} \tag{3-44}$$

The notations are the same used as those in the previous section for the elbow up and elbow down situations.

It should be noticed that the shoulder and elbow joints equations are only applied to configuration 2. In configuration 1, different equations are needed in a similar way described in section 2.3.

2.5 Introduction to the local ground coordinate

In section 2.4, the ground coordinates were fixed to the ground as the geometrical analysis did not consider the robot moving in steps. For simple movements, such as walking straight or turning on flat surfaces, the fixed ground coordinates could be used without other arrangements. However, in some complicated tasks, such as transferring between different planes and avoiding obstacles, the local ground coordinate might be more convenient for gait planning. The local ground coordinate is always changing while different groups of legs detach, move, and attach to a surface again. For example, while the robot

is applying a tripod gait, the 6 legs are divided into 2 groups: namely group A for legs 1, 3, 5, and group B for legs 2, 4, 6 (Figure 2-9 (a)). The initial position is 6 legs in contact to the ground, as mentioned in section 2.4 (Figure 2-9 (b)). The local ground coordinate stays at the geometric center of the three contacting feet while group A detaches and again comes in contact with the ground (Figure 2-9 (c)). Once group A touches the ground, a new local ground coordinate is calculated according to the leg positions of group A. By using the notations defined in section 2.4, Plane C of the new coordinate system will be located at the plane defined by the 3 contacting feet in group A. The origin of the robotic platform coordinates then has its projection to Plane C in order to calculate the new origin of the local ground coordinate, and the projection line defines the W axis (Figure 2-9 (d)). This calculation is a one-cycle process used to update the local ground coordinate. The conceived strategy defines that, before one group of legs detach, the other group should first contact the surface in order to recalculate a new coordinate. This strategy may find suitable applications when the robot is coping with terrain adaptation or obstacle avoidance.

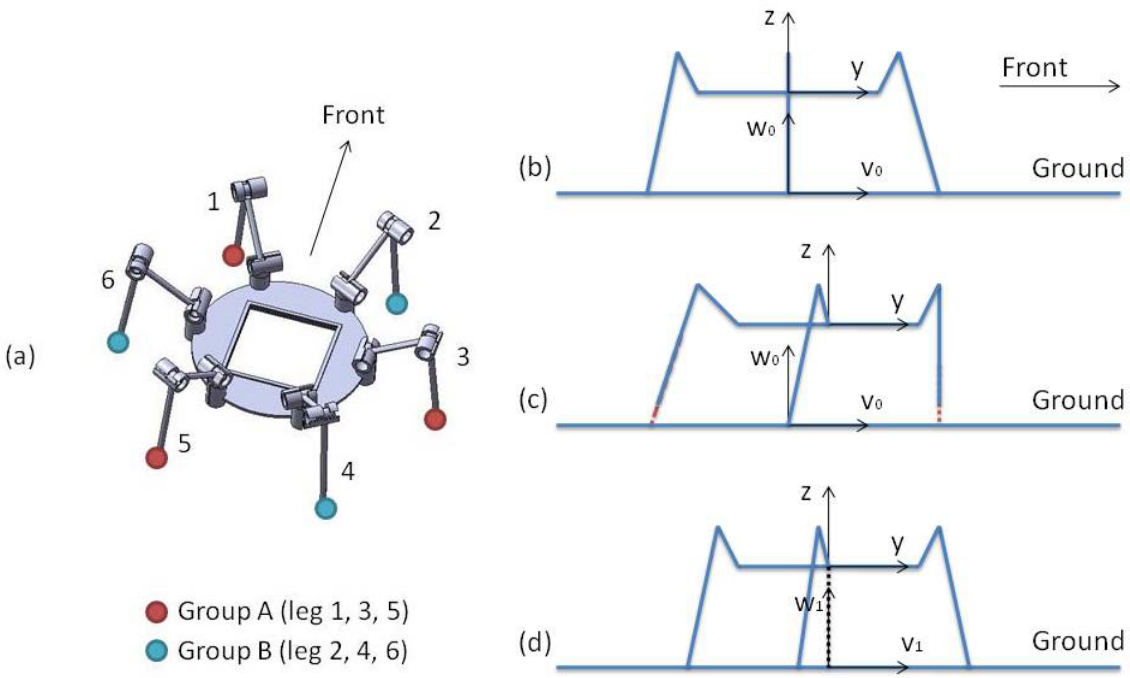

Figure 2-9: Local ground coordinate example: (a) Leg grouping in tripod gait. (b)-(d) Side view interpretation for one cycle of changing the local ground coordinate (consider only group A in this step).

2.6 Chapter conclusion

In this chapter, the basic configuration of the robot was proposed. A kinematic analysis was, thereafter, performed by considering two configurations for the position of the leg's joints. By applying direct kinematic equations for each leg, the position of the feet was mapped and used for calculating the robot position with respect to the ground coordinate. By utilizing inverse kinematic equations, it is possible to plan the motion of the robot to walk, climb and cope with obstacles. In the following chapter, these equations are used to generate position data for the robot walking in a pentapedal gait.

CHAPTER 3 MECHANICAL AND MECHATRONIC DESIGN

Based on the analysis presented in Chapter 2, two prototypes were developed by considering the two configurations of the position of the leg's joints, which affect the thickness of the robot's body. A smaller body thickness is assumed to be better because the center of mass (COM) of the robot's body, which houses most of the electronics and has most of the robot weight, can be placed closer to the contacting wall. With the COM closer to the wall, the torque generated by body weight with respect to the adhesive feet is reduced, avoiding twisting on the synthetic dry adhesive, which can cause adhesion failure. On the other side, the configuration 1, in which the shoulder and the elbow joints are yields a more compact robot.

In this chapter, the mechatronic design of two prototypes, respectively having configuration 1 and 2, are introduced. Discussion about their performance is given in Chapter 4.

3.1 Manufacturing of robot construction part

A rapid prototyping machine, InVision^{TM} HR Si^2 3-D Printer, was used in all the prototype manufacturing. Parts were designed in SolidWorks and sent to the printer for fabrication. The machine allows new prototype fabrication within one day and achieves relatively good accuracy, which is important for a miniaturized robot. From a test of gap printing, the minimum clearance the

machine achieves is 0.25 mm. The disadvantage of this machine is the part material, VisiJet® SR-200, is made from triethylene glycol dimethacrylate ester and urethane acrylate polymer, which is brittle and can be easily broken by applying large forces. The material properties require that the mechanical design should avoid large forces acting on the weak parts. Specification of the part material is given in [49].

3.2 Prototype 1: hexapod using servo motor electronics

3.2.1 Mechatronic system analysis

Prototype 1 was designed according to configuration 1, which confers the prototype a smaller body thickness (Figure 3-1). To control a robot walking as planned, a position control was implemented, using a position sensor, an actuator, and a controller. Towards this objective, a servo motor was used, as it contains all these components.

Some parts from the servo motors, Hitec HS-311, were used in this first prototype (Appendix B). A typical servo motor contains a gearbox, a DC motor, a potentiometer, and a preprogrammed Printed Circuit Board (PCB), which form the closed loop control of a joint (Figure 3-2). The preprogrammed PCB consists of the electronics for controlling the position of the servo motor. From the servo controller, the position signal (in angles) is sent to the preprogrammed PCB to run the motor until the potentiometer reaches the set point value. Three wires attach to the servo motor: a signal line and two power lines. The signal line is

receiving signals in pulses, while the power lines provide power to the motor in a constant voltage level.

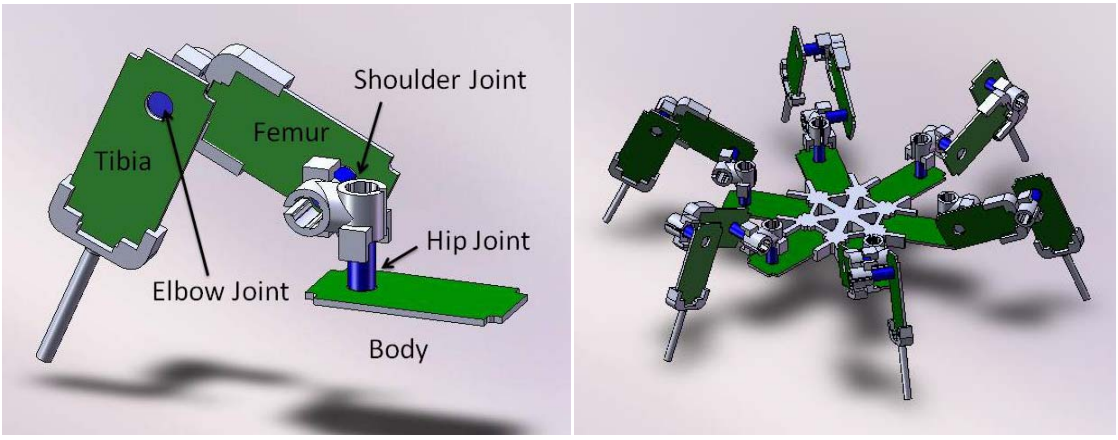

(a) **(b)**

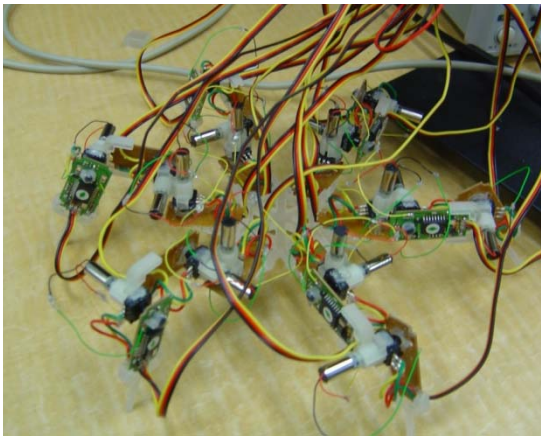

(c)

Figure 3-1: Design of Prototype 1. (a) CAD model of one leg in Prototype 1. (b) CAD model of Prototype 1. Blue part represents the motor, green part denotes the preprogrammed PCB and grey part is the robot construction part manufactured by the 3D printer. (c) Prototype 1 without servo controller.

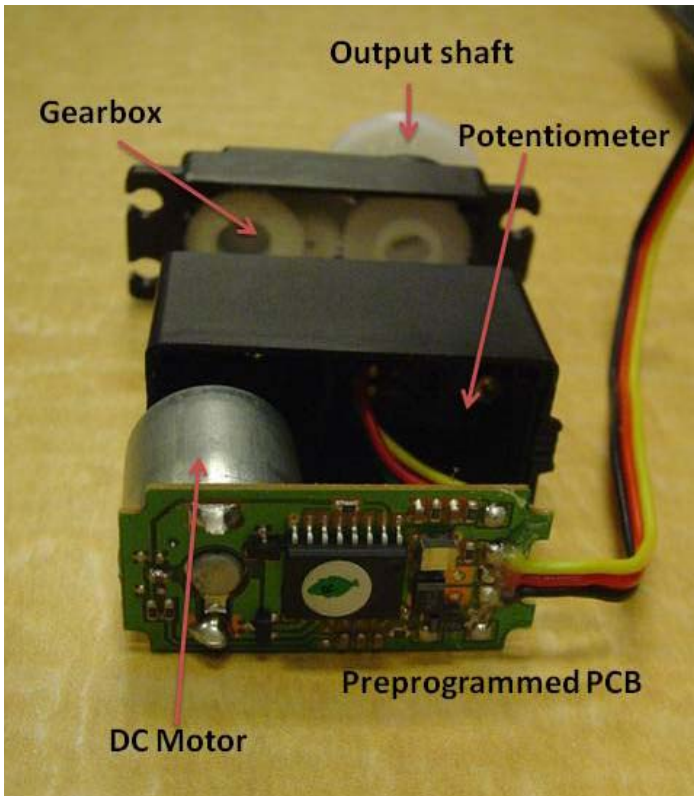

Figure 3-2: Original structure of HS-311 Servo motor.

By using the servo motor, we do not need to gather all the position feedback and set point signals in the main processor, which saves a lot of wiring and control calculations. It is possible to connect all the power lines in each joint and wire them to a single power source afterwards. Therefore, from the robot to the servo controller, only 18 signal lines plus 2 power lines are needed. Figure 3-3 illustrates the data flow of control signals in Prototype 1. Each preprogrammed PCB runs its own control loop to achieve a desired angle and only accepts

position signals from the servo controller. Position signals are stored in the computer and sent to the servo controller by controlling software.

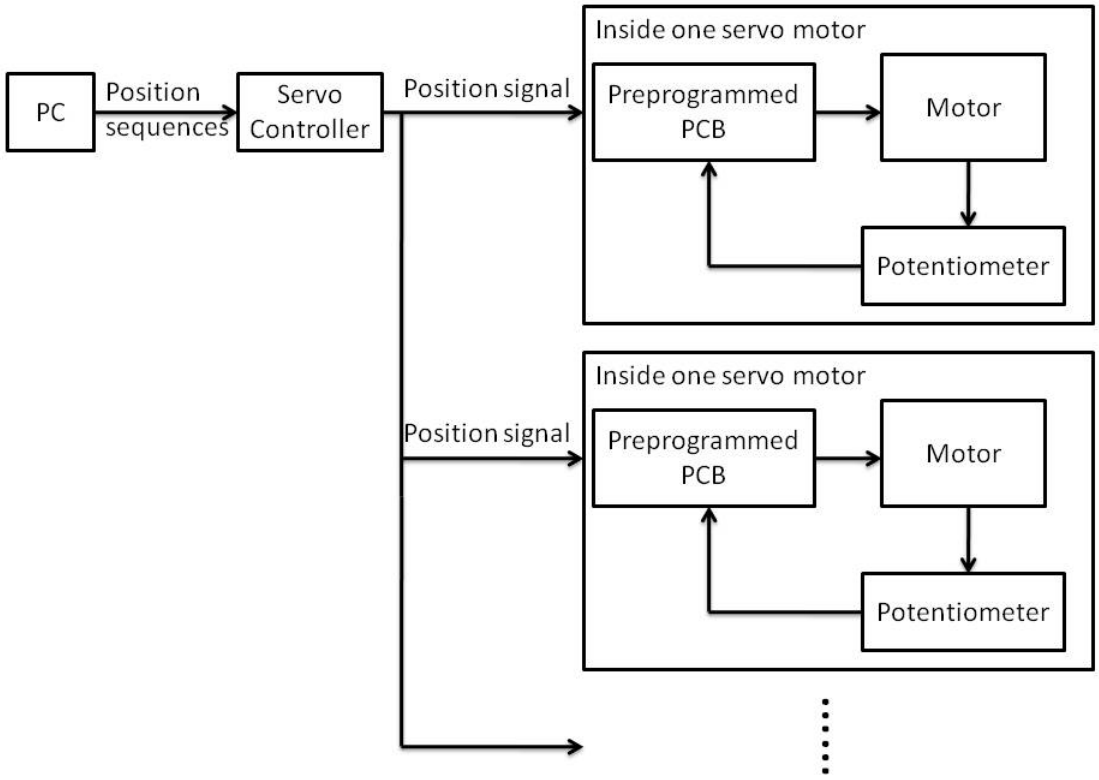

Figure 3-3: Data flow of Prototype 1.

3.2.2 Mechanical structure of modified servo joint

In order to take advantage of the servo motor's electronics while still maintaining the miniature feature of the robot, a 6 mm DC motor attached with a mini gearbox from Gizmo's Zone (GH6124S, Appendix C) replaced the original gear box and motor. The gear ratio of the attached gearbox is 1:699.55. Figure 3-1 (a) and (b) shows the CAD model of a leg and the robot prototype; (c) shows the final prototype without the servo controller board. The potentiometer constituted the joint and the PCB was integrated as part of the leg stem. Figure

3-4 demonstrates the assembly of one joint in Prototype 1. The potentiometer has a hole at the back of the wiper (Figure 3-4 (a)). The motor shaft has a similar size, which allows the shaft to be plugged in and be fixed to the wiper (Figure 3-4 (b)). The extruded part from the potentiometer, which is also the wiper, is connected to the PCB of the next link. The motor body is connected to the outer box of the potentiometer, and also to the previous link (Figure 3-4 (c) (d)). This unique configuration decreases the robot's weight and unnecessary friction compared to a joint constructed with extra parts.

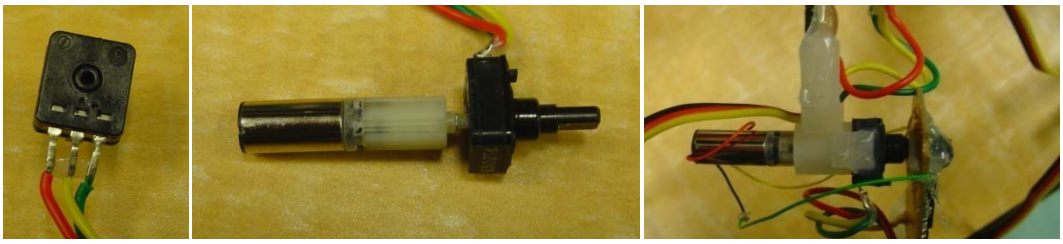

(a) (b) (c)

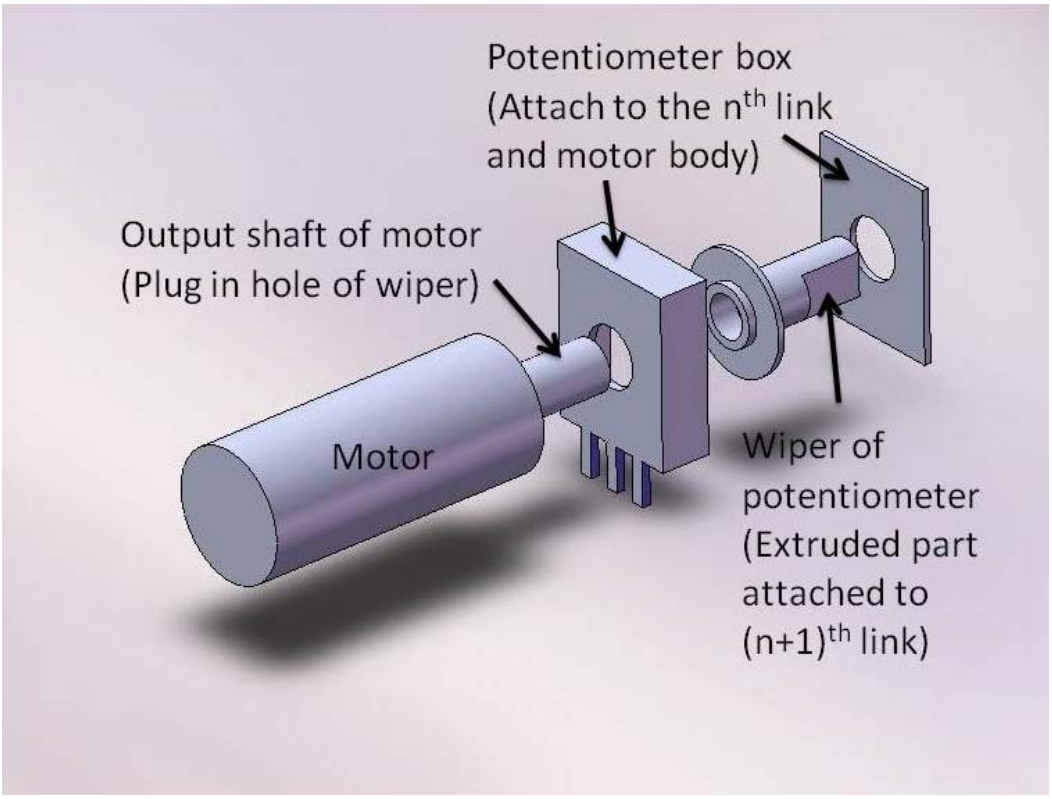

(d)

Figure 3-4: Assembly of one joint in Prototype 1. (a) Back of the potentiometer. (b) Motor shaft plugged in the rotor of the potentiometer. White part is the gearbox. (c) A joint assembly on Prototype 1. (d) Assembly structure of one joint.

3.2.3 Electronics features and adaption to the robot

A servo control board SSC-32 [44] with the software Visual Sequencer [45] from Lynxmotion Inc. was used to send the sequence of position signals to the servos. SSC-32 is able to communicate with the computer using an RS232 cable or wireless connection, such as a Bluetooth modem. Figure 3-5 (a) shows the SSC-32, a Bluetooth modem, BlueSMiRF WRL-00582 [47], from Sparkfun Electronics, and the batteries for powering the system. SSC-32 can control a maximum of 32 servos, which provids an option for adding more motors in the future. The robot configuration requires different voltage inputs for the board and the motors. The mini motor, GH6124S, has a recommended voltage of no higher than 3V. The power supply to the electronic board is 9V according to the datasheet. A lightweight Lithium Polymer Battery provides 3V to the servo motors, while the power supply for the electronic board is from a rechargeable 9V battery. The board has four analog channels for extended sensor or wireless connection. Two of the channels are currently occupied by the Bluetooth modem. The software, Visual Sequencer (Figure 3-5 (b)), is able to read the position sequence in a look-up table stored in the computer. It then sends the signals to the SSC-32 in real time. Proper software modification might enable the software to have real time feedback from the robot, which will allow for further control to cope with different situations, such as transferring from surfaces and avoiding obstacles.

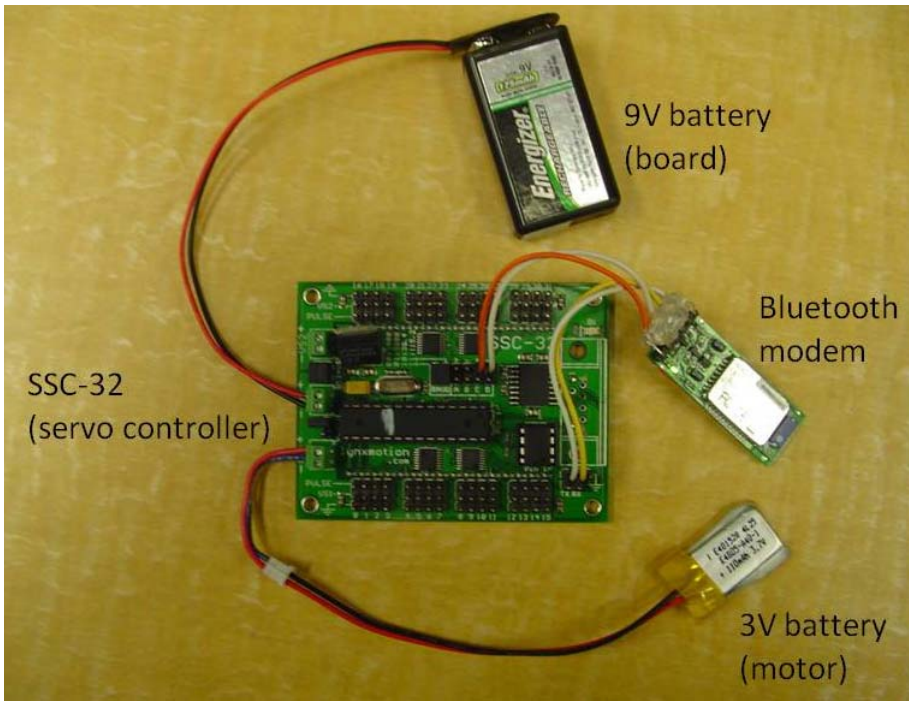

(a)

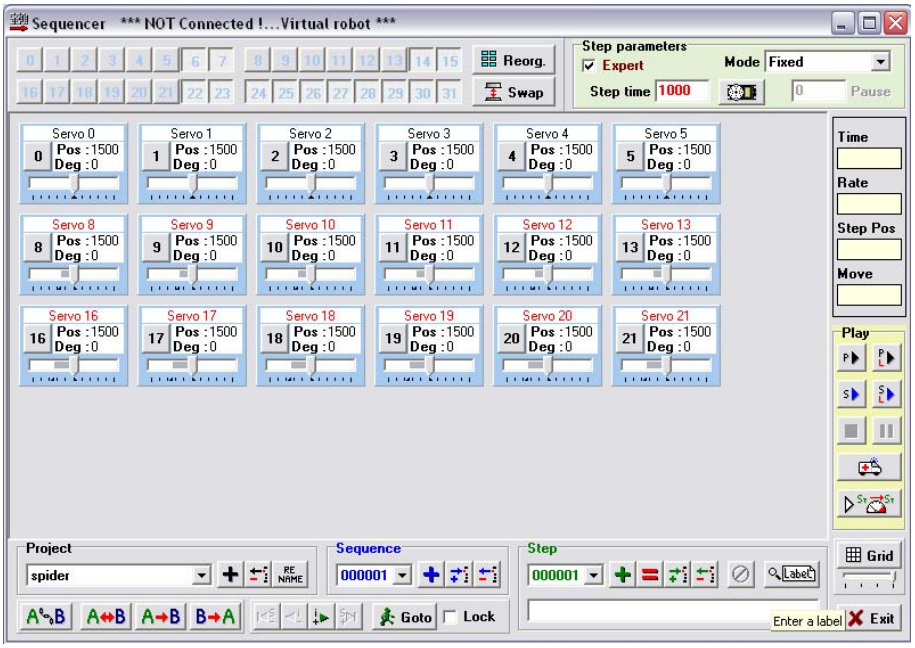

(b)

Figure 3-5: (a) SSC-32, batteries for servo controller and servo motors, and the Bluetooth modem. (b) User interface of Visual Sequencer.

3.2.4 Robot performance

Prototype 1 was able to synchronize all 18 joints to follow the position sequences in order to achieve the designed movements. The total robot weight was around 260 grams, including all the batteries, electronics and communication parts. The length of the robot body was 90 mm and leg length was 100 mm. Maximum output torque from each joint is 2×10^{-2} N·m by using a 3V power supply which powers the motors. The robot was able to walk straight and turn with different gaits on horizontal surfaces, and it was also able to climb on smooth surfaces up to 90 degrees (i.e., vertical wall) with adhesives attached.

Several issues observed during the tests, should be addressed: (1) due to clearances among gears in the motor gearbox, the joint have approximately three to five degrees of error. Both the gears and the motor shaft are fabricated with Glass Fiber Reinforced Engineering Plastic; with increasing load, especially when the robot climbs and uses adhesives, the clearance increases and eventually strips the teeth of the gears, sometimes even breaking the motor shaft. No substitute product has been found to date. (2) A lack of documentation about the preprogrammed PCB from the servo motor resulted in difficulties in accurately positioning the motor. From our observations, the controller on the PCB might be a simple Proportional-Integral-Derivative (PID) controller which has parameters that are not specified in the datasheet. The PIC manufactured by Hitec has no part numbers, and the controller parameters are neither accessible nor changeable. A digital servo, HS-5475HB, from Hitec, which is programmable by a digital servo programmer (Hitec HFP-20), was also tested with different

dead-band widths. No distinct enhancement of accuracy was observed in comparison to the analog servo HS-311. (3) The movement of the robot was not very smooth, especially when the leg is in its swing phase. This problem is not major, but it might be one of the reasons causing unstable movement. (4) The large number of wires from the servo-motors accounts for more than 20% of the robot weight. By examining the weight of one joint, the signal and power wires are 3.1 g and all other parts including the PCB, motor, and potentiometer weight, only weigh 5.0 g. A solution to this problem was found by substituting the existing thick wires with thin silver wires (0.0762 mm bare Teflon coated silver wire from A-M Systems); the modified servo motor in fact performed as good as the original one with respect to both reaction speed and output torque.

3.3 Prototype 2: hexapod with motor driven joints

Prototype 2 was designed to have fully customized electronics and mechanical structure (Figure 3-6). The prototype was designed using configuration 2 in the kinematic analysis. Compared to Prototype 1, this prototype was designed with all parts specifically selected, resulting in a more compact structure. The weight of Prototype 2 was around 130 g without a battery, nearly half of the mass of Prototype 1 which was 260 g. Electronic boards were stacked in three layers in the middle of the robot body. In this prototype, the joint was fabricated from the 3D printer material, instead of using the rotation mechanism of the potentiometer as in Prototype 1. Magneto-sensitive sensors were used as position feedback and placed beside the joints without touching the motor. Actuators and sensors located at the joint formed a compact and clean structure

for the robot. At the end of the leg, a connector was designed to attach the adhesives. The connectors are replaceable, allowing the robot feet to have different contact angles and to have different adhesive samples attached.

Compared to Prototype 1, the axes of the hip joint and the shoulder joint intersect as configuration 2 introduced in Chapter 2. Hence, the robot body is a little thicker than Prototype 1, regardless the stacked electronic parts. This configuration, however, allows for increased compactness and reduces the robot's weight.

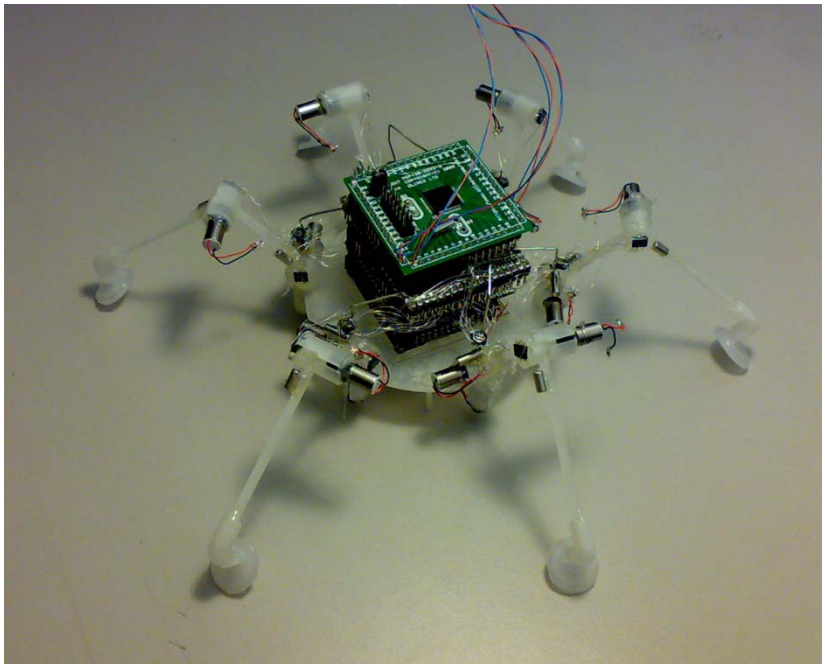

Figure 3-6: Second prototype with electronics, connectors and feet [34].

3.3.1 Mechatronic system analysis

Prototype 2 used the mini motor, GM15, from Solarbotics, a position sensor, HMC1512, from Honeywell, and several other electronic parts to achieve position control of each joint. Two options on controller construction exist at the

beginning of electronic design: an onboard micro controller or an off-line computer transferring signals via wireless connection to the onboard electronics. This thesis will only discusses the off-line computer controller designed using LabVIEW from National Instruments (NI).

The position sensor HMC1512 (see Figure 3-7 (a)) was selected because it is frictionless compared to a typical position sensor such as potentiometers. The size of the chip is 5 mm $\times$ 5 mm $\times$1 mm and each weighs 5 g. The resolution of the sensor is approximately 0.05 degree [39]. It has 8 pins: 4 power pins and 4 signal pins from 2 Wheatstone Bridges. Differentiations of the 4 signal outputs form the 2 signals from each bridge, which are used in angular position calculations. GM15 (see Figure 3-7 (b)) was chosen because of its miniaturized features (6 mm diameter) and because it includes a gearbox (gear ratio 1:25, Appendix D). The H-bridge chip SN754410 is one of the most common PICs used for controlling small robots. This chip can control two motors rotating clockwise (CW) or counter-clockwise (CCW) at the same time. According to the datasheet, the chip requires only 1 input line for each motor with the simple circuit with a converter. The input signal to the motors and output signal from the sensors are analyzed by using a Data Acquisition Card (DAQ) USB-6259 - a simple PID controller was designed and tested in LabVIEW 8.2. Joint design is shown in Figure 3-7 (c).

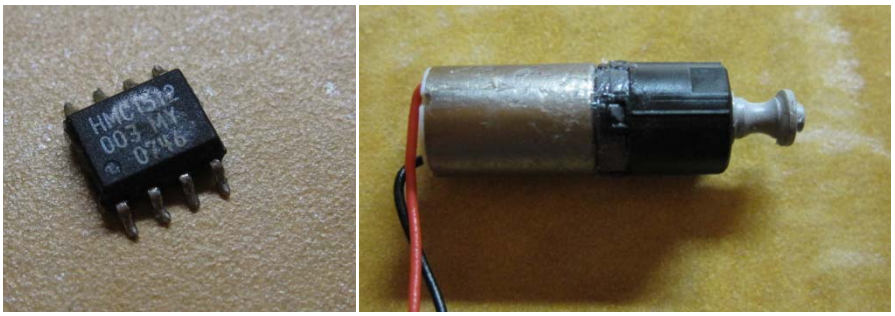

(a) **(b)**

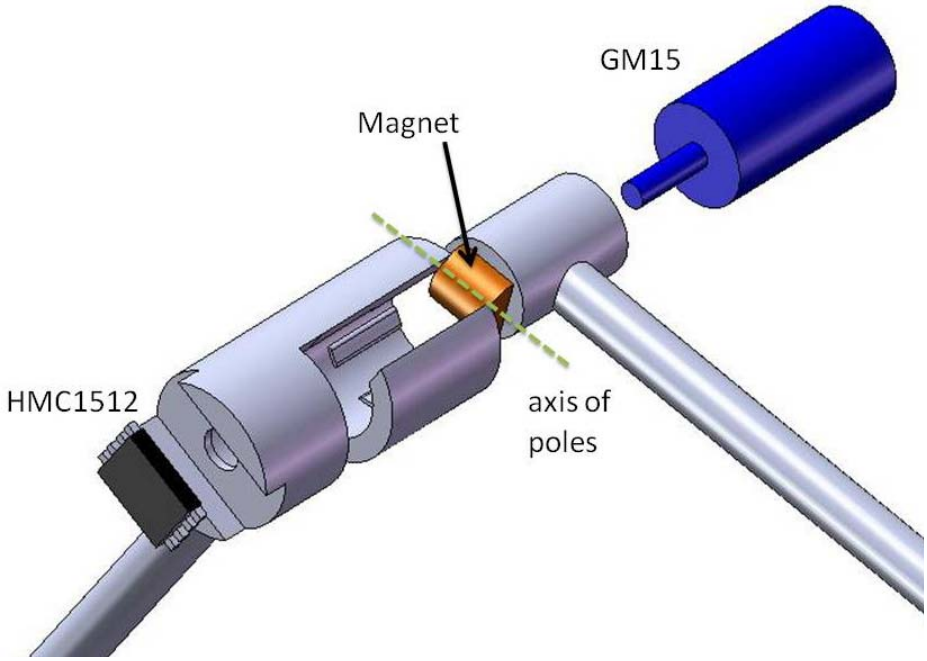

(c)

Figure 3-7: Construction of one joint in Prototype 2. (a) HMC1512 rotary position sensor. (b) GM15 mini gear motor. (c) CAD Scheme of joint construction.

3.3.2 Motor control signal

A digital signal controlled with pulse width modulation (PWM) was used to control the motor. As its name expresses, PWM is a pulsed signal in which the

percentage of the high voltage (5V) in one period, which is called duty cycle, decides the information in the signal. PWM can also be thought as an average voltage level, as in an analog signal. To apply PWM to the DC motor, an H-bridge and converter circuit is usually added between the signal source and the motor. By applying a 50% duty cycle, the motor receives an 'average voltage' of 0V, while a 100% and 0% duty cycle will run the motor in full speed rotating CW and CCW, respectively. This method solves the problem of the dead-band caused by the excitation voltage of the motor in the case of an analog signal. The pulse rotates the motor in two directions with a certain frequency, which decreases the heat otherwise caused when an analog signal is used in holding high torque. Test results showed that the minimum frequency of PWM that should be applied to the circuit is 50 Hz. Frequencies lower than 50 Hz will cause the motor to oscillate. Usually a 500 Hz PWM is applied to the circuit for smooth movement.

3.3.3 Sensor selection and tests

For position feedback, the potentiometer is one of the most common angular sensor used in miniaturized robots. It has the advantage of being lightweight, having a simple signal output (one line analog signal), and it is available in a large variety of different shapes and resistances. One main disadvantage of potentiometers is the friction inside the sensor. While the wiper and the fixed part have good contact, the friction between them is usually high, and this characteristic is not desirable in a power conserving robot. If the friction is low, the wiper and fixed part will have weak contact, which causes an

inconsistent output voltage. We conducted a simple test using a low friction potentiometer, Murata SV01L, in one joint. The set point and sensor response was generated and recorded by a Data Acquisition Card (DAQ) USB-6259 and LabView 8.2 both from NI. Control of the test system was simply obtained by using a proportional controller. The chart in Figure 3-8 demonstrates the desired angles (blue line) and measured experimental angle (red line). The offset between set point and process variable was deemed to be caused by clearances of the low friction potentiometer. In order to avoid friction and an inconsistent sensor signal, the magneto-sensitive rotary sensor HMC1512 was tested and integrated in one leg position experiment.

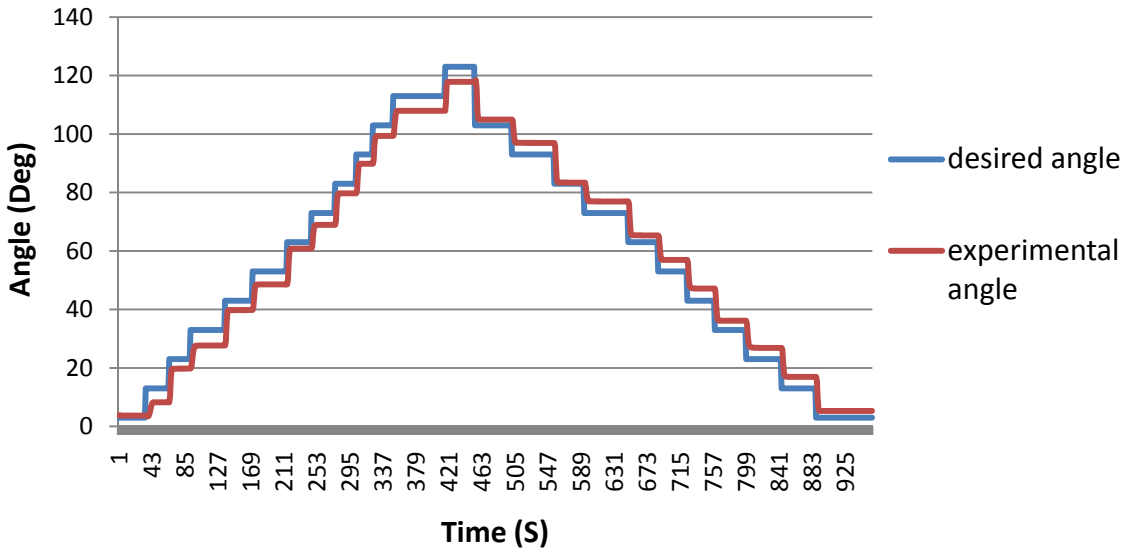

Figure 3-8: Potentiometer test result.

The HMC1512 is able to sense a maximum of 180 degrees of rotating displacement. The magnet should be placed on a parallel plane to the sensor

and, therefore, it was embedded inside the joint underneath the sensor as Figure 3-9 shows. Four magneto-sensitive resistors are placed as a Wheatstone bridge in the sensor. The anisotropic magnetoresistance causes the resistance change in the sensor. According to the datasheet, two magnetoresistance parts have a 45 degrees offset which causes the output of the two bridge to also have 45 degrees of offset. Instead of using the equation provided by the manufacturer (see Appendix E), another set of substitute equations (equation 3-1, 3-2) were deduced and used to calculate the output angles. Tests were performed to validate those equations. A magnet was rotated with constant velocity in the elbow joint and the maximum angle of rotation was 135 degrees. The output voltage is charted in Figure 3-10. According to the voltage-angle relationship in this chart, the equations used in converting output voltage to the joint angle are:

$$If\ V_B > V_{ob}, \theta = \frac{1}{2} arccos \frac{V_A - V_{oa}}{V_{Amax} - V_{Amin}} \tag{3-1}$$

$$If\ V_B < V_{ob}, \theta = -\frac{1}{2} arccos \frac{V_A - V_{oa}}{V_{Amax} - V_{Amin}} \tag{3-2}$$

where $V_{ob} = \big||V_{Bmax}| - |V_{Bmin}|\big|$, $V_{oa} = \big||V_{Amax}| - |V_{Amin}|\big|$. Notations of V_A and V_B, indicate the output voltage of Bridge A and Bridge B.

In equations (3-1) and (3-2), the 0 degree position is not the end position of the moving joint. Therefore, to implement the equations into each joint, the angle θ should be subtracted by a certain angle to correspond with the kinematic configuration.

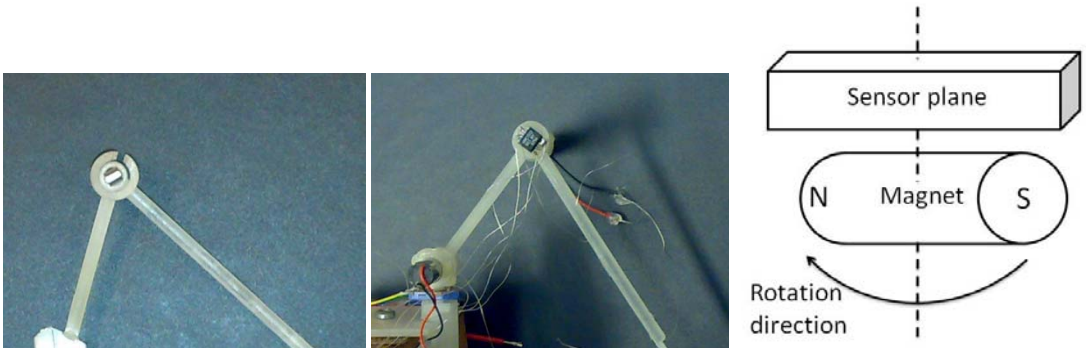

(a) **(b)** **(c)**

Figure 3-9: Application process of magneto-sensitive sensor. (a) Magnet positioned inside a joint, glued to the smaller circle which is the rotor. (b) Sensor place on top of the magnet, glued to the bigger circle which is the stator. (c) Graph showing the working principle of the sensor.

Several angles (15, 30, 45, 60 degrees) were tested with the same controller as the potentiometer test. A protractor was attached to the joint to inspect the rotational displacement. All angles reached the target. The minimum observable displacement was 0.5 degree. The problem with attaching the sensor onto the robot is that the hip and shoulder joints are so close that the two sensors and magnets interfere with each other if the same sensor and the same arrangement is applied to the two joints. To avoid this situation, the sensor and magnet of the hip joint need to be reconfigured in a different place. Alternatively, one of the joints could utilize a different type of sensor, e.g., a potentiometer with proper friction or a rotary encoder.

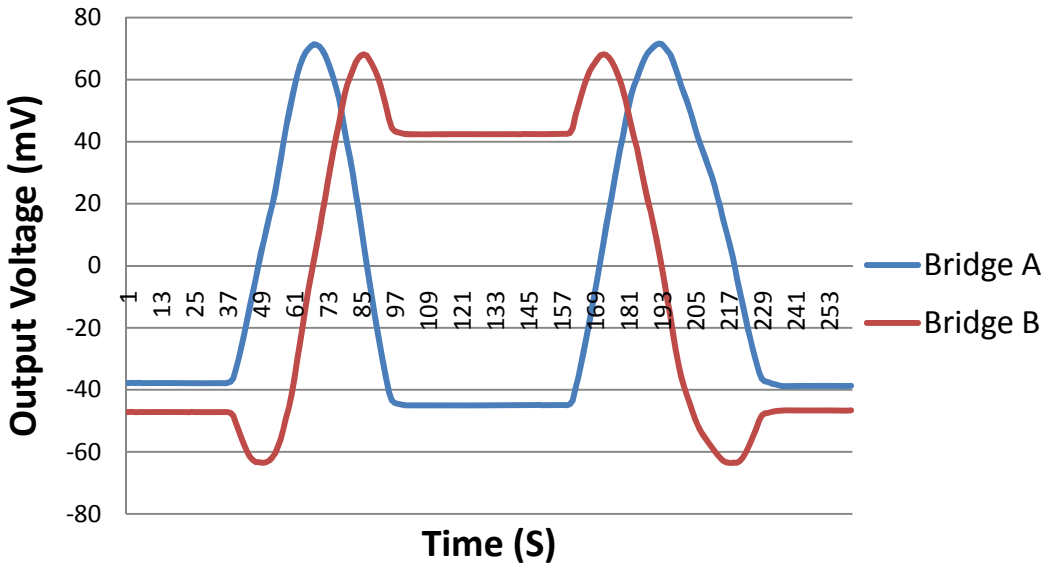

Figure 3-10: Magneto-sensitive sensor test result. The magnet was rotating 135 degrees with constant velocity.

Compared to the potentiometer, four lines of signal output from each sensor complicate the wiring and displacement calculation. Though the four lines could be differentiated before connecting to the processor, each sensor will have two signals, which results in a total of 36 wires from the sensors to the processor for the entire robot. The two signals need to be calculated with the set of equations to convert into angular position. For these reasons, and despite the difficulties encountered while trying to embed all joints with the HMC1512 rotary sensor, implements the magneto-sensitive sensor into the robot is a feasible solution.

3.3.4 Controller design and other electronics

A PID controller was built in LabVIEW after we decided on the final actuators and sensors (Figure 3-11). The DAQ USB-6259 receives and transfers signals between the hardware, which are the sensor and motor, and the PC, where the controller, implemented in LabVIEW, is running. In each joint, the DAQ sends a one-line PWM signal to the converter with a set duty cycle and frequency. Afterwards, the converter outputs two lines of signals to the H-bridge, one of them is the same as the original PWM and the other is reversed. The H-bridge links the two poles of the motor, driving it to rotate with desired speed and direction.

The sensor outputs four signals from two bridges, which are differentiated in the DAQ to provide two output signals to the controller. The two signals are converted into angular position with the equations (3-1) and (3-2) in the LabVIEW controller. The DAQ is connected to the PC by a USB port. The scheme of the control loop is shown in Figure 3-12. Validation is given in a test of one leg position control, which is going to be described in Chapter 4. Unfortunately, current DAQ manufactured by NI could only generate PWM in maximum of eight individual digital channels. Prototype 2, however, requires 18 signals for controlling all the motors. If LabVIEW and the DAQ are used to control the entire system, additional electronics, such as a multiplexer and Field-Programmable Gate Array (FPGA), should be added in a proper circuit to arrange the high number of input and output wires.

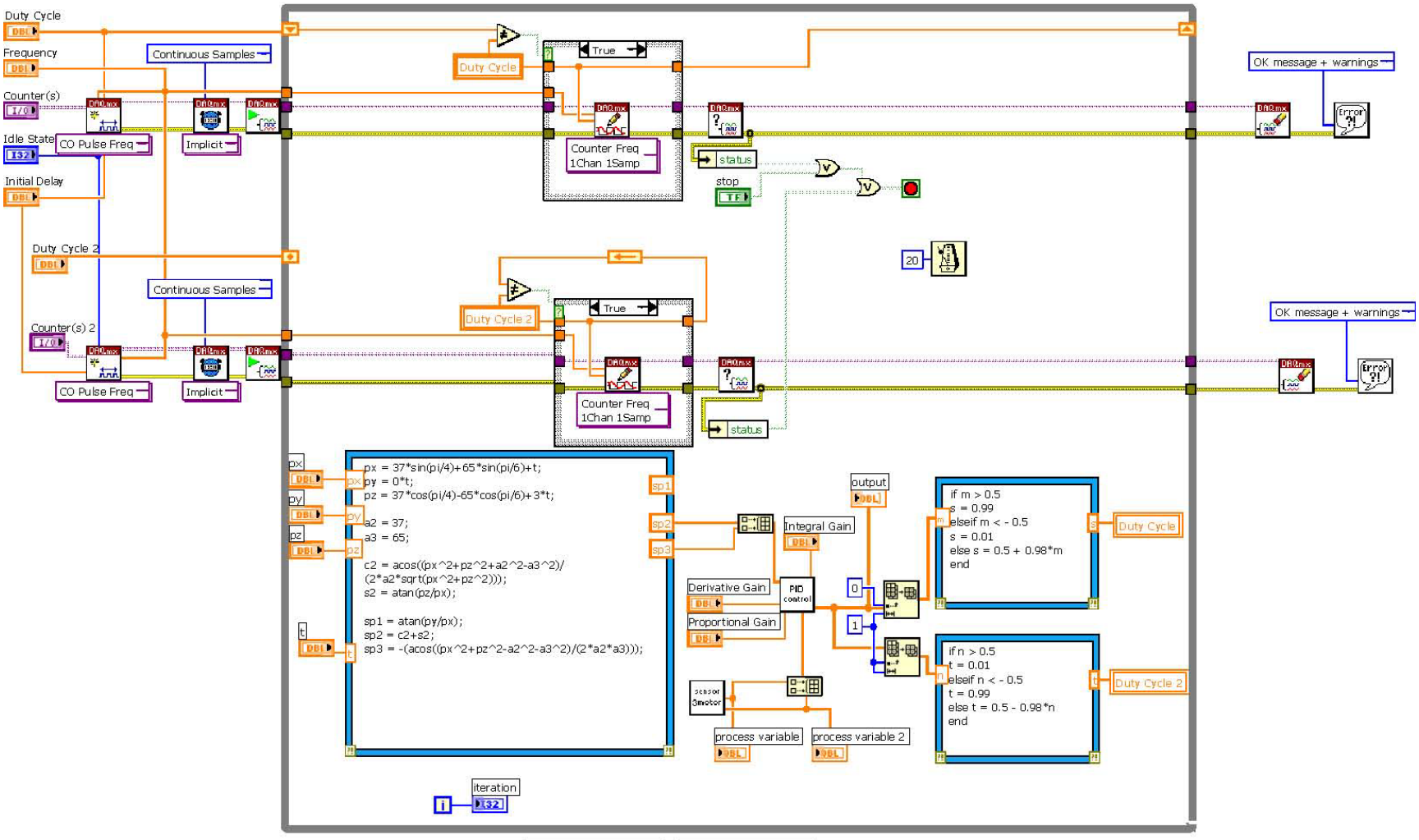

Figure 3-11: Block diagram of controller design in LabVIEW 8.2.

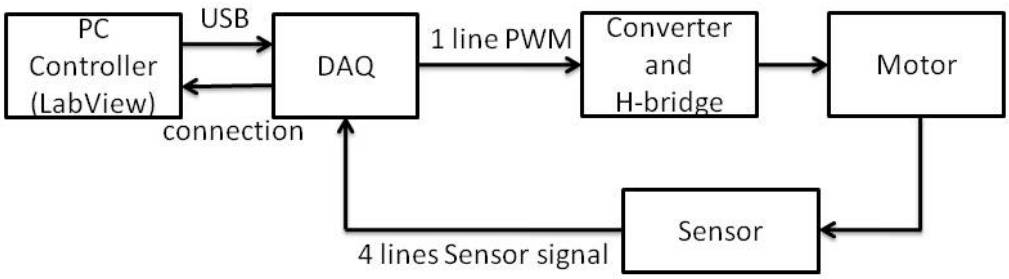

Figure 3-12: Control loop in one joint of Prototype 2.

3.4 Discussion and conclusion

Prototype 1 showed the ability of climbing an inclined surface. Pentapedal gait, the gait of moving one leg per time, was tested and is discussed in Chapter 4. The use of commercial parts, such as the PCB from servos and servo controller with proper software, is a convenient way to control the climbing robot in position. However, compared to Prototype 2, the predesigned electronics has several disadvantages, which confines the size and function of the robot. On the other hand, Prototype 2 had all customized electronics components which allowed for the most compact design. Although controlling the position of all motors was not possible, Prototype 2 showed the flexibility of the electronics system design and the potential to have accurate movements. The design of a reliable electronic system of Prototype 2 represents a long-term goal to be performed as further research. Thus design is beyond scope of this thesis. A comparison about the two prototypes is given in Table 3-1.

Table 3-1: Comparison of Prototype 1 and 2.

	Weight	Size	Sensor	Motor	Controller
Prototype 1	260 g (batteries included)	90 mm body diameter, 100 mm full leg length	Potentiometer (from servo motor HS-311)	6 mm gear-motor GH6124S (1:700)	Servo controller SSC-32, Servo motor PCB, PC Software
Prototype 2	131 g (batteries not included)	90 mm body diameter, 102 mm full leg length	Magneto-sensitive sensor (HMC1512)	6 mm gear-motor GM15 (1:25)	H-bridge, customized LabVIEW controller

In this chapter, the feasibility of the preliminary system design of a hexapod climbing robot was demonstrated in both mechanical and mechatronic aspects. Features of each prototype were discussed and compared. Prototype 1 has the highest potential to be developed in a short period, while Prototype 2 has more potential in the long-term.

CHAPTER 4 KINEMATIC VALIDATION AND DEVELOPMENT OF CONTROL STRATEGIES

The first three sections of this chapter present the kinematic validation of the equations proposed in Chapter 2. The remaining sections of this chapter present a preliminary development of control strategies to be used in maneuvering with synthetic dry adhesives integrated on the feet of the robot.

4.1 Serial manipulator kinematics

4.1.1 MATLAB simulation

The inverse kinematic equations for a serial manipulator introduced in Chapter 2 were used in MATLAB to generate joint variables for the designated end-effector trajectories. Figure 4-1 (a) schematically represents the simulated configuration. The geometry of the leg is based on Prototype 2. The origin of the leg platform is located in the geometric center of the shoulder joint. The initial position of the hip joint is 0 degrees, the shoulder joint is 45 degrees, and the elbow joint is -105 degrees. The end effector has an angle of 30 degrees with respect to the ground plane. Figure 4-1 (b-d), therefore, shows the validation results of the inverse kinematic and direct kinematic equations. An example of a defined trajectory is shown in Figure 4-1 (c) as the time history of the end effector coordinates. The trajectory is a function of time, which lasts for 30 seconds while moving at a speed of $\sqrt{2}$ mm/s. Figure 4-1 (b) shows the time history of each

joint while the end effector was moving as Figure 4-1 (c) defines; joint rotation angles were generated by utilizing inverse kinematic equations (2-11) - (2-14). Figure 4-1 (d) shows the time history of the end effector coordinates generated by direct kinematic equation (2) – (5) using the result of the joint variables generated in the inverse kinematics shown in Figure 4-1 (b). Figure (c) and (d) are identical, which means the direct kinematic and inverse kinematic equations are consistent with each other, proving the equations are correct and ready for application.

For a fixed end-effector position, only one set of joint variables achieves the goal in a continuous trajectory. In other words, the orientation of the end effector in a designated position is fixed, which means that, if we need to control the end tip of the leg in both position and orientation, the current design will not be sufficient. As the direction of the leg tip does not really matter while it is in the swing phase, the main concern of the leg tip direction is the approaching and detaching angle for controlling the properties of the synthetic dry adhesion. Another degree of freedom, or an extra joint, needs to be added for controlling the feet direction.

In the most recent foot design, the extra joint was designed to be passive and was fabricated using Polydimethylsiloxane (PDMS) as an ankle (Figure 4-2 (a)). As the material is soft, it allows the end tip of the leg to have three more degrees of freedom, allowing for rotation in all directions when the feet are attached to a surface. The three extra passive DOFs are modeled as a spherical joint in Chapter 2. Another potential design of the passive joint is the dual layer

foot (Figure 4-2 (b)), which may be used in future designs. The dual layers include the upper layer, which consists of spaced macro pillars attached to a one-piece PDMS foot, and the lower layer, which is fabricated out of micro adhesive pads attached to each pillar of the upper layer. This design is more compliant to the contacting surface due to its multi-scale structure.

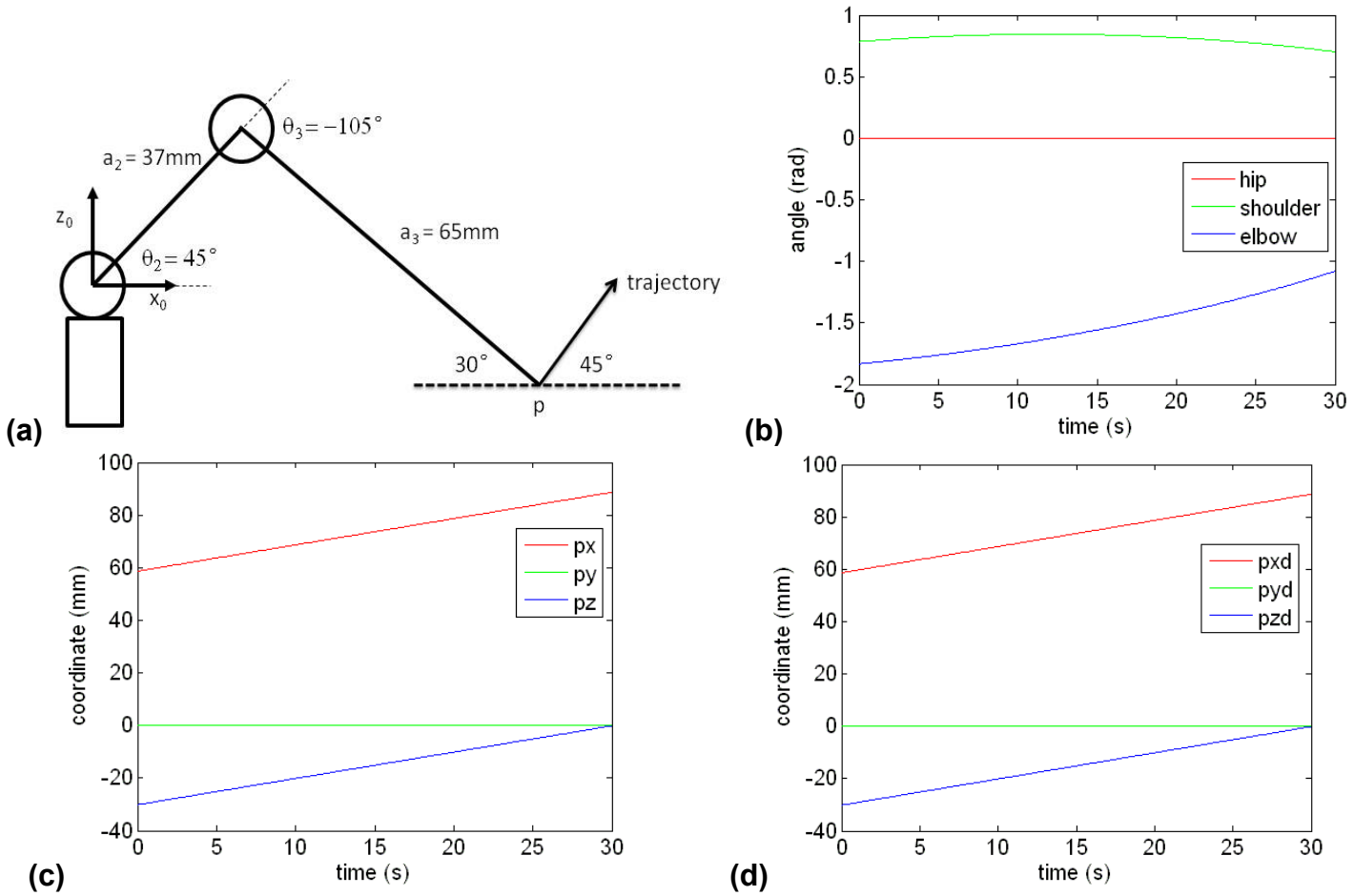

Figure 4-1: Single leg kinematic validation. (a) Assignment of initial position and parameters. (b) Time history of joint variables while end-effector is moving 45 degrees straight outward. (c) Time history of end effector coordinates assigned in inverse kinematic simulation. (d) Time history of end effector coordinates as output generated by direct kinematic equations.

(a) (b)

Figure 4-2: Ankle on a foot fabricated using PDMS (a) and a dual-layer foot (b).

4.1.2 Position control test based on Prototype 2

In order to test the PID controller designed in LabVIEW and to validate the one leg open chain kinematics, a position control test based on Prototype 2 was performed with the setup as shown in Figure 4-3. Wires at the back were linked to the DAQ PCI-6071E. The motor signals were provided by the digital ports in PWM and the sensor signals were feedback into DAQ's analog channels. As Chapter 3 described, PID control is provided by LabVIEW. A MATLAB script was written in a node in the controller. By using MATLAB results, three motors were given the data and the end-effector was monitored to verify if it achieved the expected trajectory, which was a 45 degree straight line outward. To avoid overshoot, the joints were moved in very small steps at a relatively slow speed ($\sqrt{2}$ mm/s). Measuring with a protractor, the end effector was observed to follow the predefined trajectory.

Test results of the control loop are shown in Figure 4-4. The set point denotes the data generated by MATLAB simulation and sensor 2 and sensor 3 denote the sensor feedback signals in the shoulder and elbow joints,

respectively. Because the hip joint does not move in this trajectory, the data for the first joint are not shown in the test results. The results highlight that the elbow joint was more accurate than the shoulder joint because the shoulder joint experienced a heavier load than the elbow joint through the movement. The load on the elbow joint was only due to the mass of the last link of the mechanism, while the load of the shoulder joint was from the last two links plus the motor in the elbow. The two joints used the same set of parameters since the controller design did not separate the parameter setting. Different controller parameters might need to be assigned to the shoulder joint for improved accuracy.

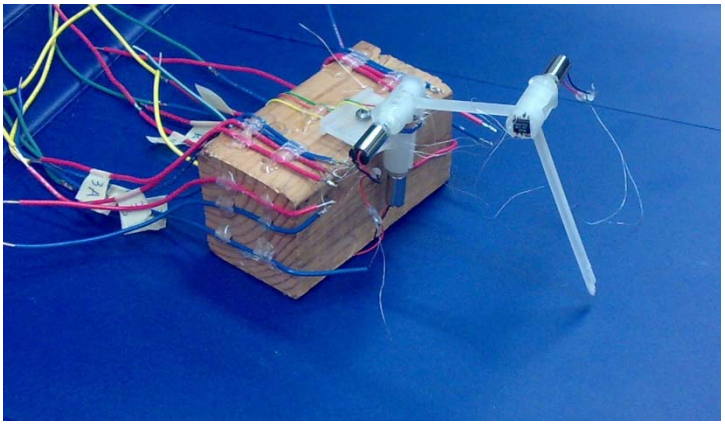

Figure 4-3: Test configuration of the single leg position control.

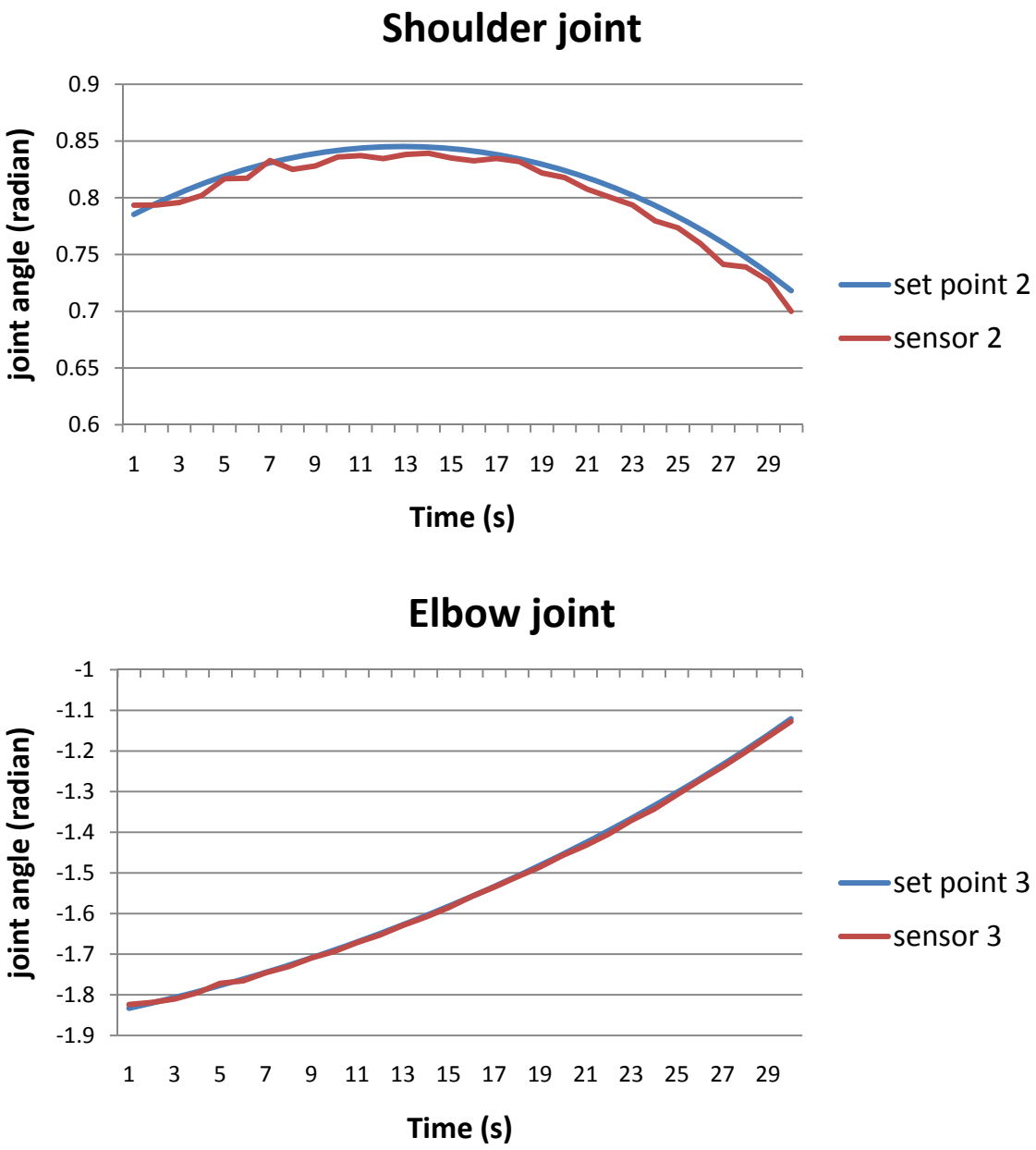

Figure 4-4: Controller test result of the shoulder joint (sensor 2) and elbow joint (sensor 3).

4.2 Parallel manipulator kinematics

4.2.1 Data generated in MATLAB

The inverse kinematic equations discussed in Chapter 2 were used in generating data for the robot platform movement using MATLAB. The geometry of the robot was taken from Prototype 1. The robot platform was designed to move forward 10 mm at a speed of 1 mm/s. All legs were assumed to contact to the ground through the moving process. The initial angles of all the legs were identical: hip joints at 0 degrees, shoulder joints at 30 degrees and elbow joints at -90 degrees. In order to obtain the elbow joint data directly applicable to the test platform, the sign of the elbow joint data was reversed (i.e., value become positive). Figure 4-7 shows the plot of the joint variables for the front, middle, and rear legs. Because the legs of the robot were arranged symmetrical in a circle, the two front legs have the same joint variables, as do the two middle and the two rear legs.

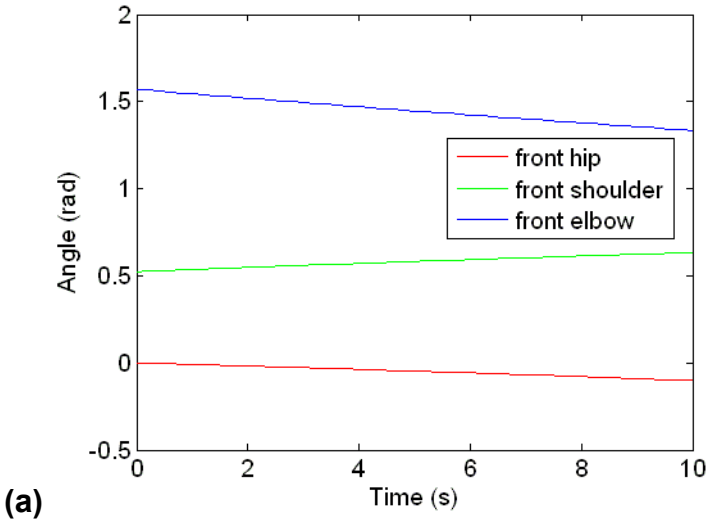

(a)

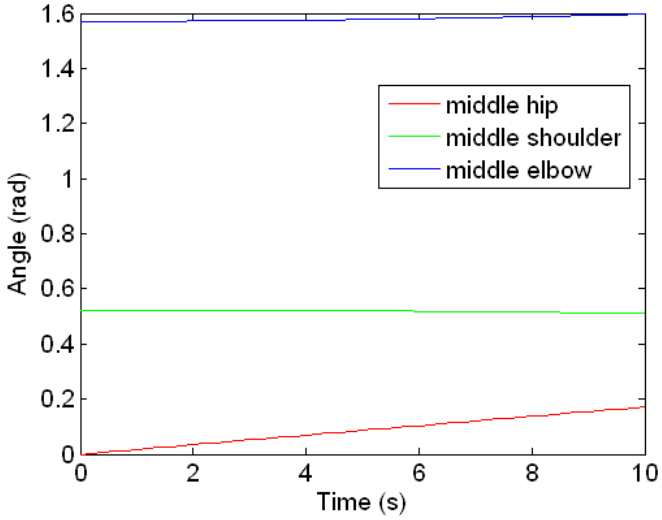

(b)

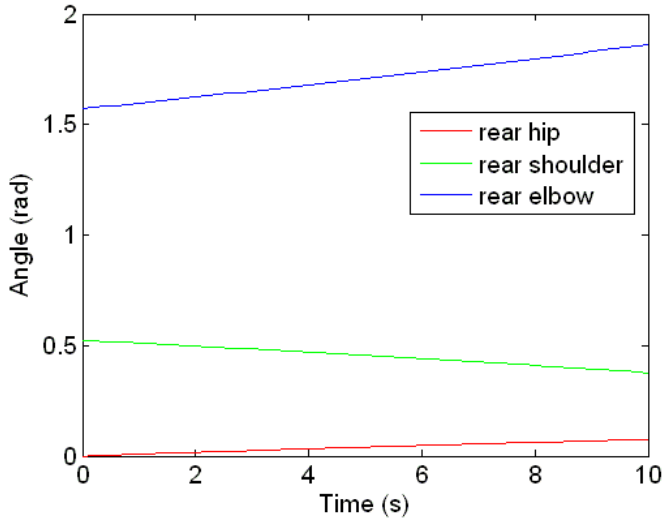

(c)

Figure 4-5: Joint variables in front (a), middle (b), and rear legs (c) for simulation of robot moving 10 mm forward.

4.2.2 Simulation with Webots™

The data generated using the kinematic equations were exported to an Excel table for all 18 joints. A virtual robot having the same geometry as Prototype 1 was built in Webots™ and simulated the movement of the robot by reading the Excel table [1]. Three situations were simulated in Webots: the robot body moving forward for 10 mm with all legs attached, the robot turning 0.5 radians with all legs attached, and the robot lifting up each leg once and then moving the body forward to complete one step. A screen shot of the visual robot is shown in Figure 4-9. From the visualization results, the robot moved as expected and, therefore, we determined that applying the data to the physical Prototype 1 would be safe.

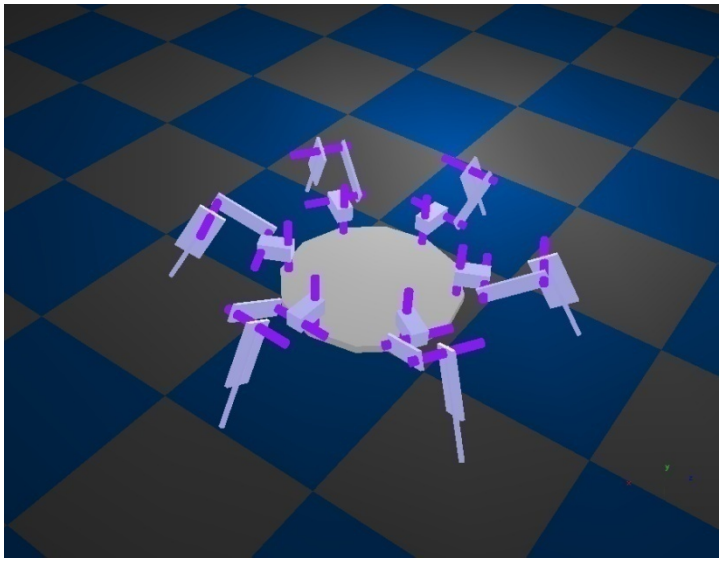

Figure 4-6: Prototype 1 simulated in Webots™. (Picture cited from Ausama. A. (2009))

4.3 Robot test in full step sequence

Combining the single leg kinematic and parallel platform kinematic equations, we determined that the robot should be able to walk in sequential steps as planned. Tests were performed to validate the gait planning on both level ground and a vertical wall.

4.3.1 Robot walking on level ground

Before applying the step sequence to the climbing robot on a tilted surface, the prescribed motion was first tested on level ground. A commercial platform AH3-R (Figure 4-10 (a)) from Lynxmotion was initially used in a walking test without adhesion on a horizontal surface. Such a platform was used in our preliminary tests as it can quickly and inexpensively be repaired in case of failure. The mechanical configuration of AH3-R was the same as Prototype 1, which enabled the robots to share the same kinematic equations. The only difference was that the AH3-R was much bigger than Prototype 1 (round body diameter of 300 mm, compared to Prototype 1 of 90 mm body diameter). The larger size of the robot platform was convenient to observe the test results. The robot electronics was the same as Prototype 1, allowing both platforms to use the same procedure. The computer transfered the position sequence stored in a look up table to the servo motors in each joint through the servo controller SSC-32.

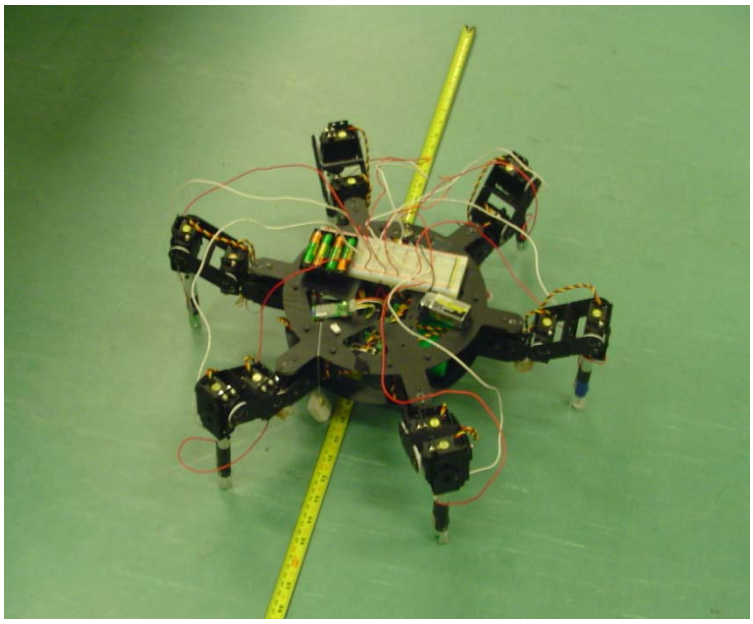

(a)

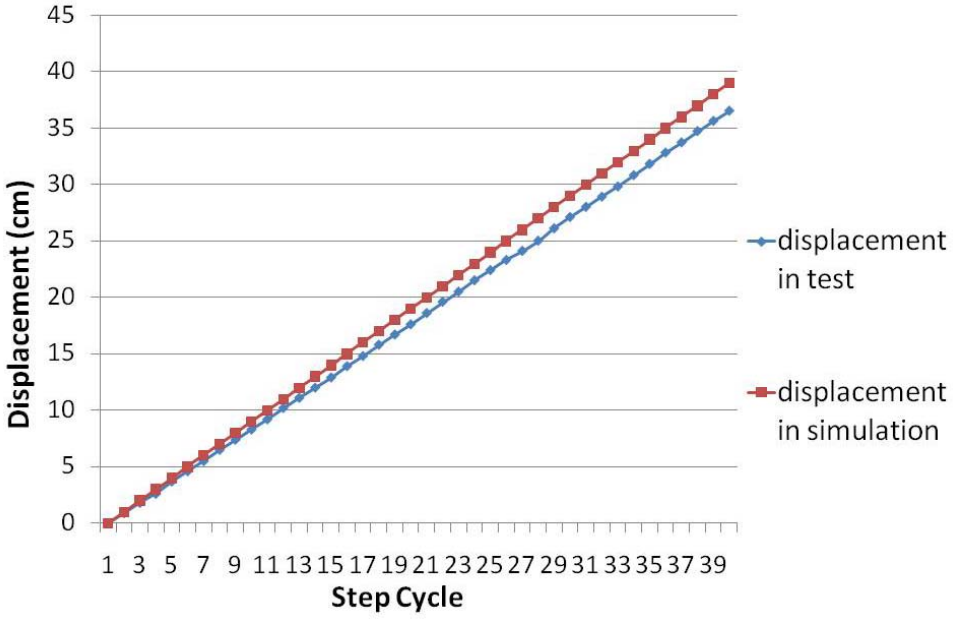

(b)

Figure 4-7: Test of robot walking on level ground. (a) Test platform AH3-R and setup. (b) Test result showing the error in 40 step cycles.

The motion of the robotic legs was designed to move the robot 10 mm forward for each step in a pentapedal gait, which moved one leg at a time. Each step was planned as follows: beginning with the Left Front Leg (LFL) and proceeding in counter clockwise, each leg was lifted, moved, and lowered one at a time, followed by the forward motion of the robot body. The tip of the leg was detached following a 45-degree trajectory to minimize the robot's power consumption (a detailed discussion is presented in the next section). The legs attached to the ground at 10 mm forward from the initial position. The initial and end positions with respect to the joint variables were identical in order to form a repeatable step cycle. The initial angles of the leg had the shoulder joint at 30 degrees, the elbow joint at -120 degrees, and the hip joint at 0 degrees (Figure 4-7 (a)), which poses the tibia perpendicular to the ground. Different initial positions were also tested, but the motors of the AH3-R have limited torque and this prevents exploring a wide range of feasible trajectories. For instance, with the tibia forming certain angles to the ground, e.g. 60 degrees, the robot body collapses due to gravity acting on the body weight. With a perpendicular tibia to the ground, however, this problem is avoided.

With the above configuration, the robot was set to walk in the same gait repeatedly for 40 step cycles. Test results are shown in Figure 4-7 (b). The robot was supposed to have a final displacement of 400 mm (40 cm), but it only reached 36.5 cm due to a 1 mm error in almost every step. The error was probably due to the mechanical clearances of the 18 revolute joints of the robot. However, the test still validated the kinematic equations and the planned gait.

4.3.2 Robot climbing on a vertical wall

Prototype 1 was tested on a tilted surface with pentapedal gait and, eventually, on a vertical Plexiglas surface (Figure 4-9). The tip of the leg was attached to a piece of single-layer adhesive through a silicone interface. This silicone interface formed the ankle mechanism (Figure 4-8) instead of the PDMS ankle mentioned in section 4.1.1. Different postures were tested for vertical climbing, including the one tested on the horizontal ground. The clearance of each joint caused the robot's body to drop a few millimeters in the direction of gravity. To minimize the gravitational effects on the robot's movement, the center of mass (COM), which is located at the geometric center of the robot body, was placed as close to the wall as possible. The middle legs were positioned upward, close to the front legs, because the robot tends to fall off the wall when the front legs detach first. By taking into account the results obtained during the force distribution tests (Appendix A), the middle legs, which were positioned closer to the front legs, were used to reinforce the front legs' adhesion.

The initial position of the legs when the robot climbs on a vertical wall were as follows: the shoulder joints were at 20 degrees, the elbow joints were at -50 degrees, and the hip joints were at 0 degrees for the front and rear legs and ± 45 degrees for the middle legs.

The gait was slightly different than previous conditions: first, the body was moved upward by 5 mm (Figure 4-9 (a-b)), then each leg was moved upwards by 5 mm from the LFL to LML in CCW sequence to form the full step cycle (Figure 4-9 (c-d)). Before starting the step, each foot was preloaded manually. From

observation, the displacement error should be bigger than the level ground test. The robot was not able to finish the second step cycle due to insufficient preloading on the adhesive to hold the robot in position for the next step cycle.

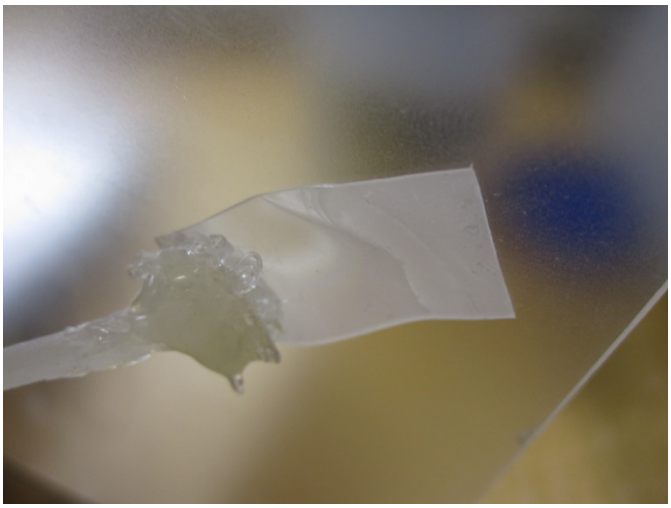

Figure 4-8: Foot used in the vertical climbing experiment. Single layer adhesive was glued to the leg tip with silicone sealant.

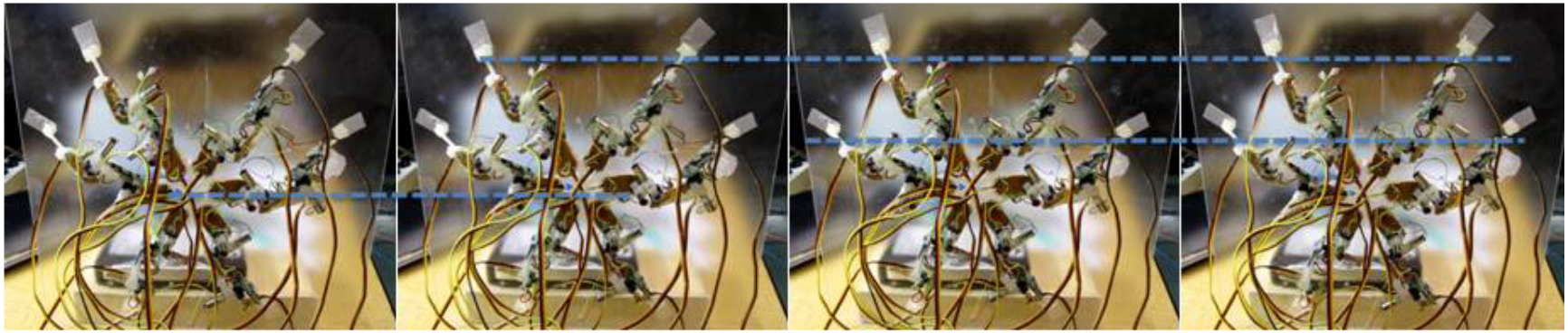

(a) **(b)** **(c)** **(d)**

Figure 4-9: Snap shots of the robot climbing on vertical Plexiglas. (a) Original position, (b) Body moved forward in 5mm, (c) Left front leg moved forward in 5 mm, (d) robot finished a full step cycle.

4.4 Trajectory selection for releasing the dry adhesive

The trajectory of the tip of each leg was at 45 degrees with respect to the surface for all the tests presented in the previous section. In this section, the motivation for selecting this particular trajectory is provided.

4.4.1 Theory of peeling an elastic thin film

The robot's foot was fabricated with thin layer of PDMS using the most recent adhesive design. The design is considered as an elastic thin film with dry adhesion attached at the bottom. As mentioned in Chapter 1, dry adhesives are easier to release when they are peeled from the surface. Several studies have investigated the efficiency of peeling elastic thin films and micro-fibrila, such as the gecko seta, in a certain direction [16-18][30-33]. Kendall [35] proposed a theory of peeling elastic thin films from a rigid substrate that indicated the relationship between peeling force and peeling angle (Figure 4-10:

$$(\frac{F}{b})^2 \frac{1}{2dE} + (\frac{F}{b})(1 - cos\theta) - R = 0 \qquad (4\text{-}1)$$

where *b*, *d*, and *E* denote the width, thickness, and Young's modulus of the elastic thin film. θ denotes the peeling angle between thin film and substrate. *F* represents the peeling force in the same angle θ with respect to the substrate. *R* denotes the adhesive energy, which is the experimental energy required to fracture a unit area of the interface. In equation (4-1), the first term is called the elastic term, the second is called the potential term, and the last term represents the surface term. Usually the elastic term may be neglected unless the material is

very soft or the peeling angle approaches zero. The surface term, *R*, is not a constant, and it depends on the crack speed.[4] If the peeling movement is performed at a constant speed, the relationship between the peeling force and angle simplified to:

$$\frac{F}{b}(1 - cos\theta) = R_c \tag{4-2}$$

where R_c denotes the adhesive energy when the crack speed is constant. Therefore, from the power saving point of view, to determine the movement of peeling a thin elastic film, the minimum force to release adhesion occurs at a peeling angle of 90 degrees with a constant crack speed.

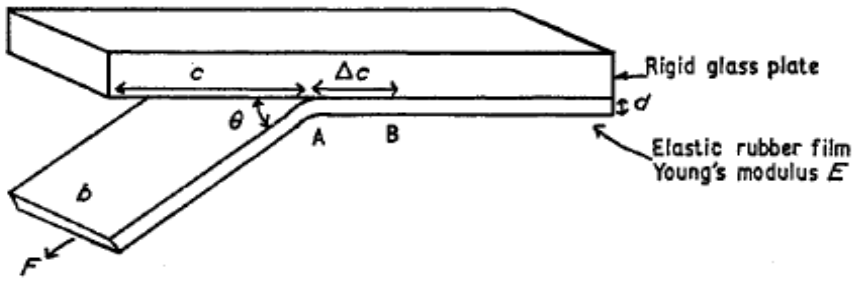

Figure 4-10: Elastic thin film peeling from a rigid substrate. (Picture cited from Kendall [35])

4.4.2 Power consumption test for various peeling angles

According to the above conclusion, keeping the peeling angle at 90 degrees should minimize the force required to peel off an elastic thin film. Although dry adhesion is a compliant mechanism combining structures from the

[4] Crack speed is the speed of rubber film detaching from the substrate.

macro to micro scale, it is worthwhile to validate the theory of peeling thin films in the macro scale before applying this technique to micro or nano structures in the robot adhesive. A test was performed by peeling an elastic thin layer at various angles. The test platform used is the same one as in the serial manipulator position test. The power consumption of the peeling process was recorded and compared. Since the peeling speed was very slow and constant, the power consumption should be proportional to the peeling force, which was intended to be minimized.

The trajectory for a certain peeling angle (90 and 60 degrees) is demonstrated in Figure 4-11. The bold lines show the adhesive pad at three positions during the peeling process. The dashed curves denote the unchanged length of the already released part of adhesive. The peeling force was always parallel to the adhesive pad. The end effector of the robot leg was fixed to the left end of the adhesive in the figure, while the right end was still on the substrate. Note that an equilateral triangle is formed by the adhesive before and after peeling, the trajectory of peeling the elastic thin film should be a 45-degree straight line as the figure shows. By using the same method, the trajectory for other peeling angles was also determined as different angles of straight lines: e.g., peeling angle of 30 and 60 degrees (Figure 4-11 (b)) have the trajectories of straight lines in 75 and 60 degrees with respect to the substrate.

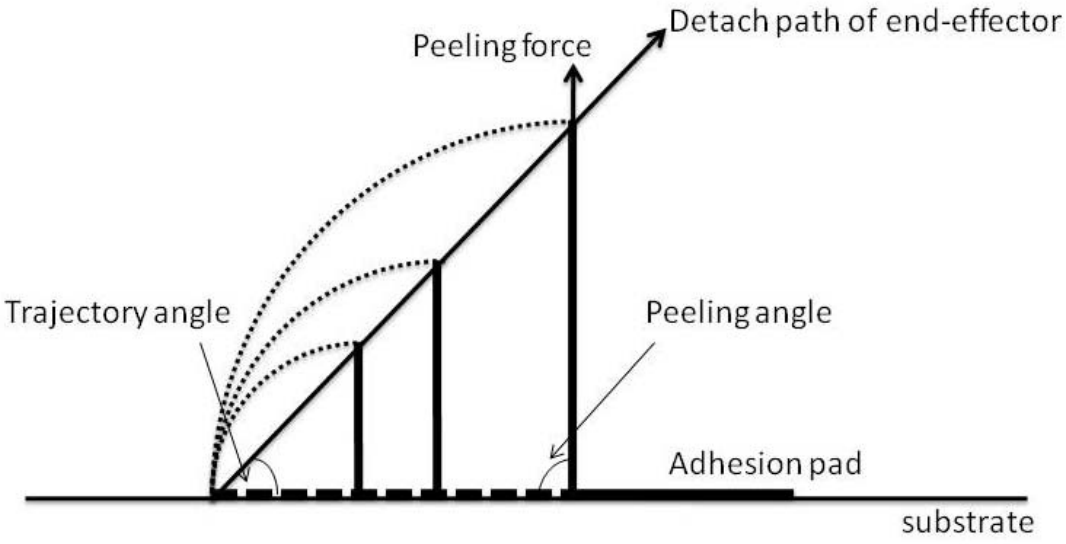

(a)

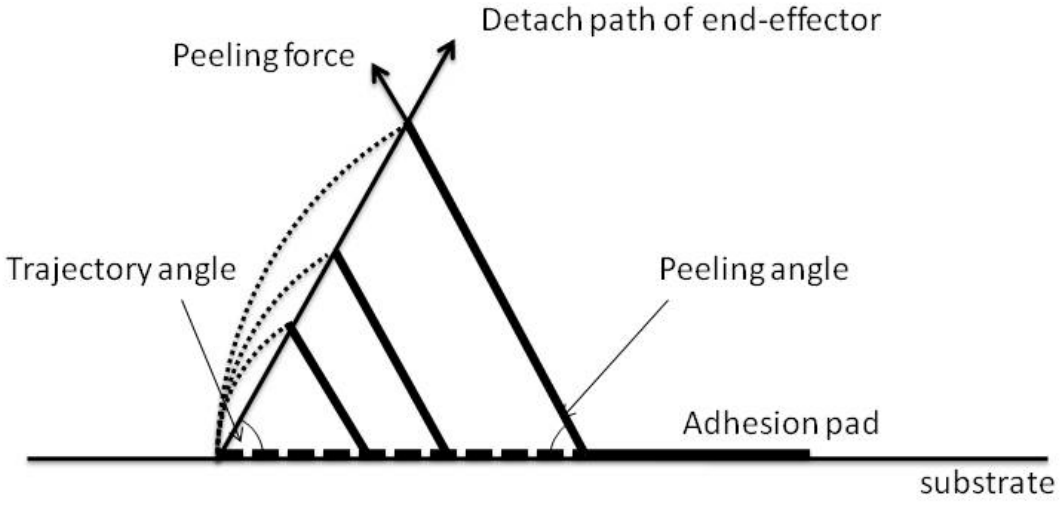

(b)

Figure 4-11: Trajectory with a constant peeling angle. (a) Peeling angle at 90 degrees. (b) Peeling angle at 60 degrees.

For the tests, a thin strip of silicone was attached to the end tip of a robotic leg. The initial position had the strip fully in contact with a Plexiglas substrate. A digital multimeter was plugged in between the power supply and the motor power

pin of the H-bridge chip to measure and record the current used by the actuation system. As the voltage supplied to the motors was constantly 3V, the peeling force should be proportional to the current required by the motors. Four sets of trajectories were studied: 30, 40, 45, and 60 degree straight lines upward from the substrate [37]. As Figure 4-12 shows, 45 degrees, which corresponds to a peeling angle of 90 degrees, consumes the least power. By observing the data of the 30 and 60 degree trajectories, the trend of the other peeling angles is predictable. The power consumption of 30 and 60 degrees were similar – because they are both 15 degrees from the minimum power trajectory at 45 degrees. The theory of peeling robot feet in the macro scale was validated and, therefore, applicable to the adhesion system. A 45-degree trajectory was, therefore, used during tests (e.g. in Figure 4-9).

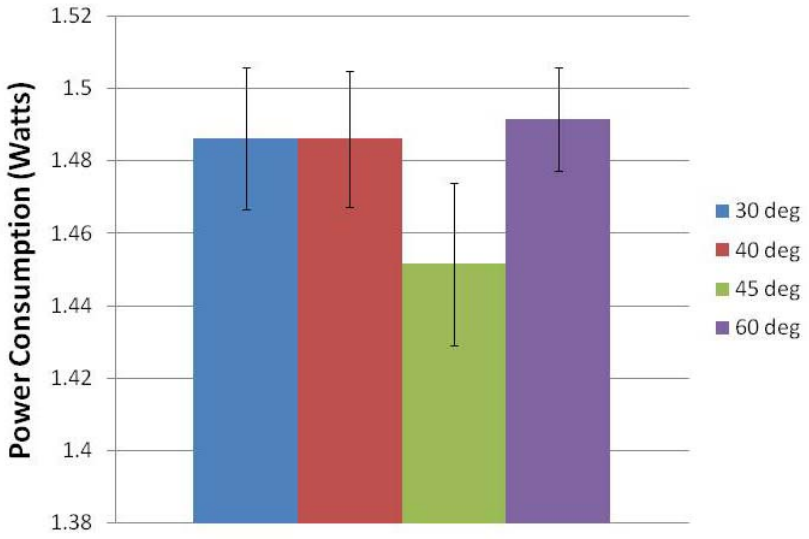

Figure 4-12: Power consumption of different peeling trajectories [1].

4.5 Optimizing the adhesive force

Different tests based on Prototype 2 were performed to investigate the optimal position that fully utilizes the unique properties of dry adhesion.

4.5.1 Optimal leg angle for maximizing the adhesive force

In order to determine the most power efficient joint torques for reliable adhesion, experiments were performed by measuring power consumption while the robot was attached to a wall. A simple test was initially performed to identify the optimal angle that the legs should assume to maximize the adhesive force. Tests were completed with a prototype having embedded PDMS feet. Each time after a measurement, the PDMS feet were cleaned by Scotch® tape to remove dust and allow them to have the same adhesion property, thus enabling repeatable measurements. A simple robot having three symmetric legs, each one controlled by a single motor, was used for this experiment. The tripod, and the angle α which was investigated in this preliminary analysis, are shown in Figure 4-13.

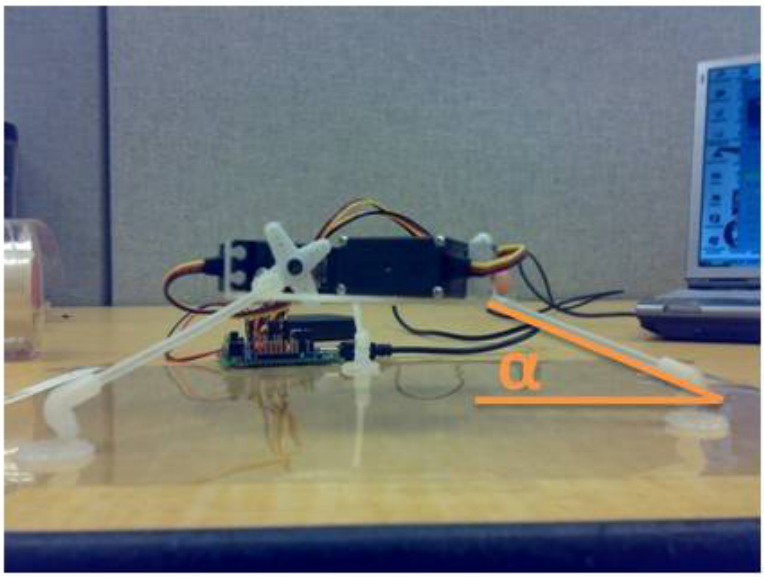

Figure 4-13: Test setup for determining the optimal leg angle for maximizing adhesion.

The tripod had a mass of 97 g. The robot was placed gently onto a smooth plastic surface. The preload of the feet was equal to the weight of the robot itself. Tests were performed by pulling the robot with a force normal to the surface, and the detaching force was recorded through a force sensor. Figure 4-14 shows the results obtained. The peeling force perpendicular to the surface was maximized when angle α was approximately at 45 degrees.

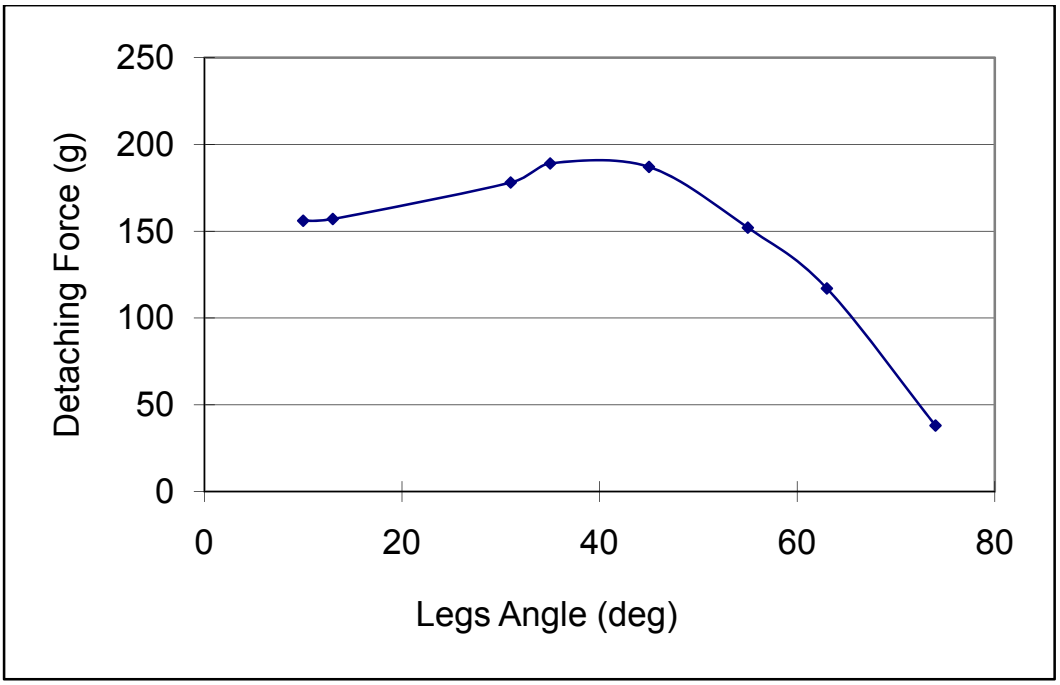

Figure 4-14: Test results of optimal leg angle.

4.5.2 Auto-preloading with optimized leg angle

By utilizing the result of the last section, an auto-preloading test with Prototype 2 was performed. Prototype 2 was positioned on a smooth surface, with all the legs posted at 45 degrees for angle α. The hip and shoulder joints were mechanically constrained, whereas the elbow joint imposed the preload to the smooth surface. A 1×1 cm^2 PDMS foot without micro or nano structures, which require a long time and effort to fabricate, was attached to the tip of each leg; the absence of micro/nano posts does not affect the validity of the results of the auto-preloading experiments. For a given torque to the motors, the horizontal surface on which the robot stood was gradually tilted. The angle at which the robot's feet detached from the surface was recorded.

Figure 4-15 shows the relationship between the total power consumption of the 6 motors used and the maximum slope of the inclined surface. The gripping effect caused by the preload provided by the legs is apparent from this figure. Without preload (power consumption equal to zero), the robot was able to stay attached to the surface up to 20 degrees of slope. For a 2.7 W input power, the robot was able to adhere up to a slope of almost 45 degrees. An equal voltage was provided to all the six motors. Optimization of the distribution of the torque could increase the gripping force. It should be remarked that an inclined surface was a stricter condition than an upside-down condition.

The results show that actively controlling the joint torque enhances the performance of the adhesive feet. Thereafter an investigation into optimal torques for each joint was performed to further investigate the adhesion performance.

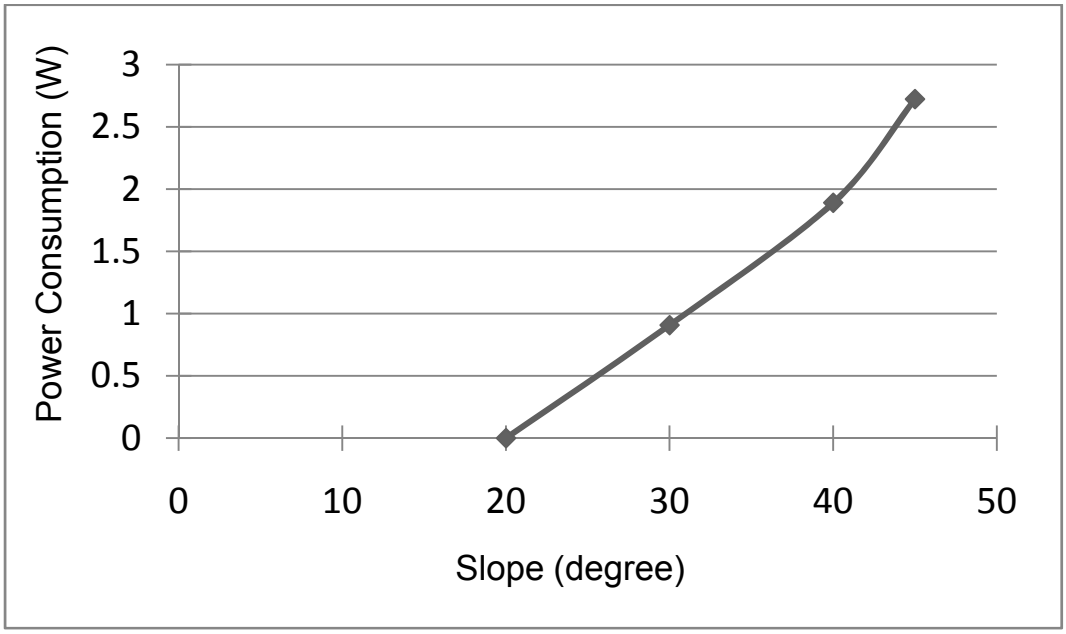

Figure 4-15: Test result of auto-preloading.

4.6 Experimental validation of optimal joint torques for stable adhesion

In order to identify the torque that each of the 18 motors should exert, an algorithm of optimal joint torques was developed for the climbing robot [38]. The algorithm is intended to maximize the preload in order to maximize adhesion and decrease the probability of adhesion failure during vertical climbing. The theoretical aspects of the algorithm are not described in this thesis as they were developed by another student of MENRVA group (Isacco Pretto, 2009 [38]). The experimental validation focuses on the situation of the robot climbing a vertical wall. A simplified platform was developed specifically for the purpose of providing an experimental validation of the algorithm - the current Prototypes 1 and 2 cannot in fact be used because they are not suitable for force control in their current design (i.e., the electronics should be suitable to control the torque of the motors and force sensors should be attached to each feet).

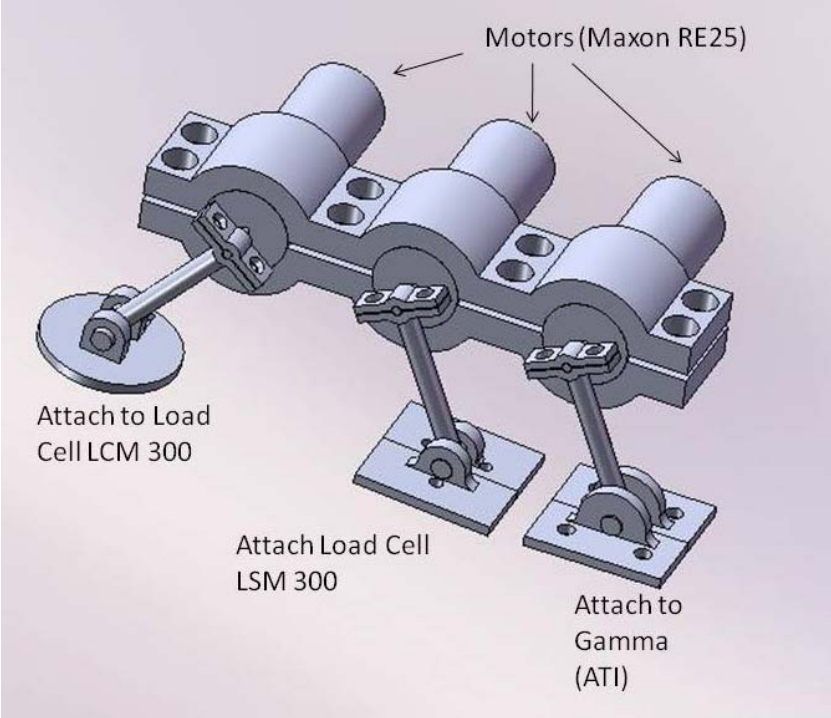

Figure 4-16: CAD model of simplified robot.

4.6.1 Experimental setup

The simplified platform includes two parts: the robot and the contact point sensing mechanism. The robot has three legs with equal length (Figure 4-16). The motors are arranged in a line with the motor shafts 50 mm apart. The leg length is also 50 mm. At the end of each leg, a revolute joint was designed to connect the sensor with a proper interface. Each sensor was fixed to a flat plate which was aligned and glued to a vertical surface. Because each contacting point was fixed to the wall, the robot was over constrained and could not move even when the motors were activated. The test platform with both parts assembled is shown in Figure 4-17.

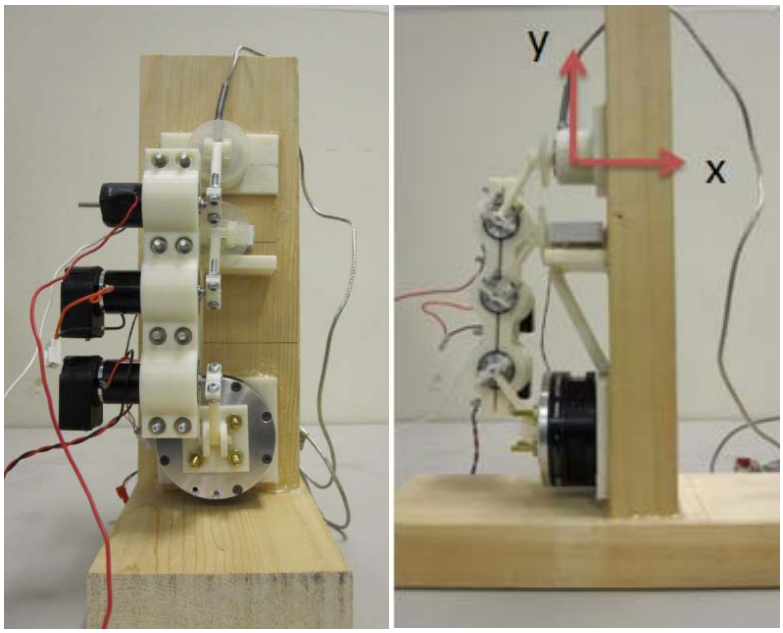

(a) **(b)**

Figure 4-17: Assembled test platform. (a) Front view. (b) Side view with coordinates used in the algorithm.

The motors (Maxon RE25) were able to provide relatively stable torques with a fixed current input. The maximum stall torque was 240 mNm according to the datasheet. Each motor was connected to a separate channel of the power supplies. The three sensors, from the bottom up, are a 6-axis Force/Torque sensor Gamma from ATI Industrial Automation, load cells LSM 300 and LCM 300 from Futek. A controller also from ATI was connected to the Gamma and a demo program was used to monitor the contacting force of the lower joint. For the load cells, a customized amplifier with a gain of 430 was used in to output the force reading of the upper two joints. A digital multimeter was connected to the

amplifier to record the reading. With this equipment, the sensors all have a resolution of about 5 g.

4.6.2 Test procedure and results

Before every measurement, the sensors were calibrated first in a no load situation. Joint torques were calibrated by a digital scale (accuracy in 0.1 g) with legs attached (see Appendix F). Six sets of joint torques were tested for further model fitting (Table 4-2). Variables $\tau 1$, $\tau 2$ and $\tau 3$ denote the torques from the upper, middle and lower motors, respectively. For each set of torques, three measurements were taken and averaged as the final output.

Table 4-1: Joint torques for model fitting

Test number	$\tau 1$ (Nm)	$\tau 2$ (Nm)	$\tau 3$ (Nm)
1	0	0	0
2	0.1	0	0
3	0	0.1	0
4	0	0	0.1
5	0.1	0.1	0.1
6	-0.2	-0.2	-0.2

Two tests were performed. In the first test, no torque was applied to the motors (see Figure 4-18). In the second test, optimal torques provided by the Min-max algorithm presented in [38], were used. Results are shown in Figure 4-18 and Table 4-2. Variables *C1x*, *C2x* and *C3x* denote the static adhesion forces, which were perpendicular to the wall on the upper, middle, and lower joints, respectively. The objective was to minimize the negative force (adhesion) having

the highest module; Table 4-2 shows that the proposed algorithm was able to reduce the maximum force from -4.5369 N (*C2x*) to -0.3875 N, thus reducing the adhesion requirements. Table 4-2 also shows that the contact forces from the experiments match the simulation results. Thus the proposed algorithm proved suitable for future implementations for climbing robots relying on adhesion.

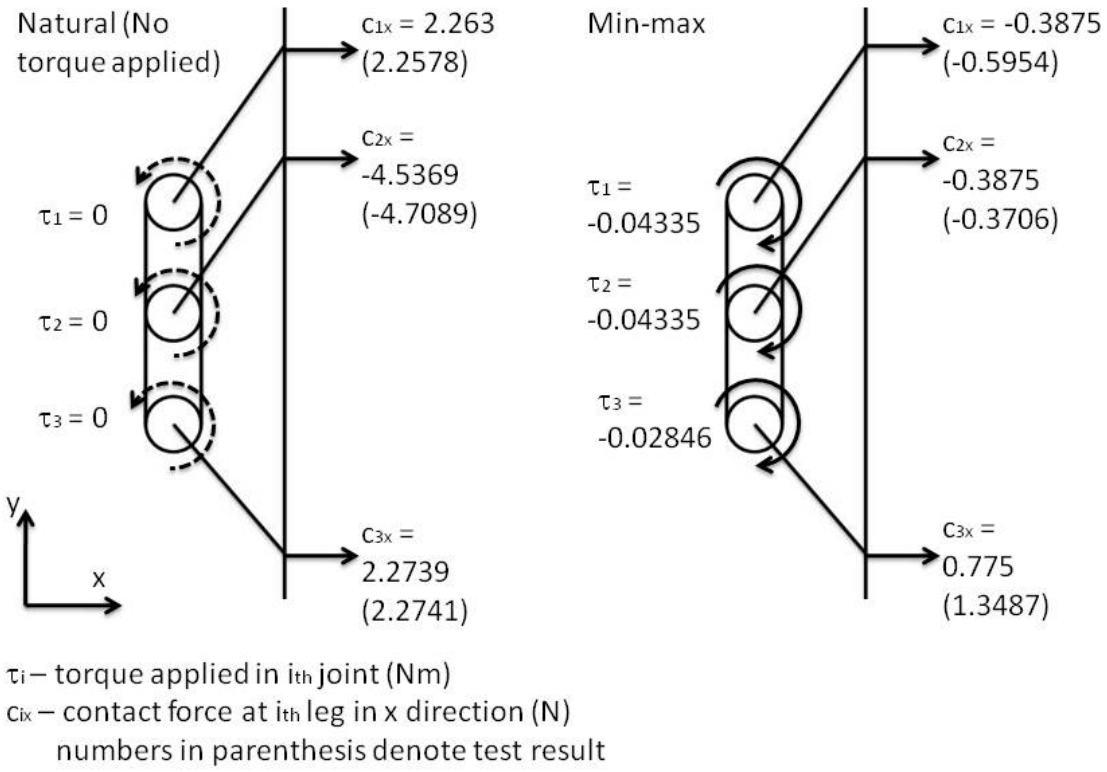

Figure 4-18: Results of control algorithm in simulations and experiments. Numbers in the parentheses denote the experimental result.

Table 4-2: Simulated and experimental results.

	Input torques			**Contact forces (simulator)**			**Contact forces (experiment)**		
	$\tau 1$ (Nm)	$\tau 2$ (Nm)	$\tau 3$ (Nm)	*C1x* (N)	*C2x* (N)	*C3x* (N)	*C1x* (N)	*C2x* (N)	*C3x* (N)
No torque applied	0	0	0	2.263	-4.5369	2.2739	2.2578	-4.7089	2.2741
Min-max algorithm	-0.043348	-0.043348	-0.028463	-0.3875	-0.3875	0.775	-0.05954	-0.3706	1.3487

4.7 Discussion and conclusion

This chapter presented the validation of kinematic analysis and a preliminary result of controlling adhesion force. Inverse kinematic equations were used to control the robot's movement in both simulations and physical robot tests. The simulation results proved that the equations are correct in the application so far. Trajectories for a single leg manipulation were validated in straight-line movements. Robot body manipulation was only tested in a moving robot platform parallel to a flat surface. Combining these test results led to the feasibility of the robot walking on level ground and climbing vertical surfaces. Passive mechanisms should be further investigated to compensate for the error introduced by manufacturing tolerances of various components.

A power consumption test for optimal release of dry adhesion was performed. A platform was designed to validate the adhesive's properties. In order to keep the supporting feet on the wall, the reaction force between wall and the peeling foot should be as small as possible. Test results validated the assumption in a macro-scale thin film adhesive. The test platform proposed here could be used with modification (e.g., adding another joint to control the approaching angle) in future foot designs before applying to the climbing robot and robot posture investigation.

Based on the two preliminary tests, the optimal angle between the leg and surface was obtained, and it was also proved that the adhesion forces can be increased by actively controlling the torque of the motors. Tests performed by using the Min-max algorithm showed that optimal joint torques can maximize

preload and minimize contact forces, thus enabling us to take full advantage of the adhesion properties.

CHAPTER 5 TOWARDS A FUTURE DESIGN – TETHER ACTUATED JOINT

The work space of each leg of the two prototypes introduced in Chapter 3 is theoretically defined by the set of points within the sphere surrounding the hip joint; however, it in reality is limited by the presence of the motors in the shoulder and elbow joints, which could collide in between the two legs. In order to increase the dexterity of the robot legs, a future tether-actuated joint design is proposed. The idea is to centralize all the motors on the robotic body and, therefore, increase the workspace of each leg. Furthermore, this design could be arranged in an under-actuated system. An early attempt was made by developing a tether-actuated leg (Figure 5-1). However, the leg was not properly designed to be under-actuated because of implementation difficulties.

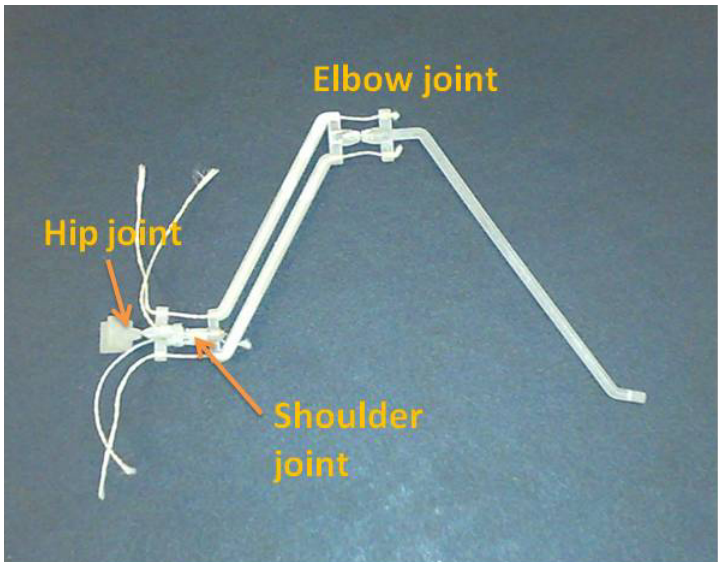

Figure 5-1: Leg prototype with tether actuation.

The leg prototype was designed with three joints similar to Prototype 1: the hip and shoulder joints connected in series and the elbow joint located far away between the femur and tibia. A thin plastic sheet connecting two adjacent links comprises one joint; e.g., a thin plastic sheet embedded between the femur and tibia to form the elbow joint. Two strings were fixed to the far away link; e.g., the knobs were located at the tibia to actuate the elbow joint. The joint was able to turn in both directions by pulling different strings (Figure 5-2).

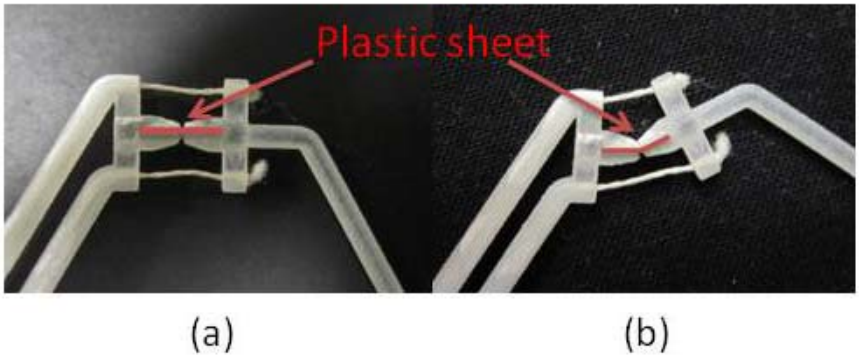

Figure 5-2: Tether actuating joint. (a) Original position (without pulling force). (b) Bending joint, joint rotate CCW with pulling upper string.

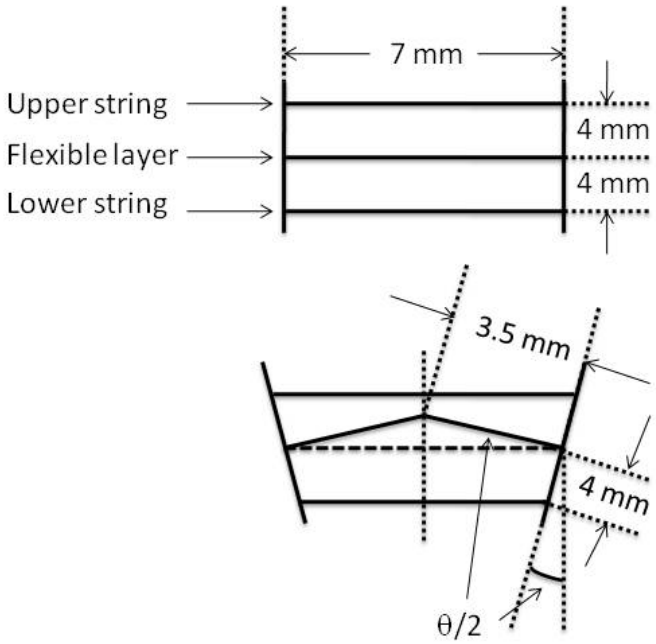

Figure 5-3: Calculation of string length in flexible joint.

By examining the geometry of the joint, clearly, the length between the two strings in one joint is different while the joint is bending. In the schematic of one joint, as shown in Figure 5-3, the elongation of the upper string is different from the shrinking distance of the lower string. The distance between string ends and the flexible layer on the part is fixed at 4 mm. Assuming the flexible layer is not stretchable, the distance between the bending point and the end of the joint is 3.5 mm. The strings are 7 mm in original position. The shrinkage of the lower string and the elongation of the upper string are given in following equations:

$$l_s = 7 - \left[2 \times \left(3.5cos\frac{\theta}{2} - 4sin\frac{\theta}{2}\right)\right] = 7 - 7cos\frac{\theta}{2} + 8sin\frac{\theta}{2} \quad (5\text{-}1)$$

$$l_e = \left[2 \times \left(3.5cos\frac{\theta}{2} + 4sin\frac{\theta}{2}\right)\right] - 7 = 7cos\frac{\theta}{2} + 8sin\frac{\theta}{2} - 7 \quad (5\text{-}2)$$

where θ denotes the angular change in the joint.

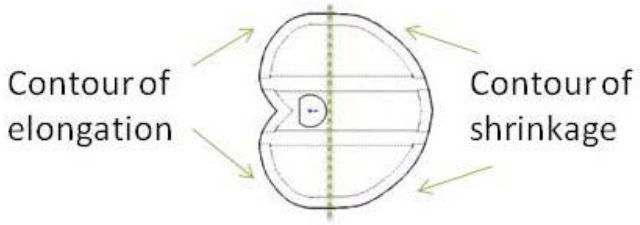

(a)

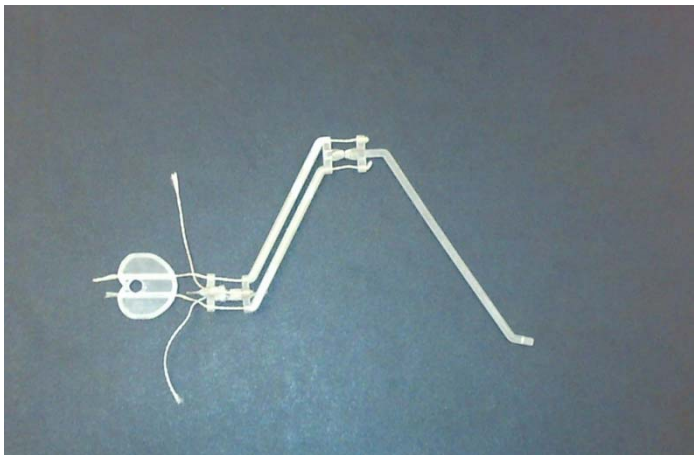

(b)

Figure 5-4: A cam design for pulling strings. (a) Contour of the cam for elongation and shrinkage. (b) A cam used to activate the elbow joint.

According to the above equations, a cam was designed to attach to the rotary motor in order to actuate this specific joint (Figure 5-4). The contour of the cam was designed to be symmetric to actuate the joint by rotating in both directions. The hole was attached to the motor shaft, which is housed at the robot body. Each joint needs a motor to actuate; therefore, the leg needs three cams attached to the motors. Considering the robot is mounted with six legs in this configuration, there will be eighteen cams and motors centralized at the body. The wiring path should be properly designed as it will be difficult to find space for mounting electronics. However, this design will centralize most of the body mass (mainly from the motors) at the body. The COM will always be inside the body volume and, therefore, will be easier to control compared to current prototypes. Further development of this under-actuated system will decrease the number of actuators and keep the advantage of a stable COM.

CHAPTER 6 CONCLUSIONS AND FUTURE WORK

6.1 Conclusions

Inspired by spiders, the development of a hexapod climbing robot was introduced in this thesis. Background studies on dry adhesion and climbing robots were provided. Existing climbing robots using dry adhesion encounter several problems in mobility, such as turning and transiting different angled surfaces. The proposed hexapod climbing robot in this research was designed to solve these problems. Although synthetic dry adhesion at the present stage was not able to adhere well to rough surfaces, the robot under development was developed with the potential to climb on various surfaces under different circumstance.

Motivated by designing such a robot, the mechanical design was inspired by spiders. The basic configuration of the climbing robot had six legs arranged in a circular platform, with three revolute actuators in each joint. In order to control the robot movement as planned, kinematics were studied in order to generate the joint variables following certain trajectories. Single leg kinematics and robot platform kinematics were considered in separate cases and afterwards were combined considering controlling the whole robot. The local ground coordinates were proposed because the original world coordinates which is fixed to the ground will become far away from the robot's coordinates while the robot keeps

walking. The introduction of the local ground coordinate provided an alternative approach for the robot to better cope with nearby terrain changes.

Two prototypes were developed based on the two configurations in different design approaches. Mechanical and mechatronic design aimed at developing a miniaturized and robust climbing system were presented. Prototype 1 utilized parts from commercially available servo motors. The electronic boards of the motors served also as structural components for the robot legs and body, in order to reduce the robot's weight. Prototype 2 used all customized electronics which were selected for their power saving potential. Sensors that produce no friction and actuators that provide relatively strong torque with a mini gearbox were used. All the components were small and lightweight, compared to existing climbing robots. The control strategies were different in both prototypes, while Prototype 2 required the consideration of much more sophisticated electronic design.

Based on the kinematic analysis, tests were performed to validate the equations. Experiments successfully proved the equations were applicable for the defined tasks, and those test platforms were further utilized to investigate adhesion and movement. The result of optimized trajectory for peeling the adhesive was applied to the climbing test. Prototype 1, with attached adhesive, achieves the goal of climbing a smooth vertical wall.

Several assumptions and considerations were considered during the investigation of the climbing and adhesion mechanism in order to finally develop a climbing robot integrated with a synthetic dry adhesive. Our preliminary result

shows the potential of achieving the goal of the proposed research. Future work will focus on improving the performance of the climbing robot from adhesion and power saving perspectives.

6.2 Future work

6.2.1 Four joints in each leg

While testing the robot climbing a vertical wall, the direction of the adhesive, which is the angle between adhesive film and the leg stem, changed every time when a different robot posture was used. Although the silicone glue provided flexibility for the rotation while the leg attached to the surface, the approaching angle was fixed and affects the preload and adhesion quality (attached area). A fourth joint, placed parallel to the shoulder and elbow joints, might be able to solve this problem. The kinematic configuration, therefore, will change, and each leg of the robot will become a redundant serial manipulator for end-effector position control. Joint angles will not be a single solution for a fixed end effector position. Trajectory planning should be analyzed carefully; by actively controlling the position of the end effector, the robot might perform better with the adhesive attached. Considering Prototype 1, the servo controller is able to connect to a maximum of 32 motors. With the same construction as the shoulder and elbow joint, the fourth joint can to be added without extra designs. However, this joint will increase six sets of sensors and actuators, which will increase both the complexity and weight of the climbing robot. The electronics will also become more complicated by significantly increasing the number of components, especially in Prototype 2. On the other hand, reducing actuators by

introducing an under-actuated system might compensate for this extra complexity.

6.2.2 Joints with tether actuation

As described in Chapter 5, an under-actuated system may be useful for future variations on this climbing robot. There are existing robot hands and tether actuated robotic systems for reference, e.g. the famous Utah/MIT dexterous hand, Stanford/JPL finger et al. The tether actuated system, or tendon driven system in bio-mimetic terms, is also inspired by nature. Spiders use both tendon and hydraulic tubes to actuate the joints in their legs [36]. By further investigating the spider actuation system, the design of future climbing robots might be able to reduce the number of actuators and, therefore, reduce the robot weight and improve climbing capabilities.

APPENDICES

Appendix A: Force distribution during walking

Force distribution in each leg during a designed gait was investigated in order to predict and further optimize the adhesion performance. The robot taking a pentapedal gait was simulated, and the forces at the tip of each leg were estimated using a multi-body simulator [1]. Afterwards, force distribution measurements were obtained using the AH3-R, which we modified by integrating Force Sensing Resistors (FSRs) at the tip of each leg (Figure A-1). Forces were recorded while the robot moved using the pentapedal gait. Figure D-2 (a) and (b) respectively show the simulated and measured forces of LFL during a full walking cycle.

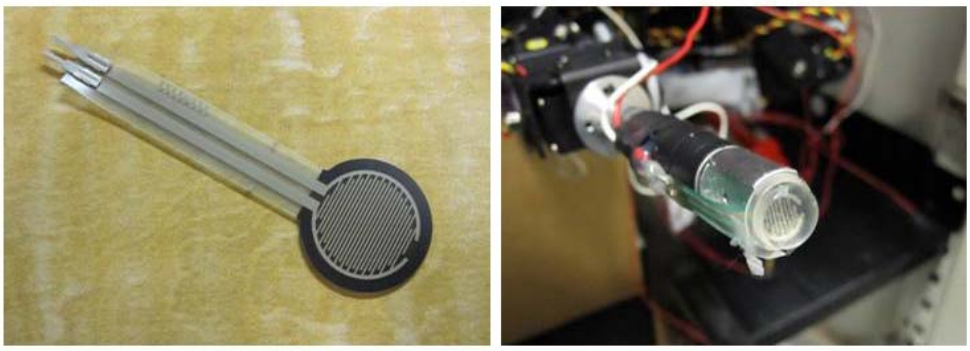

Figure A- 1: FSR modification on AH3-R. (a) FSR before attached to the leg. (b) A leg of AH3-R mounted by a FSR at the tip.

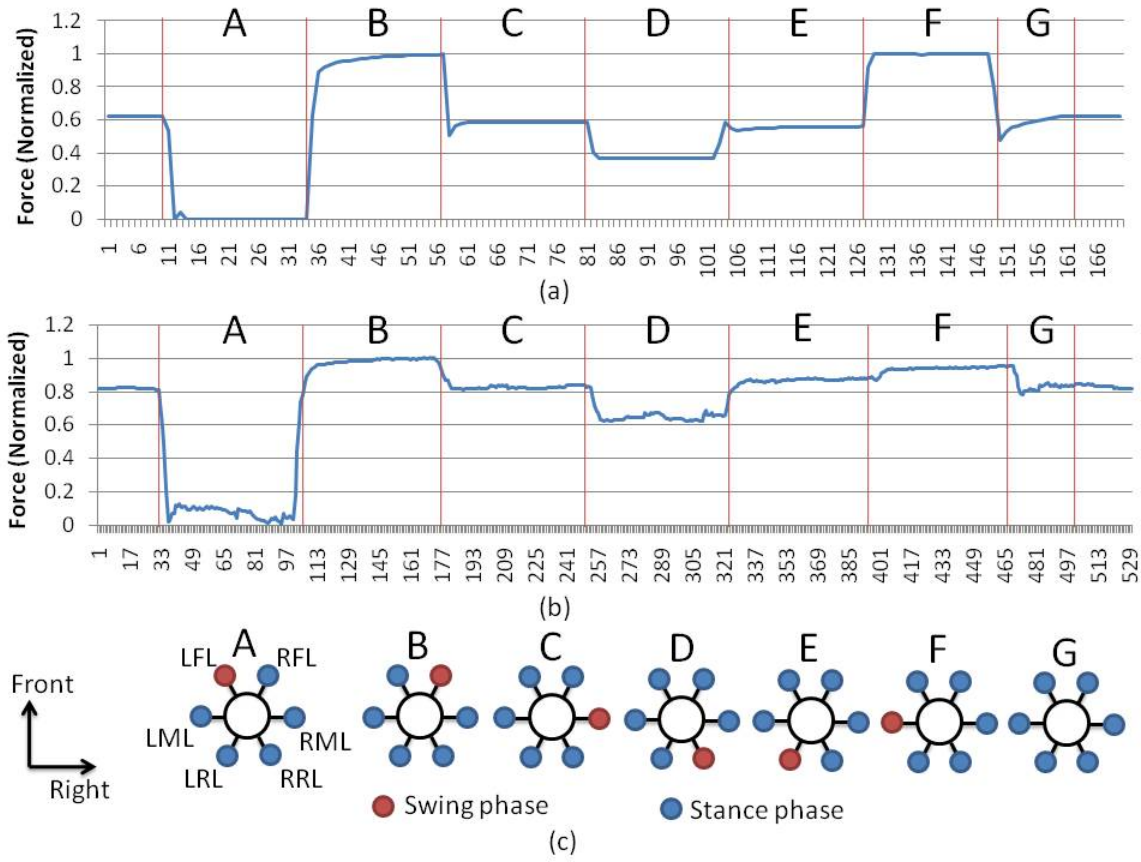

Figure A- 2: Force measurement targeted at Left Front Leg (LFL) within one step cycle. (a) Simulation data; (b) Measurement from real robot; (c) Devided phases during the robot movement. Looking from top, RFL stands for Right Front Leg, RML stands for Right Middle Leg, RRL stands for Right Rear Leg respectively [1].

In the designed gait, the LFL is the first leg taking action in the sequence (see Figure A-2). During Phase A, no force was applied to the end tip of the LFL as it is in swing phase. Phase B starts when the LFL contacts the ground and the Right Front Leg (RFL) is lifted. Since the RFL is not supporting any body weight, the LFL and Right Middle Leg (RML) should undergo the highest force as they share the load of the moving leg. Phase C starts with the RML moving up. The

LFL was not adjacent or opposite to the moving leg (RML) and has the same load as all legs are in contact to the ground. Data in Phase D shows that the force decreased when the opposite leg was in the swing phase. Phase E and F had a similar effect on Phase C and B. Phase G represents the robot body moving forward with all legs attached to the ground. Since the FSRs are not suitable to show the absolute value of the force, both the simulated and experimental data were normalized to better compare the trends of interested forces. We observed that (a) the moving leg bears no force and its opposite leg bears minor force, (b) two adjacent legs undergo the highest load during the movement, (c) forces at the non-adjacent and non-opposite legs were identical to the stance phase. Test results showed that the simulation was consistent to the realistic force distribution of the robot; therefore, future analyses predicting loads during vertical climbing or upside-down locomotion could accurately be performed.

The FSRs (Figure A-1 (a)) we used was manufactured by Interlink electronics [40]. Relationship between applied force and output voltage is not linear according to datasheet. A circuit for integrating the FSRs proposed by Lynxmotion [41] is utilized in force distributing test. Output voltage and the applied force was calibrated using a customized test. The relationship between force and voltage is shown in Figure A-3. Weights were put on the FSR and the corresponding output voltage was recorded.

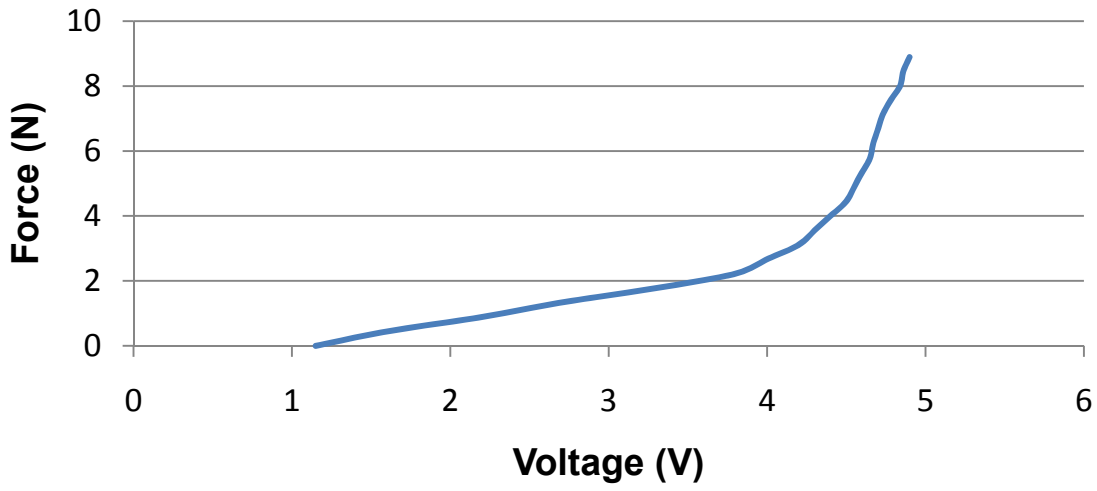

Figure A- 3: Relationship between applied force and output voltage.

The function used in converting voltage to force was generated using MATLAB. The function is given as follow:

$$F = 0.1126 \times V^5 - 1.4025 \times V^4 + 6.7427 \times V^3 - 15.5951 \times V^2 + 18.1189 \times V - 8.2377 \quad \text{(A-1)}$$

where F denotes the applied force and V denotes the output voltage.

Appendix B: Specification of servo motor HS-311

The specification of servo motor HS-311 used in Prototype 1 is given in Table B-1. Data were gained in [48].

Table B- 1: specification of servo motor HS-311.

Control system	+ pulse width control 1500 msec Neutral	
Operating voltage range	4.8 V to 6.0 V	
Test voltage	4.8 V	6.0 V
Operating speed	0.19 sec/60°at no load	0.15 sec/60°at no load
Stall torque	3 kg • cm	3.5 kg • cm
Idle current	7.4 mA at stopped	7.7 mA at stopped
Running current	160 mA/60° at no load	180 mA/60° at no load
Stall current	700 mA	800 mA
Dead band width	5 msec	5 msec
Operating travel	40°/one side pulse travelling 400 msec	
Direction	Clock wise/ pulse travelling 1500 to 1900 msec	
Motor type	Cored metal brush	
Potentiometer type	4 slider/ direct drive	
Amplifier type	Analog controller and transistor driver	
Dimension	40 mm × 20 mm × 36.5mm	
Weight	43 g (1.51 oz)	
Ball bearing	Top/resin bushing	
Gear material	resin	
Splined horns	Super/R-XA	
Connector wire length	300 mm (11.81 in)	
Connector wire strand counter	40 EA	

Appendix C: Specification of mini-motor GH6124S

The mini-motor GH6124S used in Prototype 1 is manufactured by Gizmo's zone [43]. In the same series, GH612, from the same manufacturer, the GH6124S has the highest gear ratio in the gearbox. The diameter of the motors in this series is 6 mm. Mechanical details and general specification of GH612 series are given in Table C-1 for comparison. The technical detail of GH612 series motor is given in Table C-2. Data in both tables are gained from the manufacturer [42].

Table C- 1: Mechanical details and specification of GH612 series 6mm mini-motors

Part number	GH6121S	GH6122S	GH6123S	GH6124S	
Operating voltage	3 V	3 V	3 V	3 V	Motor spec
Speed (no gearhead)	31000 rpm				
Gear stages	1	2	3	4	Gearhead spec
Gear ratio	1:5.14	1:26.45	1:136.02	1:699.55	
Voltage	3 V				No load
Speed (gearhead)	5000 rpm	1000 rpm	200 rpm	40 rpm	
Current	40 mA				
Maximum torque	5 g • cm	25 g • cm	120 g • cm	200 g • cm	Max. Output torque
Motor length (gearhead)	17.80 mm	19.60 mm	21.40 mm	23.20 mm	Physical parameters
Motor length (no gear head)	12 mm				
Shaft diameter	1.5 mm				
weight	1.6 g	1.7 g	1.8 g	1.9 g	
Gear head material	Glass Fiber Reinforced Engineering Plastic				

Table C- 2: Performance of GH612 series mini-motors at constant voltage of 3 V. (ambient temperature 25/30° C).

At no load	speed	28110 rpm
	current	0.0216 A
At rated load (0.4 g • cm)	speed	23620 rpm
	current	0.0678 A
At stall	torque	2.5 g • cm
	current	0.31 A
At maximum efficiency	efficiency	49.18%
	torque	0.5 g • cm
	speed	22488 rpm
	current	0.08 A
	output power	0.116 W
At maximum power output	output power	0.18 W
	torque	1.25 g • cm
	speed	14055 rpm
	current	0.16 A

Appendix D: Specification of mini-motor GM15

The mini-motor GM15 used in Prototype 2 is manufactured by Solarbotics [47]. Specification of GM15 is summarized in Table D-1.

Table D- 1: Specification of GM15 mini-motor [47].

Gear ratio	1:25	
Dimensions	20.1 mm × 6 mm × 6 mm (wire length 25 mm)	
Weight	1.3 g	
Test voltage	3 V	6 V
Unloaded speed	920 rpm	1550 rpm
Unloaded current	100 mA	200 mA
Stall current	210 mA	350 mA
Stall torque	35.28 g • cm	69.33 g • cm

Appendix E: Relationship between output voltage and rotary position of HMC1512

From an application note from Honey well [39], the HMC1512 is able to sense 180 degrees of rotary displacement using the following set of equations:

$$\Delta V = \Delta V_A - \Delta V_B = -V_s S sin(2\theta) \quad \text{(E-1)}$$

$$\Delta V_A = V_s S sin(2\theta) \quad \text{(E-2)}$$

$$\Delta V_B = -V_s S cos(2\theta) \quad \text{(E-3)}$$

where V_s is supplied voltage to the chip, S is the material constant which is set to 12 mV/V, θ is the reference of the magnetic field angle. The first equation denotes the relationship between the differentiated output voltage and magnetic angle, while the two equations below represent the individual bridge output with respect to the magnetic field angle.

Sensor test result in Figure 3-10 match the waveform graph the manufacturer provided in 135 degrees of displacement. Instead of equations (E-1) to (E-3), equations (3-1) and (3-2) were used to transform between output voltage and angular displacement. The modified equations in Chapter 3 are convenient to utilize and simplified in two situations, for they are easily integrated in the control node in LabVIEW.

Appendix F: Calibration of Maxon RE25 motor

A Maxon motor used in section 4.6 was calibrated with a scale and a simple arm structure. Test setup is shown in Figure F-1. The arm length is 65 mm. Test process consisted of driving the motor with constant current and no limit of voltage from a power supply, instead of constant voltage in most of the motor driven process, because the current would be proportional to the output power and therefore the output torque. This assumption was proved by the test result. The relationship between input current and output torque is given in Figure F-2. Observing from the chart, the relationship between current and torque is linear. Datasheet is given in [43], responding to model RE25-118752.

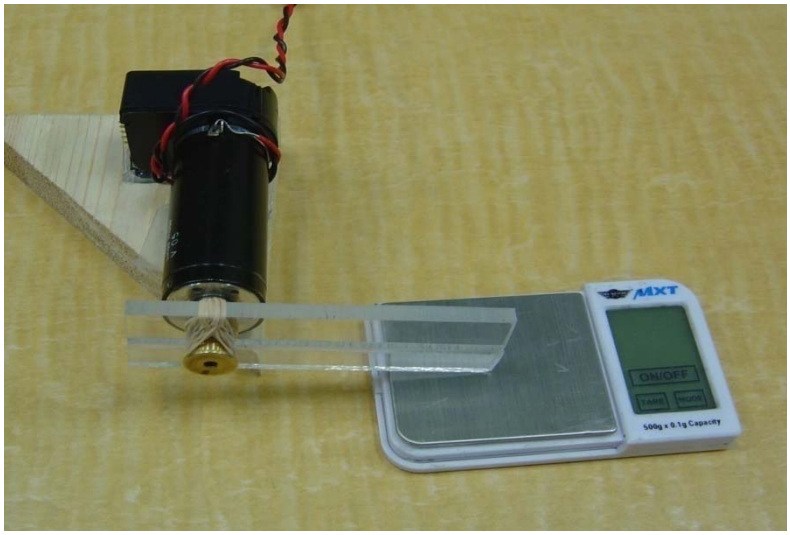

Figure F- 1: Test setup for Maxon motor calibration.

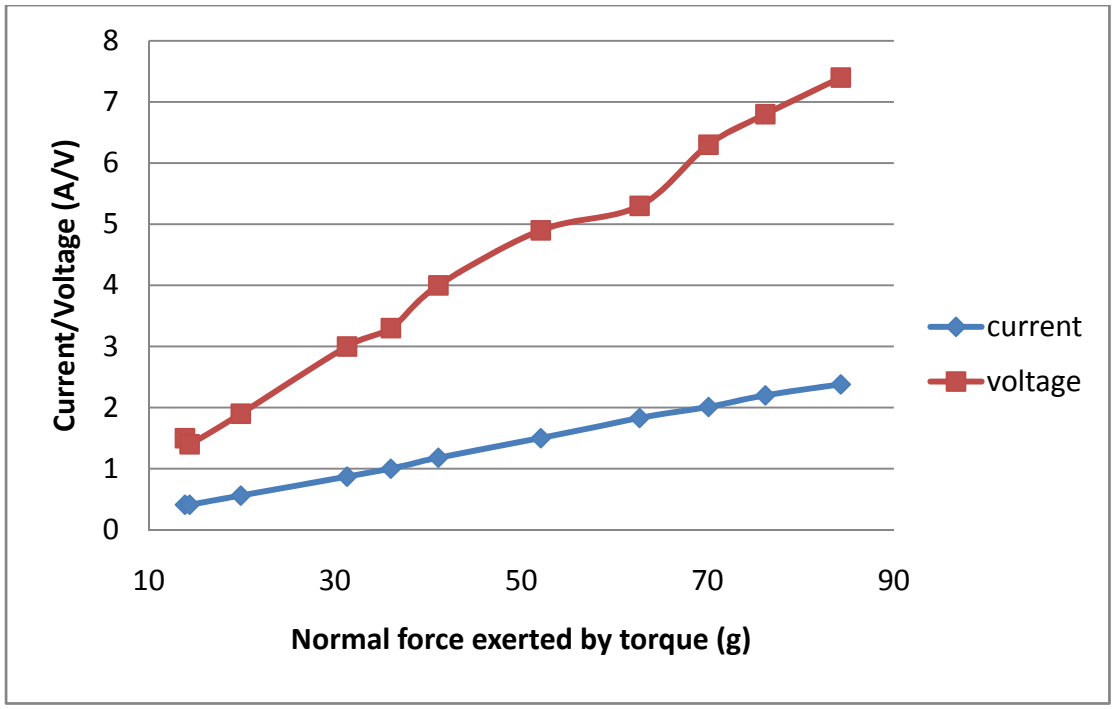

Figure F- 2: Relationship between input current and voltage with respect to the output torque.

BIBLIOGRAPHY[5]

[1] **Y. Li, A. Ahmed, C. Wu, C. Menon, "Preliminary Analysis of a Legged Robot Designed to Climb Vertical Surfaces", 2009 IEEE Toronto International Conference - Science and Technology for Humanity, Toronto, Canada, 2009.**

[2] K. Autumn, M. Sitti, Y. A. Liang, A. M. Peattle, W. R. Hansen, S. Sponberg, T. W. Kenny, R. Fearing, J. N. Israelachvili, and R. J. Full, "Evidence for van der waals adhesion in gecko setae," PNAS, vol. 99, pp. 12252-12256, 2002.

[3] S. Kim and M. Sitti, "Biologically inspired polymer microfibers with spatulate tips as repeatable fibrillar adhesives," Applied Physics Letters, vol. 89, pp. 261911 1-3, 2006.

[4] H. Yao, H, Gao, "Mechanics of robust and releasable adhesion in biology: Bottom-up designed hierarchical structures of gecko," Journal of the Mechanics and Physics of Solids, vol 54 (6), pp. 1120-1146, 2006.

[5] C. Menon, N. Lan, D. Sameoto, "Towards a methodical approach to implement biomimetic paradigms in the design of robotic systems for space applications", Applied Bionics and Biomechanics, pp.1–13, 2009.

[6] **D. Sameoto, Y. Li, C. Menon, "Multi-scale compliant foot designs and fabrication for use with a spider-inspired climbing robot", Journal of Bionic Engineering, Vol. 05, No. 03, pp. 189-19, 2008.**

[7] **D. Sameoto, Y. Li, C. Menon, "Micromask Generation for Polymer Morphology Control: Nanohair Fabrication for Synthetic Dry Adhesives", Advances in Science and Technology, Trans Tech Publications, Vol. 54 pp 439-444, 2008**.

[8] M. Greuter, G. Shah, G. Caprari, F. Tache, R. Siegwart, and M. Sitti, "Toward micro wall-climbing robots using biomimetic fibrillar adhesives," presented at Proceedings of the 3rd International Symposium on Autonomous Mini Robots for Research and Edutainment, Awara-Spa, Fukui, 2005.

[5] Publications highlighted throughout are results of this thesis work.

[9] K. A. Daltorio, S. Gorb, A. Peressadko, A. D. Horchler, R. E. Ritzmann, and R. D. Quinn, "A robot that climbs walls using microstructured polymer feet," Proceedings of the Eighth International Conference on Climbing and Walking Robots and the Support Technologies for Mobile Machines, pp. 131-138, 2005.

[10] O. Unver, A. Uneri, A. Aydemir, and M. Sitti, "Geckobot: a gecko inspired climbing robot using elastomer adhesives," Proceedings of the International Conference on Robotics and Automation, pp. 2329-2335, 2006.

[11] S. Kim, M. Spenko, S. Trujillo, B. Heyneman, M. V, and M. Cutkosky, "Whole body adhesion: heirarchical, directional and distributed control of adhesion forces for a climbing robot," IEEE Conference on Robotics and Automation, pp. 1268-1273, 2007.

[12] M. Murphy, M. Sitti, “Waalbot: an agile small-scale wall climbing robot ustilizing dry elastomer adhesives”, IEEE/ASME transactions on Mechatronics, vol. 12 (3), pp. 330-338, 2007.

[13] C. Menon, M. Murphy, and M. Sitti, "Gecko inspired surface climbing robots," IEEE International Conference on Robotics and Biomimetics, Shenyang, China, 2004.

[14] C. Menon, M. Murphy, M. Sitti, N. Lan, “Space exploration - towards new advanced bioinspired climbing robots, in (M.K. Habib Ed.) Bioinspiration and Robotics - Walking and Climbing Robots”, Advanced Robotic Systems International and I-Tech, pp544, 2007.

[15] C. Menon, M. Sitti, “A Biomimetic Climbing Robot Based on the Gecko”, Journal of Bionic Engineering, Elsevier, Vol. 3, No. 03, pp. 115-125. 2006.

[16] A. B. Kesel, A. Martin and T. Seidl, “Getting a grip on spider attachement: an AFM approach to microstructure adhesion in arthropods”, Smart Materials and Structures, vol 13, pp 512-518, 2004.

[17] S. Niederegger, S. N. Gorb, “Friction and adhesion in the tarsal and metatarsal scopulae”, J Comp Physiol A (2006) 192: 1223-1232.

[18] K. Autumn, Y. A. Liang, S. T. Hsieh, W. Zesch, W. P. Chan, T. W. Kenny, R. Fearing, and R. J. Full, "Adhesive force of a single gecko hair," Nature, vol. 405, pp. 681-685, 2000.

[19] D. Campolo, S. Jones, and R. S. Fearing, "Fabrication of gecko foot-hair like nano structures and adhesion to random rough surfaces," presented at Nanotechnology 2003, San Fransisco, CA, 2003.

[20] M. Sitti and R. S. Fearing, "Synthetic gecko foo-hair micro/nano-structures as dry adhesives," Journal of Adhesion Science and Technology, vol. 18, pp. 1055-1074, 2003.

[21] A. K. Geim, S. V. Dubonos, I. V. Grigorieva, K. S. Novoselov, A. A. Zhukov, and S. Y. Shapoval, "Microfabricated adhesive mimicking gecko foot-hair," Nature Materials, vol. 2, pp. 461-463, 2003.

[22] D. Santos, S. Kim, M. Spenko, A. Parness, M. Cutkosky, “Directional Adhesive Sturctures for Controlled Climbing on Smooth Vertical Surfaces”, 2007 IEEE International Conference on Robotics and Automation, pp1262-1267, 2007.

[23] B. Aksak, M. P. Murphy and M. Sitti, “Gecko Inspired Micro-Fibrillar Adhesives for Wall Climbing Robots on Micro/Nanoscale Rough Surfaces”, 2008 IEEE International Conference on Robotics and Automation, pp3058-3063, 2008.

[24] D. Sameoto, C. Menon, “Direct molding of dry adhesives with anisotropic peel strength,” Journal of Micromechanics and Microengineering, 2009.

[25] S. Kim, A. T. Asbeck, M. Cutkosky, and W. R. Provancher, "Spinybot II: climbing hard walls with compliant microspines," Proc. of 12th Int. Conf. on Advanced Robotics, pp. 601-606, 2005.

[26] A. Saundersa, D.I. Goldmanb, R.J. Fullb, M. Buehlera, “The RiSE Climbing Robot: Body and Leg Design,” Proc. of SPIE Vol. 6230, 623017, 2006.

[27] M. J. Randall, “Adaptive neural control of walking robots,” London: Professional Engineering, 2001, pp.2.

[28] **Y. Li, D. Sameoto, C. Menon, “Properties Validation of an Anisotropic Dry Adhesion Designed for Legged Climbing Robots”, 2009 IEEE International Conference on Robotics and Biomimetics, 2009**.

[29] Z. Wang, X. Ding, A. Rovetta, “Structure Design and Locomotion Analysis of a Novel Robot for Lunar Exploration”, 12th IFToMM World Congress, Besançon , France, June18-21, 2007.

[30] S. Kim and M. Sitti, "Biologically inspired polymer microfibers with spatulate tips as repeatable fibrillar adhesives," Applied Physics Letters, vol. 89, pp. 261911 1-3, 2006.

[31] H. Yao, H, Gao, “Mechanics of robust and releasable adhesion in biology: Bottom-up designed hierarchical structures of gecko,” Journal of the Mechanics and Physics of Solids, vol 54 (6), pp. 1120-1146, 2006.

[32] **D. Sameoto, Y. Li, C. Menon, “Multi-scale compliant foot designs and fabrication for use with a spider-inspired climbing robot”, Journal of Bionic Engineering, Vol. 05, No. 03, pp. 189-19, 2008**.

[33] **D. Sameoto, Y. Li, C. Menon, "Micromask Generation for Polymer Morphology Control: Nanohair Fabrication for Synthetic Dry Adhesives", Advances in Science and Technology, Trans Tech Publications, Vol. 54 (2008) pp 439-444**.

[34] **C. Menon, Y. Li, D. Sameoto, C. Martens, "Abigaille-I: towards the development of a spider-inspired climbing robot for space use," 2008 2nd IEEE RAS & EMBS International Conference on Biomedical Robotics and Biomechatronics. BioRob 2008, pp. 384-9, 2008**.

[35] K. Kendall, "Thin-film peeling – the elastic term," Journal of Physics D (Applied Physics), pp. 1449-1452, 1975.

[36] R. F. Foelix, "Biology of Spiders," New York: Oxford University Press; 1996.

[37] Claire W., Spider robot system design, Report for ENSC494 Special Project, School of Engineering Science, SFU, 2008.

[38] **I. Pretto, Y. Li, C. Menon, S. Cocuzza (in preparation) Strategies for optimizing adhesion force during robotic vertical climbing. To be submitted to IEEE Transaction on Robotics.**

[39] Magnetic Displacement Sensors HMC1501/1512, URL: http://www.magneticsensors.com/datasheets/hmc1501-1512.pdf.

[40] Interlink electronics, Force sensing resistor (FSR), URL: http://www.interlinkelectronics.com/force_sensors/technologies/fsr.html.

[41] James Frye, Hexapod Foot Sensor Assembly Guide, Lynxmotion Inc., URL: http://www.lynxmotion.com/images/html/build127.htm.

[42] Spec sheet of GH612 series 6mm mini motor, URL: http://www.gizmoszone.com/shopping/storepro5/html/pages/612metaldatasheet.pdf

[43] Maxon precision motors, URL: http://shop.maxonmotor.com/ishop/article/article/118752.xml.

[44] Manual of SSC-32, URL: http://www.lynxmotion.com/images/html/build136.htm.

[45] Specification of Visual Sequencer, URL: http://www.lynxmotion.com/Product.aspx?productID=443&CategoryID=15.

[46] Schematic of BlueSMiRF, URL: http://www.sparkfun.com/datasheets/RF/BlueSMiRF-Gold-ChipAnt-v1.pdf.

[47] Resource of GM15,
URL: http://www.solarbotics.com/products/gm15/resources/.

[48] Specification of servo motor HS311,
URL: http://www.hitecrcd.com/product_file/file/45/HS311.pdf.

[49] Specification of plastic material of 3D printer VisiJet® SR-200,
URL: http://www.simt.com/rpc/pdf/23100-S02-02_A_MSDS_US_English_SR200.pdf